

STRUCTURE AND MECHANICAL PROPERTIES OF CEMENT AND
INTERMETALLIC COMPOUNDS VIA *AB-INITIO* SIMULATIONS

A DISSERTATION IN
Physics
and
Geoscience

Presented to the Faculty of the University
of Missouri-Kansas City in partial fulfillment of
the requirements for the degree

DOCTOR OF PHILOSOPHY

by
Chamila Chathuranga Dharmawardhana
M.S., Central Michigan University, 2008

Kansas City, Missouri
2015

© 2015

Chamila Chathuranga Dharmawardhana

ALL RIGHTS RESERVED

STRUCTURE AND MECHANICAL PROPERTIES OF CEMENT AND INTERMETALLIC COMPOUNDS VIA *AB-INITIO* SIMULATIONS

Chamila Chathuranga Dharmawardhana, Candidate for the Doctor of Philosophy
Degree

University of Missouri-Kansas City, 2015

ABSTRACT

Calcium silicate hydrates comprise a class of minerals formed synthetically during Portland cement hydration or naturally through various geological processes. The importance of these minerals is immense since they are the primary binding phases for Portland cement derived construction materials. Efforts spanning centuries have been devoted to understand the structural aspects of cohesion in these minerals. In recent years, the focus has progressively turned to atomic level comprehension. Structurally these minerals can range from crystalline to highly disordered amorphous phases. This thesis focuses upon unraveling the nature of chemical bonding in a large subset of calcium silicate hydrate (CSH) crystals. Thus their electronic structure was calculated and bonding mechanisms were investigated quantitatively. Results highlight a wide range of contributions from each type of bonding (Si-O, Ca-O, O-H and hydrogen bond) with respect to silicate polymerization, crystal symmetry, water and OH content. Consequently, total bond order density (TBOD) was designated as the overall single criterion for characterizing crystal cohesion. The TBOD categorization indicates that a

rarely known orthorhombic phase Suolunite is closest to the ideal composition and structure of cement. Present work finds the relationship of partial bond order density (PBOD) of each bond species, especially HBs to the mechanical properties of CSH crystals. This can be used as a basis to validate existing C-S-H models and to build improved ones. This work goes further and validates the recently proposed models (2014) for C-S-H (I) phase on the same basis of proposed electronic structure parameters. Then the respective Calcium aluminosilicate hydrates C-A-S-H (I) phase models are proposed. Finally, these results lead to improved interpretations and construction of realistic atomistic models of cement hydrates.

Ab initio molecular dynamics (AIMD) could be vital to solve critical problems in complex structural material such as cement. However, it is far too early to be applicable for cement. Thus, this study used intermetallic compounds as a test case to develop new AIMD methods. In light of this objective, a direct method to calculate high temperature mechanical properties was devised for Mo_5Si_3 (T1 phase) and $\text{Mo}_5\text{B}_2\text{Si}_3$ (T2 phase). It was found that thermal expansion anisotropy (TEA) of T1 phase is captured by this simulation. It was also found an AIMD method to reduce TEA of Mo_5Si_3 (T1 phase) by strategic alloying. With further research these methods may be transferrable to cement and may allow optimizing the performance of hydraulic cements.

APPROVAL PAGE

The faculty listed below, appointed by the Dean of the School of Graduate Studies have examined a dissertation titled “Structure and Mechanical Properties of Cement and Intermetallic Compounds via *ab-initio* Simulations” presented by Chamila Chathuranga Dharmawardhana, candidate for the Doctor of Philosophy degree, and certify that in their opinion it is worthy of acceptance.

Supervisory Committee

Wai-Yim Ching, Ph.D., Committee Chair
Department of Physics

James B. Murowchick, Ph.D.
Department of Geosciences

Anil Misra, Ph.D.
Department of Civil, Environmental and Architectural Engineering, University of Kansas

Paul Rulis, Ph.D.
Department of Physics

Jejung Lee, Ph.D.
Department of Geosciences

CONTENTS

| | |
|---|-------|
| ABSTRACT | iii |
| ILLUSTRATIONS | x |
| TABLES | xvi |
| ACKNOWLEDGMENTS | xviii |
| CHAPTERS | |
| 1. INTRODUCTION..... | 1 |
| 1.1 Introduction to cement and C(A)SH | 4 |
| 1.2 Introduction to intermetallic high temperature superalloys | 7 |
| 1.3 Outline of thesis | 9 |
| 2. THEORY AND METHODOLOGY..... | 11 |
| 2.1 Density functional theory | 11 |
| 2.2 The orthogonalized linear combination of atomic orbitals (OLCAO) Method.... | 18 |
| 2.3 Vienna ab initio simulation package (VASP) | 20 |
| 2.3.1 Geometric optimization | 21 |
| 2.3.2 Elastic and mechanical properties calculations..... | 22 |
| 2.4 ab initio molecular dynamics (AIMD)..... | 24 |
| 3. MECHANICAL ANISOTROPY AND INTERLAYER COHESION OF LAYERED | |
| CSH CRYSTALS | 27 |
| 3.1 Introduction | 27 |
| 3.2 Computational modeling details | 30 |
| 3.3 Results and discussion | 30 |
| 3.3.1 Relaxed crystal structures..... | 30 |
| 3.3.2 Electronic structure of relaxed crystals | 33 |

| | |
|--|----|
| 3.3.3 Bond order and hydrogen bonding..... | 37 |
| 3.3.4 Mechanical properties and interlayer cohesion | 40 |
| 3.4 Summary and conclusion..... | 43 |
| 4. QUANTUM MECHANICAL METRIC FOR INTERNAL COHESION IN CEMENT | |
| CRYSTALS | 45 |
| 4.1 Introduction | 45 |
| 4.2 Computational modeling details | 47 |
| 4.3 Classifications and structural details of CSH crystals..... | 48 |
| 4.4 Electronic band structures of CSH | 52 |
| 4.5 Main types of bonds in CSH..... | 55 |
| 4.6 Bond order distribution for each group | 57 |
| 4.7 Quantum mechanical metric for internal cohesion in CSH | 65 |
| 4.8 Electronic structure of suolunite | 69 |
| 4.9 Discussion and conclusion | 70 |
| 5. NATURE OF INTERATOMIC BONDING IN CONTROLLING THE MECHANICAL | |
| PROPERTIES OF CALCIUM SILICATE HYDRATES | 74 |
| 5.1 Introduction | 74 |
| 5.2 Computational modeling details | 76 |
| 5.3 Results and discussion | 77 |
| 5.3.1 Relationship of CSH minerals with cement gel | 77 |
| 5.3.2 Elastic and mechanical properties of CSH crystals..... | 82 |
| 5.3.3 Relationship of bonding, atomic ratios and H/S ratio to mechanical | |
| properties..... | 86 |

| | | |
|-------|--|-----|
| 5.3.4 | Role of hydrogen bonding in controlling the mechanical properties | 92 |
| 5.4 | Conclusion | 97 |
| 6. | ELECTRONIC STRUCTURE OF C-(A)-S-H (I) PHASE: THE RICHARDSON-2014 MODELS..... | 98 |
| 6.1 | Introduction | 98 |
| 6.2 | Computational modeling details | 100 |
| 6.3 | Results and discussion | 101 |
| 6.3.1 | A realistic C-(A)-S-H (I) models: The Richardson-2014 models..... | 101 |
| 6.3.2 | Electronic structure of Richardson-2014 models | 111 |
| 6.3.3 | Bonding types of Richardson-2014 models | 113 |
| 6.4 | Summary and conclusion..... | 116 |
| 7. | TEMPERATURE DEPENDENT MECHANICAL PROPERTIES OF MO-SI-B COMPOUNDS VIA AB-INITIO MOLECULAR DYNAMICS..... | 119 |
| 7.1 | Introduction | 119 |
| 7.2 | AIMD method with in NVT ensemble | 122 |
| 7.3 | Thermal expansion and mechanical property calculation..... | 124 |
| 7.4 | Elastic and mechanical property calculation | 127 |
| 7.5 | Summary and conclusion..... | 131 |
| 8. | IN SEARCH OF ZERO THERMAL EXPANSION ANISOTROPY IN MO_5Si_3 BY STRATEGIC ALLOYING | 132 |
| 8.1 | Introduction | 132 |
| 8.2 | AIMD methodology and modeling details..... | 135 |
| 8.2.1 | NPT simulations..... | 135 |

| | |
|---|-----|
| 8.2.2 Second and third order elastic constants | 137 |
| 8.2.3 Phonon density of states..... | 138 |
| 8.3 Results and discussion | 140 |
| 8.3.1 Coefficient of thermal expansion (CTE) and thermal expansion anisotropy (TEA)..... | 140 |
| 8.3.2 Discussion on lattice anharmonicity in $\text{Mo}_5(\text{Si,Al})_3$ models | 143 |
| 8.4 Conclusion | 149 |
| 9. FINAL REMARKS AND FUTURE WORK | 151 |
| APPENDIX A:..... | 156 |
| A.1 Typical INCAR for NVT calculation | 156 |
| A.2 Typical INCAR for NPT calculation | 157 |
| A.3 AIMD scripts for data processing and plotting | 159 |
| BIBLIOGRAPHY | 167 |
| VITA | 188 |

ILLUSTRATIONS

| Figures | page |
|---|------|
| 1. (color online) The (1x2x2) supercell of (a) jennite, (b)T9A and (1x3x1) supercell of (c)T11A (d)T14A.The atoms are indicated as: Ca-Green, O-Red, Silicate tetrahedra-Grey, and H-white. | 28 |
| 2. Total and Partial Radial Pair Distributions of (a) jennite, (b)T9A, (c)T11A and (d) T14A. | 32 |
| 3. Upper panel: calculated band structure of (a _i) jennite, (b _i) T9A, (c _i) T11A and (d _i) T14A before geometric optimization. Lower panel: calculated band structure of (a _f) jennite, (b _f) T9A, (c _f)T11A and (d _f) T14A after geometric optimization. | 34 |
| 4. (color online) Total and element resolved partial density of states of (a) jennite, (b)T9A (c)T11A (d)T14A..... | 36 |
| 5. (color online) Total and orbital-resolved partial density of states of T14A: (a) Ca, (b) Si, (c) O (non-water), (d) O (in H ₂ O), (e) H..... | 37 |
| 6. color online) Distribution of bond order vs. bond length in: (a) jennite, (b) T9A, (c)T11A, and (d) T14A. The color code is Ca-O intra layer (solid black), Ca-O inter layer (open black), Si-O (red), covalent O-H in water (H-O-H) (blue), Non-water -O-H (green), HBs within water (H ₂ O---H) (pink), and non-water HBs (dark yellow). (color online) The schematic diagrams of the two types of HBs. (a) between H and O in two water molecules; (b) between H in a water molecule and a non-water O. | 39 |

| | | |
|-----|---|----|
| 7. | (color online) (a) Plot of the BOD and C/S ratios in the four CSH crystals; (b) Plot of mechanical parameters (K, G, E) in the four crystals..... | 43 |
| 8. | Ball and Stick diagrams of 20 CSH and CS crystal structures. | 51 |
| 9. | Band Structures of 20 CSH and CS crystal structures. | 54 |
| 10. | Distribution of bond order vs. bond length in four representative crystals. (a.2) Allite; (b.1) Alwillite; (c.2) Suolunite; and (d.8) Jennite. Symbols for different types of bonds are shown at the top, “-“ for covalent bond, “...” for hydrogen bond. The pie chart in the inset shows the percentage of different types of bonding: red, Ca-O; green, Si-O; violet covalent –(O-H); orange, other HB; blue, HB between H ₂ O. Lower insets show different types of hydrogen bonds. ... | 56 |
| 11. | BO distribution of main bond types in 20 CS/CSH crystals. Pie charts in corresponding insets show % BO of each types of bond except covenant bond of H ₂ O. Color scheme given in the legend is common to both scatter plots and pie charts. | 61 |
| 12. | (a) Total bond order density vs. C/S ratio in 19 crystals. (Portlandite (a.3) was excluded since it has no Si atoms.); (b) TBOD distribution map vs. the composition of Ca:Si:H. The color bar labels the values for the TBOD. The dot-dash lines indicate specific C/S ratios. | 66 |
| 13. | Total and partial DOS of Suolunite. The DOS scale is made different for PDOS for clarity. | 70 |
| 14. | Effective water content to Si ratio (H ₂ O/Si) vs C/S ratio in the present study (open symbols for different groups). The effective water content is comparable with total water measured in SANS performed by Allen <i>et. al.</i> ³⁸ and a set of | |

| | |
|--|----|
| controlled drying experiments by Cong and Kirkpatrick ³⁷ (solid symbols). | |
| The solid and dashed lines are guides to the eye for an approximate linear correlation. | 79 |
| 15. (a) Ternary map of HB-PBOD distribution vs. Ca:Si:H ratio. The color bar label the values for HB-BOD. The dot-dash lines indicate specific C/S ratios. Each data point is marked and represents a crystals according to Table1. (b) Similar ternary maps for the calculated shear modulus G (in unit of GPa) vs. the composition of Ca:Si:H, (c) same for bulk modulus K and, (d) Young's modulus E | 84 |
| 16. Distribution of mechanical parameters K , G and E (GPa) as a function of PBOD of: a) Si-O, b) Ca-O and c) HBs. Different symbols designate four different groups of crystals: <i>a</i> (open square), <i>b</i> (red circle), <i>c</i> (blue triangle up), and <i>d</i> (pink triangle down). | 88 |
| 17. Distribution of K , G and E as a function of atomic percentage of (a) Si, (b) Ca and (c) H. | 90 |
| 18. Distribution of K , G and E as a function of percentage of (a) H_2O and (b) OH. | 90 |
| 19. Bulk mechanical properties as a function of (a) C/S ratio and (c) H/S ratio. | 92 |
| 20. (a) Four different structural units: T (SiO_4 tetrahedron), TH (SiO_4 -H), W (H_2O), CH ($2Ca$ -O-H) of local environment for oxygen (T, TH, W and CH) and H (TH, W) in CSH. (b) 12 different types of hydrogen bonding between the four units in (a): (1) T-TH, (2) T-W, (3) T-CH, (4) TH-TH, (5) TH-W, (6) TH-CH, (7) W-TH, (8) W-W, (9) W-CH, (10) CH-TH, (11) CH-W, (12) CH-CH. (c) BO vs. BL distribution for HB and Ca-O bonds in 15 hydrated CSH crystals. | |

| | |
|---|-----|
| Different types of HBs are labeled with different color and symbols. The inset pie chart shows the percentage BO for different types of hydrogen bonding. Specific BO for suolunite (c.2) and the highest BO from afwillite (b.1) are indicated by arrows. | 94 |
| 21. (a) Normalized frequency histogram for the Ca—O distances that are present in the crystal structures of 35 crystalline calcium silicate hydrates and related phases. (b) Histogram that shows the percentage of the Ca atoms in these phases that are coordinated to different numbers of O atoms. (see ref. ¹⁶ and references there in) | 102 |
| 22. Representation of BT, PT and v (vacant) sites. The Q ⁿ notation is NMR terminology..... | 104 |
| 23. Ball&Stick diagrams of (a) Tinf_14sc (b) Tinf_14sc+Al_model1 and (c) Tinf_14sc+Al_model2..... | 108 |
| 24. Ball&Stick diagrams of (a) Tinf_sc_noCa_LS1 and (b) Tinf_sc_noCa_LS1+Al. | 109 |
| 25. Degree of possible Al ³⁺ substitutions in C-A-S-H (I) phases. (see ref ¹⁶ for experimental data and references)..... | 110 |
| 26. Total and partial DOS of (a) Tinf_14sc (b) Tinf_14sc+Al_model1 and (c) Tinf_14sc+Al_model2..... | 112 |
| 27. Total and partial DOS of (a) Tinf_sc_noCa_LS1 and (b) Tinf_sc_noCa_LS1+Al. | 113 |

| | | |
|-----|---|-----|
| 28. | Bo vs BL scatter plot of (a) Tinf_14sc (b) Tinf_14sc+Al_model1 and (c) Tinf_14sc+Al_model2. The inset shows the pie chart of % contributions of bond types..... | 114 |
| 29. | Bo vs BL scatter plot of (a) Tinf_sc_noCa_LS1 and (b) Tinf_sc_noCa_LS1+Al. The inset shows the pie chart of % contributions of bond types. | 115 |
| 30. | Unit cell of (a) T1 and (b) T2 | 121 |
| 31. | Pressure fluctuation during the AIMD relaxation of (a) T1, (b)T2 for temperatures 300 K, 1000 K, 1500 K and 2000 K..... | 124 |
| 32. | The calculated and experimental (^a ref. ¹¹⁶ , ^b ref. ¹²⁵) thermal expansion of T1 on (a) <i>a</i> -axis, (b) <i>c</i> -axis and on T2 phases (c) <i>a</i> -axis, (d) <i>c</i> -axis | 125 |
| 33. | Calculated temperature dependence C_{ij} of T2 and corresponding experimental data ^{114a} (b) calculated bulk mechanical properties (K, G, E, γ) and experimental data at room T ¹²⁷ for T1 (c) calculated bulk mechanical properties (K, G, E, γ) and experimental data ^{114a} for T2. The calculated results are indicated in black circles and the corresponding experimental results are indicated in red circles. The fit to 3 rd order BM-EOS ¹²⁴ from isotropic volume change is indicated in blue circles..... | 128 |
| 34. | (a) Atomic structure of Mo ₅ Si ₃ viewed from <i>c</i> direction; (b) Mo-2 chain (4b sites) viewed from <i>a</i> -axis direction | 133 |
| 35. | Fluctuation of: (a) pressure and (b) Temperature as a function of AIMD run time in the model with 25% V concentration at 300K. Averages are taken from data after the 1ps tome represented by the vertical line..... | 137 |
| 36. | Velocity auto correlation function (VACF) for Mo and Si in Mo ₅ Si ₃ at 300K. | 139 |

| | |
|--|-----|
| 37. Simulated CTE for $(\text{Mo,V})_5\text{Si}_3$ as a function of Vanadium concentration: (a) α_c , and (b) α_a ; (c) TEA. Experiment data are from Rawn et al (2005) shown in red open circles and Rodrigues et al (2009) shown in red open star symbols. | 141 |
| 38. Simulated (a) CTE and (b) TEA as a function of % Al substitution in $\text{Mo}_5(\text{Si,Al})_3$ alloys..... | 142 |
| 39. Calculated phonon DOS at the ground state using DFT for: (a) Mo_5Si_3 ; (b) Mo_5Al_3 | 145 |
| 40. Ground state phonon PDOS projected along: (a) <i>a</i> direction and (b) <i>c</i> direction for Mo_5Si_3 ; and (c) <i>a</i> direction and (d) <i>c</i> direction for Mo_5Al_3 | 146 |
| 41. Phonon PDOS from AIMD at T=1500K for Mo_5Si_3 projected on the (a) <i>a-axis</i> (b) <i>c-axis</i> and for Mo_5Al_3 projected on the (c) <i>a-axis</i> (d) <i>c-axis</i> | 149 |

TABLES

| Table | page |
|---|------|
| 1. Experimental/Theoretical cell parameters for the jennite and tobermorite family of crystals. | 32 |
| 2. Summary of bond order for each type of bond (BO%). | 38 |
| 3. Calculated elastic constants for the four CSH crystals in units of GPa. | 41 |
| 4. Average mechanical properties including comparison with existing work | 41 |
| 5. Mineral names, crystal symmetry and space group symmetry, chemical formulas, Calculated C/S, density, and band gap (in eV) of the 20 crystals in this study. | 50 |
| 6. Experimental crystal parameters of the 20 crystals. | 52 |
| 7. The crystal parameters (% error from experimentally reported values). | 55 |
| 8. Designated label for each class, mineral name[chemical formula], SiO-BOD, CaO-BOD and HB-BOD, TBOD, (BOD x 10 ⁻³) Bulk modulus (K), shear modulus (G) and Young's modulus (E) (GPa) of 20 crystal phases. | 80 |
| 9. Major elastic constants (GPa), Poisson's ratio (γ) percentage Ca, Si, hydroxyl (OH) and H ₂ O atoms (in the simulation cell) of 20 crystal phases. | 81 |
| 10. Minor elastic constants (GPa) of 20 crystal phases. | 82 |
| 11. Reported/VASP relaxed lattice parameters and there % difference and lattice parameters for the proposed C-A-S-H phases. | 109 |
| 12. Calculated CTE and TEA of a-axis, c-axis by linear fitting along with available experimental data. | 127 |
| 13. Calculated elastic constants (in GPa) of T1 phase. The experimental data is only available at room temperature (^a ref. ^{114b}). | 129 |

| | |
|--|-----|
| 14. Elastic constants and bulk mechanical properties (in GPa) of sampled models for temperatures considered for T1. | 129 |
| 15. Calculated second-order elastic constants (GPa) for a T1 unit cell substituting Al on Si sites. Number in the parenthesis is the experimental data ^a | 144 |
| 16. Calculated third-order elastic constants (GPa) of $\text{Mo}_5(\text{Si},\text{Al})_3$. Here $C_{111} + 3C_{112}$ and $C_{113} + C_{123}$ measure the 'softening rate' ¹⁴¹ of the tensile modulus $C_{11} + C_{12}$ (GPa) with [100] and [001] expansions respectively. | 146 |

ACKNOWLEDGMENTS

Words simply cannot express gratitude for my PhD adviser Prof. Wai-Yim Ching for the motivation, advice and wisdom during my stay at UMKC. This work would not be possible without his guidance. I would also like to thank Prof. Anil Misra, Prof. Ridwan Sakidja and Prof. Paul Rulis for their insight, guidance and support on many collaborated work. I also would like to thank my MS adviser Prof. Koblar Alan Jackson for guiding me to the wonderful world of computational simulations.

This work is supported and enriched by the members of Electronic Structure Group and Computation Physics Group at UMKC. My special thank therefore must go to Dr. SitaRam Aryal, Mr. Jay Eifler, Mr. Naseer Dari and Mr. Benjamin Walker of these research groups. I wish to gratefully remind wonderful insight and collaboration I gained from Dr. Neng Li, Dr. Altaf Hussain, and Dr. Ma Li. I also wish to convey my deepest gratitude to Prof. Leela Rakesh for her moral support in a difficult period at CMU.

I would like to thank all the members of my dissertation committee for their valuable comments to my work and kindly serving on my committee.

My family has been an immeasurable strength throughout my life. I would thank my father for being my greatest mentor and at times editor in so much of the work I have done, and my mother for being my strength when I was at my weakest. I thank my brother Shanaka Dharmawardhana for editing all my unprofessionally written codes. I wish to thank my sister Chathuri Dharmawardhana for all her help during my long graduate life. The academic and moral support from the best of my friends Suranga Caldera, Rajith Madushanka, Dr. Rukshan Perera, Suneth Kalapugama and Dr. Nalinda

Almeida are remembered with deepest gratitude. A special thanks go to Morgan and TJ Erikson for making me a home away from home. Last but not least I'd like to thank my uncle Chandrapala for teaching me math all those early years when I was not motivated to do so. There are far too many friends that helped me in every twist and turn of a rather rocky graduate career to be mentioned in person. However, I am grateful to all of them and will remember their support until such time I forget myself.

Finally I would like to thank the Department of Physics and Department of Geosciences of University of Missouri-Kansas City, the Department of Physics of Central Michigan University, the U. S. National Science Foundation (NSF), U. S. department of energy (DOE), the University of Missouri Bioinformatics Consortium computing facility and the National Energy Research Scientific Computing Center (NERSC) for their support in many ways.

DEDICATION

I dedicate this work to my parents, brother, sister and uncle.

It is difficult to say what is impossible, for the dream of yesterday is the hope of today and the reality of tomorrow.

Robert H. Goddard

US physicist & pioneer rocket engineer (1882 - 1945)

CHAPTER 1

INTRODUCTION

In the present day world, humans show insatiable appetite to discover new materials for achieving better living conditions. They find limited use of natural materials and understand limits in converting those into products. As an example, Clay was used to build houses initially but, with the increase in need for better comfort, they found lime and lime mixtures for construction of houses. They later found crude oil with very limited use and eventually separated diesel and gasoline to have extensive use. Iron ore was found and managed to be converted into iron with few uses. However, uses were multiplied when this very same iron was used to make steels. In this endeavor, material scientists played a major role in achieving a higher standard of living for humans. However, it probably took many decades to develop better materials using trial and error techniques with limited facilities available. The industrial revolution changed the amount of time it took for new inventions to be created as experimentation was entered into material development within laboratory conditions. This experimentation, thus the development of theories, brought materials with various characteristics into everyday use. Development of more materials motivated the design of new products and provided improved standard of living for human kind. Thus today's material science combined with a number of branches of sciences and a coordinated effort of highly qualified and experienced scientists working in well-equipped laboratories all over the world to invent new materials leading to never ending demand for new products and services. This effort developed both theoretical insight and experiences leading to new techniques

which reduce the amount of time required for development and improving sophistication¹.

Ever increasing demand for new materials increases pressure on cost and time reduction on material development thus; traditional methods such as trial and error and combinational synthesis methods are not good enough for current needs. These traditional methods consume a lot of resources in laboratories and the time of specialists thus; provide motivation for development and use of new techniques to bridge the gap.

Application of quantum mechanics and use of computer simulations are the techniques that provide help in order to reduce the gap. The speed and versatility of computer simulations using theories to build models gained much popularity among present day material researchers. Computer simulations are much more cost effective, fast and satisfy current needs ².

There is no single theory to simulate every type or aspect of material. Thus for effectiveness, the simulation of models is multilevel in time and length scales. Density functional theory (DFT) is one such theory with much recognition among researchers in order to build models for simulation. *Ab initio* simulation technique has gained much recognition among the research community owing to its cost effectiveness and versatility ³. Moreover, this method is more suitable for larger systems with complicated structures which are not easily accessible through experimentation. It is worth it to note that some achievements in this work using DFT in material development in complicated problems were unattainable with other methods ¹.

This study intends to use DFT and *ab initio* techniques with a bottom up approach which is rarely used for studies in the past with material genomic approach to generate data for analysis and drawing meaningful conclusions. Current study used DFT technique to investigate a special class of compound that is cement which was investigated over a long period but still not very well understood. The focus of the study is on main binding phases of cement identified as “calcium silicate hydrate” (CSH) and “calcium aluminosilicate hydrate” (CASH) ⁴.

As DFT is primarily a ground state theory, it is not possible to directly apply it to simulate temperature and pressure dependent studies. However, it is possible to simulate dynamics within the classical theory of mechanics and adopting DFT in an approximate form to mimic atomic level properties for high temperature and high pressure conditions of materials. These simulations are called as *ab initio* molecular dynamic approach (AIMD). The material of choice for this task is Mo-Si-B system. More detail will come under subsections for each of these separate phases. Objectives of the study are to be shown at the end of the **chapter 1**.

Application of various *ab initio* methods to solve real word problems are in many reviews and books ^{1, 5}. Those applications used different types of complex materials. Similarly the materials used for this study broadly fall into two categories: 1) inorganic and 2) intermetallic compounds. In structural perspective, all these materials are in crystalline form. Following subsections will introduce and elaborate on different material systems used in this study.

1.1 Introduction to cement and C(A)SH

Portland cement is one of the oldest and most utilized construction materials in the history of humankind and its usage entails a significant environmental, social, and economic impact. It is essentially the 'glue' of the concrete part of the built environment. The yearly production exceeds 2 billion metric tons and is rapidly increasing with the development of geographical regions such as Asia. Cement based materials are gradually broadening its applicability and venturing into many other areas of technology. Some of the non-conventional applications are refractory materials, waste storage (especially for radioactive waste), biomaterials, rapid prototyping etc. On the other end of the spectrum, manufacture of cement is also responsible for 5%-7% of manmade CO₂ per annum ⁶ thus contributing to global warming. To optimize the said applications and to avoid the adverse effects, most cement researches in the past century concerned on the macro scale structure and dynamics. However, in order to achieve comprehensive insight on properties, the need is to focus on the study of microstructure and morphology at the atomic scale of cement paste. Thus, atomic scale structure and properties of C(A)SH formed as hydration products of cement powder attract intense interest owing to the role they play in the performance of Portland cement and its potential modifications.

However, that vision is far from the reality. The cement paste is a complex multicomponent and heterogeneous composite, with different structural features at different length scales. When the clinker (cement powder) is in contact with water it becomes a hardened paste that undergoes hundreds of chemical reactions and physical processes. X-ray diffraction (XRD) data suggests that the major component of

the cement paste, the C-S-H gel, is amorphous with varying degree of intrinsic porosity. However, experiments are unable to highlight complete information regarding its atomic structure thus leading to incomplete insight on the atomic structure of C-S-H gel. The past studies show that C-S-H gel has a layered structure, at short length scales (1 to 5 nm) and the layers stack to form compact domains in which the distance between individual C-S-H layers is in the order of a few nanometers, i.e. the same order as the interlayer distance in a Tobermorite or Jennite crystals ⁴. At larger length scales (5 to 100 nm), these ordered stacks form three dimensional structures called C-S-H particles. Transmission Electron Microscopy (TEM) revealed that the actual C-S-H particle is disk shape and has a thickness of 5 nm with the long axis in the 60 nm range. During hydration these C-S-H particles multiply and aggregate to form low-density and high-density C-S-H gel at the micro length scale ⁷. This difficulty in characterizing C-S-H and the increasing availability of computational resources and methods motivated the development of many models.

There are two main models accepted for the C-S-H microstructure. The widely accepted model of Taylor ⁸ suggests that C-S-H is a single solution composed of nanometer-sized components of structurally imperfect tobermorite and jennite (T/J model). The main structural feature in tobermorite and jennite is a silicate tetrahedra chain of wollastonite type (so called “dreierkette”). There are two types of “imperfection” of tobermorite structure: (1) missing of bridging tetrahedra in the chains and (2) missing chains in the structure (substituted by hydroxyl groups). These defects are the source of large variations of Ca/Si (C/S) ratio from 0.75 in tobermorite to 1.5 in jennite. According to this model, a gradual formation of the dreierketten occurs through the condensation

of monomer to dimer, dimers to trimmers, etc. With the availability of powerful computers, many attempts were made to model microstructures in C-S-H to account for the elastic behavior, hydration, transport properties, aging.... etc. A few of the more successful models include HYMOSTRUCT⁹, NIST¹⁰, DUCOM¹¹, HydratiCA¹². On the other hand, a limited number of atomistic simulations aimed at having a realistic structure for the cement gel also appeared, mostly based on tobermorite and jennite structures. One of these studies used a Monte Carlo technique to study the electrostatic attraction between charged surfaces with a similar environment found in the interlayer of tobermorite-like structures ¹³. Several such studies have resulted in the development of quality classical potentials suitable for cement research ¹⁴. Classical molecular dynamic (MD) simulations are also used to study the polymerization of silica with the presence of $\text{Ca}(\text{OH})_2$ to build a molecular model from the bottom-up ¹⁵.

More importantly all models proposed in the literature lack consistency at least partially with experimental observation. They explain some types of experimental results and contradict with the others. Almost all models are for C-S-H and ignore the main substituent of the cement, i.e Aluminum (C-A-S-H). Thus, any model must account for both C-S-H and C-A-S-H to gain an accurate understanding and be consistent with the experiment as it is impossible to separately characterize the different phases of the cement gel. To circumvent most of these difficulties, an impressive review by I. G. Richardson ¹⁶ proposed a series of structures (Richardson-2014 models) that are both consistent with the experiment and chemically plausible for a part of cement gel known as C-S-H (I). This is the first most successful attempt to model real cement and it gives the opportunity to understand the fundamentals of cement. Also, this work intendeds to

extend the C-S-H models to include Aluminum and hence predict C-A-S-H model as well. This thesis will study some of these hypothetical models to ascertain the validity and applicability of Richardson-2014 models and to test the extension to the aluminosilicate phases.

A key point missing in all those efforts is the understanding of bonding characteristics of C(A)SH and the models for C-S-H and C-A-S-H. Due to the complexity of CSH structures, quantitative bonding information, especially H-bonding, cannot be obtained purely from experimental means without the aid of robust atomistic model for proper interpretation, giving rise to the proverbial chicken-egg problem. In the light of this critical gap in knowledge, it is of paramount importance to investigate a wide variety of crystalline C(A)SH phases with well-documented crystal structures. Such studies will provide an in-depth insight on the variations in bonding characteristics in relation to the composition and structures of these materials. In the absence of such understanding, the atomistic models proposed in the literature remain speculative. Moreover, the data obtained from crystalline phases can help to construct more realistic models that are consistent with both electronic-scale and atomistic-scale behaviors for C(A)SH phase in hardened Portland cement.

1.2 Introduction to intermetallic high temperature superalloys

In high temperature environment, the most essential requirements for a structural material, aside from the obvious requirement of high melting point are; high strength and stiffness, high oxidation resistance, adequate room temperature mechanical properties and cost effectiveness. Traditionally titanium aluminides and nickel based

superalloys were used for high temperature applications, but are quickly losing ground due to the ever increasing demand for higher operating temperatures. New materials for ultrahigh temperature machinery will not only increase their life cycle but also reduce the high energy cost of elaborate cooling systems as recurring costs. Transition Metal (TM) based 5-3 silicides have gained attention, especially T1 and T2 phases as replacement for existing Ni based super alloys ¹⁷.

The TM silicide Mo_5Si_3 (T1) and Mo_5SiB_2 (T2) are more suitable for this application. The T1 phase has a very high melting point (2180 °C) and excellent mechanical strength at high temperature. The T2 phase also has excellent mechanical strength at high temperatures and good oxidation resistance and creep resistance. Thus, response and strength of these materials at high temperatures need investigation to gain fundamental understanding. The elastic properties and hence mechanical properties at high temperature are difficult to measure via experimental methods. Moreover, there were many attempts to extend the theoretical approach to simulate and predict high temperature mechanical properties for various materials. However, those attempts were extrapolation techniques and based on the ground state calculations. Using T1 and T2 as test cases this study intends to test the possibility of using ground state DFT and *ab initio* molecular dynamics to simulate and predict high temperature mechanical properties. This will perhaps enable scientists to identify the origin and possible remedy for the thermal expansion anisotropy of the T1 phase.

The high thermal expansion anisotropy of T1 phase may also be reduced via alloying. There are many experimental and theoretical studies that suggest vanadium as a possible alloying agent to achieve this objective. A computational approach to test and

understand the effect of alloying on thermo-mechanical properties of the T1 phase is much economical than experimental testing. This study thus expect using AIMD to test Mo-V-Si and Mo-Si-Al alloying series in order to identify and reduce, the thermal expansion anisotropy of the T1 phase Mo_5Si_3 ¹⁸.

The material on focus in this thesis is CASH phases leading to understand a realistic structural model for cement. As the modeling of cement at this scale is at its infancy AIMD techniques that would be of interest cannot directly be applied so far. The application of these methods to the intermetallic compounds as a test case will be a stepping stone for much elaborate simulations of CASH phases in the future. One may also acknowledge the structural similarities of both these class of materials. Above mentioned structural anisotropy is a common feature for CASH as well as TM silicides. Thus, the techniques used in TM silicide in theory, should be transferrable and may prove important to be used in CASH phases as well.

1.3 Outline of thesis

The thesis broadly divided into two parts.

Part I: deals with the use of DFT to gain fundamental understanding of C(A)SH via a sizable selection of well-known cement minerals. Essentially, Initial work will consider 4 most important CSH crystals in cement literature to get an understanding of the chemical bonding and broad electronic properties. This knowledge promotes to work on much larger sample of 20 crystalline minerals to obtain fundamental insight previously not known about the field in general. Also Richardson-2014 models proposed recently

needs theoretical justification through careful analysis of natural crystals. The culmination of this study is the fundamental understanding of bonding of structurally known CSH to justify these hypothetical models based on vast experimental observations.

Part II: deals with the application of AIMD approaches to gain insights on high temperature mechanical properties of intermetallic and to predict new materials that has improved mechanical properties at high temperature. Also AIMD approaches are utilized to understand and predict the alloying effect on TM compounds to alleviate some mechanical deficiencies. The theoretical tools discussed and implemented in this section can be of great interest to the material discussed in **Part I** and may be used in the future.

CHAPTER 2

THEORY AND METHODOLOGY

This chapter is dedicated to lay out the theoretical framework that underpins research effort. The density functional theory (DFT) provides this need. DFT starts from the Schrödinger's equation for a many-body system. The molecular dynamics (MD) theory similarly underpins research on high temperature properties presented in chapter 7 and 8. The instruments used to investigate materials and their properties in this study are DFT based packages called Vienna Ab initio Simulation Package (VASP) and Orthogonalized Linear Combination of Atomic Orbitals (OLCAO). Further, this chapter explains the introductory description to the theory and the specific methodologies used for collection of data for this dissertation. First principles (FP) or popularly known as *ab initio* formulations are used to calculate total energy, forces, structure and properties of solids liquids and gasses. There are many other empirical and semi-empirical approaches which were popular for decades are replaced by these *ab initio* methods due to transferability and reliability.

2.1 Density functional theory

The DFT is the most widely used quantum mechanical approach in physics, chemistry biology, mineralogy, engineering and other related areas to understand the structure and property of materials and optimize them. Before getting into the DFT, it is necessary to establish the fundamental theory of quantum mechanics relating to many body problem. The first postulate of quantum mechanics is that all the information about

a given system is contained in the system wave function; Ψ . Objective here is to find the electronic wave function of solids. The nuclear degrees of freedom, for example the crystal lattice in a solid; only appears as an external potential acting on electrons as stated in Born-Oppenheimer approximation ¹⁹. This is well established in condensed matter physics. For a non-relativistic many electrons moving in a potential $v(\mathbf{r})$, the Schrödinger's equation and wave function will take the general form as follows:

$$\left[\sum_i^N \left(-\frac{\hbar^2 \nabla_i^2}{2m} + v(\mathbf{r}_i) \right) + \sum_{i<j} U(\mathbf{r}_i, \mathbf{r}_j) \right] \Psi(\mathbf{r}_1, \mathbf{r}_2 \dots \mathbf{r}_N) = E \Psi(\mathbf{r}_1, \mathbf{r}_2 \dots \mathbf{r}_N) \quad (2.1)$$

Where, N is the number of electrons and in addition to **Equation (2.1)** the electron-electron coulomb interaction is given by the $\hat{U}(\mathbf{r}_i, \mathbf{r}_j)$. For non-relativistic system, an operator for each term is given as follows:

$$\hat{T} = -\frac{\hbar^2}{2m} \sum_i \nabla_i^2 \quad (2.2)$$

$$\hat{V} = \sum_i v(\mathbf{r}_i) = \sum_{ik} \frac{Q_k q}{|\mathbf{r}_i - \mathbf{R}_k|} \quad (2.3)$$

$$\hat{U} = \sum_{i<j} U(\mathbf{r}_i, \mathbf{r}_j) = \sum_{i<j} \frac{q^2}{|\mathbf{r}_i - \mathbf{r}_j|} \quad (2.4)$$

Where, $Q_k (= Z_k e)$ is the nuclear charge, $q_i (= e)$ is electronic charge, \mathbf{r}_i are electron positions and \mathbf{R}_k are atomic positions. Solving **Equation (2.1)** exactly is impossible even with the present knowledge of mathematics and sophisticated computing power. Since early 20s relentless effort has been spent on developing methods at least approximately to solve the many-body Schrödinger's equation. Some of such methods are Hartree-Fock, perturbation theory, Green's functions and configuration interaction... etc. However, all these wave function based methods have a prohibitively high computational cost for systems even with 50 atoms ^{5b}. Thus, for real world applications where the system size of interest is much larger, DFT is the method

of choice, although less accurate as it may be. DFT recognizes that for nonrelativistic coulomb system, the particle density $n(\mathbf{r})$ completely describes the many body wave function $\Psi(\mathbf{r}_1, \mathbf{r}_2, \dots)$, thereby effectively reducing the degrees of freedom. This reduces the computational burden significantly. DFT approach can be then summarized in the following sequence.

$$n(\mathbf{r}) \Rightarrow \Psi(\mathbf{r}_1, \mathbf{r}_2, \dots, \mathbf{r}_N) \Rightarrow v(\mathbf{r}) \quad (2.5)$$

Thus, the knowledge of $n(\mathbf{r})$ implies the wave function and hence the potential. Once these are known, all observables can be obtained with the appropriate Hermitian operators.

The origin of DFT starts with the *first Hohenberg-Kohn (HK) theorem*²⁰. This states that the ground state wave function $\Psi_0(\mathbf{r}_1, \mathbf{r}_2, \dots)$ uniquely corresponds to the ground state $n_0(\mathbf{r})$. Thus the system is uniquely described by the density which effectively reduces the degrees of freedom reducing computational cost. This means the ground state energy (E_0) and all the ground state observables are a functional of $n_0(\mathbf{r})$. If Ψ_0 can be calculated from $n_0(\mathbf{r})$ and vice versa, both functions are equivalent and contain exactly the same information. Thus equation can be presented as

$$E_{v,0} = \min_{\Psi \rightarrow n_0} \langle \Psi | \hat{T} + \hat{U} + \hat{V} | \Psi \rangle \quad (2.6)$$

The ground state density n_0 provides the ground state wave function and the ground state energy $E_{v,0}$ in potential $v(\mathbf{r})$. The external potential $v(\mathbf{r})$ is similar to **Equation 2.3** According to variational principle, any n different from n_0 provides an $E[n]$ that is larger than the $E_{v,0}$. Thus provides a technique to obtain the ground state energy. This is sometimes referred as *second Hohenberg-Kohn theorem* and perhaps the most important practical application of DFT.

The Kohn-Sham approach

The theoretical framework provided by Hohenberg-Kohn above provides a rigorous foundation for electronic structure and other related property calculations for atoms and molecules. This framework was in use many ways over past 40 years. Among them Kohn-Sham approach is the most widely use technique. Kohn-Sham, instead of working exclusively in terms of the particle (or charge) density, brings back the single-particle orbitals (wave functions ϕ_i) back to the game without compromising the rigorous theoretical frame work of Hohenberg and Kohn. As a consequence, Kohn-Sham approach then looks formally like a single-particle theory, albeit many-body effects are still included via exchange-correlation functional. Kohn-Sham scheme starts with writing the minimization as

$$0 = \frac{\delta E[n]}{\delta n(\mathbf{r})} = \frac{\delta T_s[n]}{\delta n(\mathbf{r})} + \frac{\delta V[n]}{\delta n(\mathbf{r})} + \frac{\delta U_H[n]}{\delta n(\mathbf{r})} + \frac{\delta E_{xc}[n]}{\delta n(\mathbf{r})} = \frac{\delta T_s[n]}{\delta n(\mathbf{r})} + v(\mathbf{r}) + v_H(\mathbf{r}) + v_{xc}(\mathbf{r}) \quad (2.7)$$

In this **Equation (2.7)**, $T_s[n]$ is the kinetic energy of a nonintegrating system of particles, similar to **Equation (2.2)** given in terms of orbitals as follows.

$$T_s[n] = -\frac{\hbar^2}{2m} \sum_i^N \int d^3r \phi_i^*(\mathbf{r}) \nabla^2 \phi_i(\mathbf{r}) \quad (2.8)$$

Where $\phi_i(\mathbf{r})$ is single particle orbital of noninterating system and the Hartree potential $v_H(\mathbf{r})$, corresponding to **Equation (2.3)** above, is given as follows.

$$v_H[n](\mathbf{r}) = q^2 \int d^3r' \frac{n(\mathbf{r}')}{|\mathbf{r} - \mathbf{r}'|} \quad (2.9)$$

$V_{xc}(\mathbf{r})$ is termed the exchange-correlation potential and will be explained later. Suppose a system of noninterating particle system moving under potential $v_s(\mathbf{r})$, where

$$v_s(\mathbf{r}) = v(\mathbf{r}) + v_H(\mathbf{r}) + v_{xc}(\mathbf{r}) \quad (2.10)$$

Kohn-Sham formulation says that the density $n_s(\mathbf{r})$ obtained by solving the hypothetical noninteracting system under $v_s(\mathbf{r})$ is exactly same to the density $n(\mathbf{r})$ obtained by **Equation (2.7)**. Thus the Schrödinger equation for this hypothetical non-interacting (auxiliary) system is in $V_s(\mathbf{r})$ is presented as;

$$\left[-\frac{\hbar^2 \nabla^2}{2m} + v_s(\mathbf{r}) \right] \varphi_i(\mathbf{r}) = \varepsilon_i \varphi_i(\mathbf{r}) \quad (2.11)$$

This **Equation (2.11)** yields single particle orbitals that yield the density $n(\mathbf{r})$, which is given as follows.

$$n(\mathbf{r}) \equiv n_s(\mathbf{r}) \equiv \sum_i^N f_i |\varphi_i(\mathbf{r})|^2 \quad (2.12)$$

Where, number f_i is the occupation number of the i^{th} orbital φ_i . The **Equations (2.10) – (2.12)** are known as the Kohn-Sham (KS) equations. This effectively replaces the functional minimization of $E[n]$ to that of solving noninteracting Schrödinger equation.

The only term unexplained in **Equation (2.10)** above is the exchange-correlation potential. This needs to be treated carefully in DFT as it includes the effects of interaction which was effectively removed from other terms of the potential. The $v_{xc}(\mathbf{r})$ can be decomposed as $v_x(\mathbf{r}) + v_c(\mathbf{r})$ to separate the exchange and the correlation potential. $v_x(\mathbf{r})$ is due to Pauli principle (exchange energy). This is due to indistinguishability of particles. It's a unique quantum phenomenon that has no classical analogue. The exchange term has no direct particle density analogue. This works well in KS approach because orbitals are explicitly used. The correlation potential on the other hand, has a general expression neither in terms of orbitals nor in terms of density. The correlation in general terms can be thought of as the mathematical concept of non-independent events. It's also seen in classical systems especially in statistical physics.

The simplest way to understand the correlation energy in DFT is to understand the orbital picture of KS and many other formalisms. The main assumption in these methods is that the many-body wave function is approximated as a product of single-particle orbitals. Thus the correlation energy can be defined as the difference between true ground state energy obtained from the many-body wave function and the energy obtained by the antisymmetrized product of single-particle orbitals. Since a general expression does not exist various approximations have been proposed. Finding functional forms for v_{xc} for different materials and applications is an active area of study. Any DFT calculation has to specify the approximation used for the correlation potential. This thesis uses two most popular approximations. First of this is the local density approximation (LDA). Historically LDA is the most important approximation for xc potential. The LDA is approximated assuming the per-volume exchange-correlation energy ($\epsilon_{xc}[n(r)]$) for the homogeneous electron liquid ^{21, 5a} density $n(r)$ given as follows.

$$v_{xc}[n] = \int \epsilon_{xc}[n(\mathbf{r})] n(\mathbf{r}) d\mathbf{r} \quad (2.13)$$

This approximation has endured the test of time, although as crude as it is, giving amazingly good results for many materials. Success of LDA is partially attributed to cancellation of systematic errors ^{5b}. It gives good estimation for the V_{xc} because of the overestimation of the exchange energy and the underestimation of the correlation energy. Thus for numerous solid systems where rapid changes in electron density do not occur, LDA is the method of choice because of the low cost compared to other approximations. In this thesis for the OLCAO calculations (see section 2.2) LDA approximation is used.

To make up for LDA deficiencies many other functionals have been proposed for exchange-correlation potential. Thus to account for the local density variations, many gradient corrected techniques are proposed. These are commonly known as generalized gradient approximations (GGA)²² and have the following functional form.

$$v_{xc}^{GGA}[n(\mathbf{r})] = \int d\mathbf{r} f(n(\mathbf{r}), \nabla n(\mathbf{r})) \quad (2.14)$$

Where $f(n(\mathbf{r}), \nabla n(\mathbf{r}))$ is an explicit functional of both local density and its gradient accounting for small local changes in electron density. Most popular GGA implementations are PBE and B3LYP²³, Becke's exchange functional²⁴... etc. This work, we exclusively use PBE for all calculations using VASP (see section 2.3).

The theoretical framework described in this section outlines the basics of DFT but specific to the methods used in this thesis. This should sufficiently reveal methods, and software used to collect data and do necessary computations in Section 2.2 and 2.3. Here by no means intended to provide a comprehensive review of DFT and its applications. Interested reader may find many excellent reviews, and books which describe theoretical rigor and broadness of the field⁵.

The theoretical framework discussed above is implemented in the packages Orthogonalized Linear Combination of Atomic Orbitals (OLCAO), and Vienna ab initio Simulation Package (VASP) which are the two most important tools for all the calculations done in this thesis. The differences of these packages and the specific implementations will be discussed in brief in Section 2.2 and 2.3. The geometric optimization of all systems was done using VASP. Then the optimized structure was used in OLCAO for the electronic structure calculation to obtain the electronic and bonding properties. They used different basis sets and the combination of these two

packages were well suited and successfully demonstrated in many recent publications

25

2.2 The orthogonalized linear combination of atomic orbitals (OLCAO) Method

For this work OLCAO is used to obtain electronic structure and bonding information. It was very successful in collecting data and efficient calculation of electronic and some optical properties of most materials. In particular it is suitable for very large and complex systems, thus is the root of its success of OLCAO. It is developed and maintained by Prof. Wai-Yim Ching and Prof. Paul Rulis of University of Missouri – Kansas City. OLCAO use the LDA approximation for exchange–correlation potential explained in Section 2.1. This method uses a linear combination of atomic orbitals to construct the solid state wave function. The atomic orbitals are made up of radial and angular part. The radial part is expanded as a linear combination of Gaussian type orbitals (GTO). Angular part is represented by the spherical harmonics $Y_{l,m}(\theta,\varphi)$. The most important feature of OLCAO is the core orthogonalization which reduces dimension of the secular equation. For this reason OLCAO is suitable for large and complicated material systems. Thus, OLCAO was used for study leading to this thesis as it deals with most complicated inorganic and metallic systems.

OLCAO is capable of obtaining various electronic properties important for this study. These electronic properties, are band structure, total and partial density of states (DOS), effective charge and bond order. Band structure is one important property in a solid state calculation as it shows the energy as a function of k-points in reciprocal space. The k-points are chosen along the high symmetry points in the Brillouin Zone

(BZ). The energy gap between valance band (VB) and conduction band (CB) characterize the nature of the material as a metal, a semiconductor or an insulator. This study deals with both insulator in case of CASH and metals in case of intermetallic compounds described in Chapter 1. Although both are structural materials, electronic nature is vastly different. The DOS represents the number of states an electron has access for a given energy which is another representation of band structure. The DOS, $G(E)$ is expressed by following equation.

$$G(E) = \frac{\Omega}{(2\pi)^3} \frac{d}{dE} \int_{BZ} d\mathbf{k} = \frac{\Omega}{(2\pi)^3} \int_{BZ} \frac{dS}{|\nabla E|} \quad (2.15)$$

Where, Ω is volume of the unit cell and integral is over the constant energy surface in Brillouin Zone (**BZ**). The DOS can be resolved into partial DOS (PDOS) for atoms and orbitals.

The most important for this work is the analysis of bonds to find the origins of cohesion, strength and in general the nature of the material that is the bond order (BO). Bond order, used in physics community refers to the charge distribution between the pair of bonds. The evaluation of BO values (overlap population), $\rho_{\alpha\beta}$, between any pair of atoms (α , β) is based on Mulliken population analysis ²⁶:

$$\rho_{\alpha\beta} = \sum_{n,occ} \sum_{i,j} C_{i\alpha}^{*n} C_{j\beta}^n S_{i\alpha,j\beta} \quad (2.16)$$

Where i, j label the orbital quantum number and n the band index, $C_{j\beta}^n$ are the eigenvector coefficients of the wave function and $S_{i\alpha,j\beta}$ is the overlap matrix between atoms α and β ^{25a}. The BO value $\rho_{\alpha\beta}$ is a direct quantitative measure of strength between a pair of atoms.

Although BO is not a quantum observable, it is far more accurate and concise than pure geometric criteria or other parameters such as coordination numbers.

Mulliken scheme is basis dependent and its application must be confined to a specific method and a well-defined basis set. It is most effective when a more localized minimal basis set is used ²⁶. OLCAO has the flexibility to use different set of basis expansions depending on the objective of the calculation. In this present study, the BO was calculated using a minimal basis (MB) set whereas for the self-consistent potential and the electronic structure calculation, a full basis (FB) set was used. These are carefully constructed and well-tested basis set for each atom within the data base of the OLCAO package ^{25a, 27}. The MB consists of the core orbitals of the atom and the orbitals of the valence shell. However, FB has one more shell of the higher unoccupied orbitals. For example, the MB of Si consists of 9 atomic orbitals (1s, 2s, 2p_x, 2p_y, 2p_z, 3s, 3p_x, 3p_y, 3p_z) and the FB has 18 orbitals (MB plus 4s, 4p_x, 4p_y, 4p_z, 3d_{xy}, 3d_{yz}, 3d_{zx}, 3d_{2-y2}, 3d_{3z2-r2}) ^{25a}. Although there are other more elaborate methods to calculate BO values, they are usually limited to simple crystals or small molecules based on numerical evaluations of BO on 3-dimensional mesh. Such methods are usually more onerous and less efficient when apply to multi-component materials with complex structures and large number of atoms. The total bond order density (TBOD) is the cumulative BO from all unique bond pairs divided by the cell volume. Analysis of the material systems in the present study were enriched by partial bond order density (PBOD). This is defined as the cumulative BO from each unique species of bonds divided by the cell volume.

2.3 Vienna *ab initio* simulation package (VASP)

The Vienna *ab initio* Simulation Package (VASP) ^{28, 29} is a popular quantum mechanical calculation package used primarily in condensed matter physics and

materials engineering. It is mostly used as a DFT package but possible to use in Hartree-Fock approximation to solve the many body Schrödinger equation. VASP is also capable with many types of XC functionals including LDA, PBE and hybrid functionals. It uses a plane wave basis set implemented by two main techniques. First, is the projector augmented wave (PAW) method ^{30,31} and second, ultra-soft pseudo-potential method (USPP) ^{32,33}. The former is much accurate but more expensive than later. For all the VASP calculations done, study used PAW_PBE method unless specifically stated otherwise. VASP is very efficient for parallel calculations which allows for large systems of the order of hundreds or 1000 of atoms. For the systems as complex as C-A-S-H and intermetallic systems considered in this thesis, VASP is most suitable method. It uses the blocked Davidson algorithm and RMM-DIIS for efficient electronic structure convergence to obtain ground state energy.

2.3.1 Geometric optimization

The initial step to ascertain any preferred properties, it is necessary to have insight on atomic structure. The crystal structures reported in literature, often had obtained by XRD techniques and are not possible to use owing to the inherent difference of DFT optimized structure with the experimental structure. DFT optimized structure will typically differ by 5-10% in lattice constants compared with the experiment structure. Thus, initial geometric optimization is an important step. For the large crystals considered in this thesis, an efficient geometric optimization is crucial and VASP is an attractive option in this regard. VASP calculates the Pulley correlated Hellmann-Feynman forces on ions after every the SCF cycle to generate the force on ions and

stress tensor of the simulation cell. Then a quasi-Newton algorithm is used to move ions to optimize the structure. This method is very fast but may not be ideal for bad initial structures. For such cases conjugate-gradient approximations is better though slower to find structures of the crystals. Thus this study used either of or both these techniques depending on the quality of the crystal structure reported in literature. The specifics will be given as needed in the results section. Defining K-points is also an important factor to obtain quality results. Choosing K-points in each direction depends on the size of the cell and the type of material. Number of K-points has a linear scaling with the computational cost. Thus, number of K-points is described in the computational detail section of each chapter.

Any VASP calculation requires 4 main input files. These are INCAR, KPOINTS, POSCAR and POTCAR. INCAR defines the calculation type and parameters needed for the calculation. KPOINTS defines k-point mesh and POSCAR includes the initial positions. POTCAR includes the potential parameters depending on the type of potentials used and correspond to the order of elements defined in the POSCAR.

2.3.2 Elastic and mechanical properties calculations

This thesis focuses on construction material. The C-(A)-S-H is the construction material used mostly in room temperature and intermetallic compounds described in chapter 1 is a construction material used at high temperature. In this regard elastic and mechanical properties are the most important and interested of. This was described in chapter 1. Thus, simulating these properties is essential for this study. For C-(A)-S-H, mechanical properties has been used as a characterization tool to understand the

structure at micro/nano level. There are many techniques to obtain the elastic tensor of a crystal via *ab initio* calculations. Total energy approaches are most popular method but have deficiencies for elastically anisotropic materials. Thus the stress-strain method³⁴ was chosen for crystals as that was highly successful method in recent past. This method requires very accurate geometric optimization via VASP. Calculations were usually set at 10^{-6} eV for electronic convergence with high energy cutoff of 600 eV. The force convergence criterion was set at 10^{-5} eV/Å for each ionic step relaxation. The VASP relaxed crystal structures were used to calculate the 2nd order elastic tensors. A strain of +0.5% and -0.5% was applied to the cell to obtain the stress data σ_j . From the calculated σ_j data ($i, j = 1, 2, 3, 4, 5, 6$), the elastic coefficients C_{ij} are evaluated by solving following linear **Equation (17)**,

$$\sigma_j = \sum_{i=1}^6 C_{ij} \varepsilon_i \quad (17)$$

Percentage strain applied with careful selection. For hard material a smaller strain was chosen not to exceed breaking point of the material. For CSH 0.5% strain is a good choice. For metallic malleable materials, $\pm 1\%$ strain was applicable as smaller strains may run into numerical instabilities.

The averaged mechanical properties: K (bulk modulus), G (shear modulus), E (Young's modulus), and γ (Poisson's ratio) were then obtained based upon the Voigt–Reuss–Hill (VRH) approximation for polycrystals. The Voigt approximation³⁵ assumes a uniform strain in the structure and gives the upper limit of mechanical properties derived from elastic coefficients C_{ij} . In the Reuss approximation³⁶, a uniform stress distribution was assumed to get lower limit through elastic compliance tensor S_{ij} . The average of

these two limits, known as Hill approximation ³⁷, is usually taken as the reasonable representation of the calculated mechanical properties of a materials.

2.4 ab initio molecular dynamics (AIMD)

The ground state theory introduced in previous section has many applications and routinely used for wider areas. However, many real world problems deal with finite thermodynamic conditions such as temperature and pressure. For C-A-S-H the ground state calculation is good enough but for high temperature structural material a theory is needed that can capture the finite thermodynamic effects. In AIMD the forces are described within the framework of quantum mechanics, whereas the dynamics is captured in terms of classical dynamics and statistical mechanics. AIMD has given wide versatility to atomistic simulation that the phrase “virtual laboratory” was coined. There exist few different types of AIMD implementations. The first was the Ehrenfest molecular dynamics which solves the time-dependent Schrödinger equation “on-the-fly” as the nuclei are propagated using classical mechanics. This is a very expensive method thus limits applicability. Much better approach is to strictly adhere to Born-Oppenheimer approximation and separate electronic degrees of freedom and nuclei propagation. This is aptly called “Born-Oppenheimer molecular dynamics”. Thus, the electronic structure is reduced to solving time-independent Schrödinger equation self consistently. The forces at each step are calculated within Pulley correlated Hellmann-Feynman theorem. Then, the nuclei are propagated according to classical mechanics. This implies that the time dependence of the electronic structure is imposed and dictated by the parametric dependence of the classical dynamic of the nuclei which it simply follows. Thus, it is not

an intrinsic dynamics as stated in the Ehrenfest MD. Consequently the Born-Oppenheimer MD method can be readily stated as follows,

$$M_I \ddot{\mathbf{R}}_I(t) = -\nabla_I \min_{\Psi_0} \{ \langle \Psi_0 | \mathcal{H}_E | \Psi_0 \rangle \} \quad (18)$$

The Born-Oppenheimer MD is inherently costly because \mathcal{H}_E (**Equation 18**) must be minimized at each time step. However, for the problems dealt in chapter 7 and 8 the computational cost was still within reason.

All AIMD calculation in this thesis is done within “Born-Oppenheimer molecular dynamics” as implemented in VASP. Example INCAR related to the AIMD calculations and personalized scripts to filter AIMD data are given in **Appendix A**. A proper ensemble must be chosen depending on the problem at hand. In this thesis two ensembles were used. First is constant number of atoms, temperature and volume (**NVT**) and second, constant number of particles, temperature and volume (**NPT**). A typical INCAR from NVT calculation is given in **Appendix A.1**. Both problems explained in **Chapter 7 and 8** ideally should be done within **NPT** but, at the time of study in **Chapter 7**, the NPT was not implemented in VASP (version 5.2). The specific reasoning is given in **Chapter 7 and 8**. A typical INCAR from NPT calculation is given in **Appendix A.2**. From extraction of thermodynamic parameters such as temperature, pressure... etc if done by a code developed in this study called AIMD-data.pl and plotted using a aimd-plot.plt GNUplot script which is given in **Appendix A.3**. The methods applied in AIMD are different for the different problems in **Chapter 7 and 8**. The specifics of the methods are discussed in the respective chapters. However, it should be noted that a long term goal of using AIMD for the CASH will benefit immensely from the work discussed in **chapter 7 and 8**. The atomistic structure

determination of the CASH may not need the use of AIMD but to fully understand the dynamic properties like hydration and the production of clinker phases, AIMD will play very useful role.

CHAPTER 3

MECHANICAL ANISOTROPY AND INTERLAYER COHESION OF LAYERED CSH CRYSTALS

3.1 Introduction

Portland cement is one of the oldest and most utilized construction materials in the history of mankind and its usage entails a significant environmental, social, and economic impact. Hardened Portland cement paste derives its mechanical properties from the hydration products whose dominant fundamental component is the calcium silicate hydrate (CSH). With a growing desire to understand material behavior at the nanostructure scale, there has been significant interest in unraveling the CSH structure in cement paste in recent years^{38, 39, 40, 41}. In the past two decades, studies have indicated that CSH occurs as a combination of closely related mineral crystallites with a Ca/Si (C/S) ratio defined in terms of the ratio of the number of Ca and Si atoms varying from 0.6 to 2.0^{41, 42, 43, 4}. However, more recent theoretical and experimental studies seem to indicate that the CSH structure is far more complex and perhaps completely disordered^{39, 41, 44, 45}. Although CSH in cement paste has been researched for a long time, its atomic structure and electronic structures are still contested and largely unknown. Characterization and attributes such as precise atomic coordinates, partial occupancy, and the relationship of inter-layer bonding to the mechanical properties through experimental methods is extremely difficult for this class of material and therefore highly accurate computational modeling is necessary to obtain data that are otherwise unavailable. The information obtained from accurate calculations and

simulations can be used to investigate the important issue of long range interactions in such complex materials at much larger scale relevant to processing and macro scale properties. In particular, electronic structure results can provide useful information on electrostatic interaction between different particles or structures made of C-S-H crystals. The electrostatic interaction along with the polar and van der Waals interactions are three fundamental long range interactions that impact behavior at larger scale and need to be treated by a different level of theory ⁴⁶.

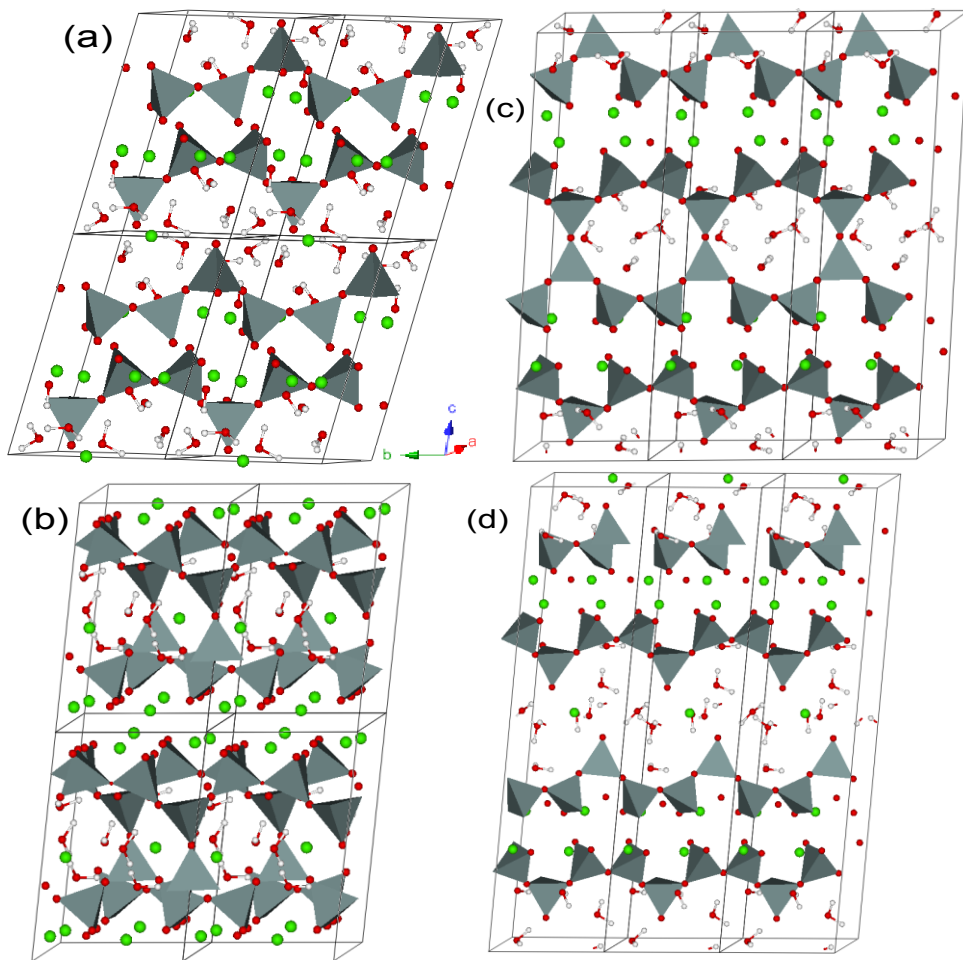


Figure 1. (color online) The (1x2x2) supercell of (a) jennite, (b)T9A and (1x3x1) supercell of (c)T11A (d)T14A.The atoms are indicated as: Ca-Green, O-Red, Silicate tetrahedra-Grey, and H-white.

In this chapter, it is reported that results from density functional theory (DFT) based *ab initio* calculations regarding the electronic structure, bonding, and mechanical properties of selected crystalline phases of CSH. This study focused in detail the following four crystalline phases: three tobermorite crystals (tobermorite 9Å (T9A), tobermorite 11Å (T11A), tobermorite 14Å (T14A))⁴⁷ and jennite⁴⁸, whose crystal structures are showed in **Figure 1**. These crystalline phases were chosen for the following reason: (1) they form the basis for the currently postulated cement paste CSH structure^{4, 41-43} (2) their crystal structures are available from previous studies⁴⁷⁻⁴⁸ and (3) they have very low symmetry with a large difference in C/S ratio and OH content which bears resemblance to the composition exhibited by the CSH cement paste. Calculations based on data revealed that the quantitative information on various types of bonding in these crystals including strong Si-O covalent bonding in the silicate network, substantial Ca-O ionic bonding, and inter-layer H-bonding, which makes a non-negligible contribution to interlayer cohesion. These data provide solid evidence that the concept of an overall bond order density (BOD) is far more relevant parameter for classifying different CSH crystal models than the most common approach of simply using the C/S ratio. Moreover, the study shows that the experimentally reported CSH crystal structures are not sufficiently accurate with regards to the water positions to properly assess hydrogen bonding and thus accurate structural relaxation using *ab initio* methods is necessary. Such information will be necessary for developing realistic nanostructure models of non-crystalline CSH that are believed to form hardened cement. This information is also critical for designing regimens needed for advantageously modifying Portland cement properties

for environmental and economic gains from the atomic-scales as articulated by recent investigators^{39, 49}.

3.2 Computational modeling details

The technical details of VASP relaxations (**Section 2.3.1**) for all crystal structures in this work are briefly outlined as follows: (1) The PAW-PBE potentials^{30, 50} used with the generalized gradient approximation (GGA); (2) electronic convergence criterion set at 10^{-6} eV; (3) the force convergence criteria set at 10^{-5} eV/Å for ionic relaxation; (4) a high energy cutoff of 500 eV is adopted with tests using 600 eV cutoff showing no discernible difference. (5) The *k*-point-meshes used are 2x3x2, 3x7x3, 4x4x1, and 4x4x1 for jennite, T9A, T11A and T14A respectively. The VASP relaxed crystal structures were used to calculate the elastic tensors for these four crystals using an efficient method discussed in section 2.3.2. This study chooses $\pm 1\%$ strain for calculating the elastic tensor within the framework of stress-strain method discussed in chapter 2. The electronic structure and bond order (BO) calculations were carried out using the OLCAO method as discussed in section 2.2.

3.3 Results and discussion

3.3.1 Relaxed crystal structures

The chemical formulae of the four crystalline phases studied are as follows: jennite $[\text{Ca}_9\text{Si}_6\text{O}_{18}(\text{OH})_6 \cdot 8\text{H}_2\text{O}]$, T9A $[\text{Ca}_5\text{Si}_6\text{O}_{17} \cdot 5\text{H}_2\text{O}]$, T11A $[\text{Ca}_4\text{Si}_6\text{O}_{15}(\text{OH})_2 \cdot 5\text{H}_2\text{O}]$ and T14A $[\text{Ca}_5\text{Si}_6\text{O}_{16}(\text{OH})_2 \cdot 7\text{H}_2\text{O}]$. These belong to the tobermorite and jennite families that

have many variations. Jennite is believed to be structurally similar to the later stage of the CSH hydration process in Portland cement with a relatively high C/S ratio of 1.5. It has a triclinic unit cell (space group P-1) ⁴⁸. Jennite has a layered structure (**Figure 1 (a)**) and three distinctive features. First there is a chain of Ca polyhedra running along the *a*-axis sandwiched between the silicate chains. Second, there are corner-shared silicate tetrahedral chains running along *b* direction. Third, the Ca polyhedra in the interlayer are connected to the silicate backbone (one Ca per unit cell) interwoven with water molecules. Bridging silicates on either sides of the interlayer are offset and not connected as in T9A, T11A. The tobermorite family of crystals is characterized by the fact that their basal spacing is related to the degree of hydration ^{47b, 51}. The three tobermorite classes T9A ^{47a}, T11A ^{47a} and T14A ^{47b} have basal separations of 9.3, 11.3, and 14 Å respectively in incrementing order of hydration. T9A, commonly known as clinotobermorite, is a triclinic crystal with C1 symmetry and five H₂O molecules, but no OH ions. T11A and T14A are monoclinic with space groups B11m and B11b respectively. All four crystals have their interlayer directions perpendicular to the *c* axis. Structurally, T9A has the same features as Jennite except the bridging tetrahedra are covalently bonded. Similar features are also apparent in T11A but there are no interlayer Ca polyhedra. T14A, on the other hand, is almost the same as Jennite except with a longer basal spacing.

Table 1 Experimental/Theoretical cell parameters for the jennite and tobermorite family of crystals.

| | | C/S | a (Å) | b (Å) | c (Å) | α° | β° | γ° |
|--|--------|------|---------|--------|---------|----------------|---------------|----------------|
| Jennite ⁴⁶ | Theory | 1.5 | 10.7307 | 7.3477 | 10.7884 | 103.20 | 94.81 | 110.24 |
| Ca ₉ Si ₆ O ₁₈ (OH) ₆ •8H ₂ O | Exp. | | 10.5760 | 7.2650 | 10.9310 | 101.30 | 96.98 | 109.65 |
| Triclinic/P-1 | %diff | | -1.46 | -1.14 | 1.30 | -1.88 | 2.23 | -0.54 |
| T9A ⁴⁴ | Theory | 0.83 | 11.3607 | 7.4068 | 11.4637 | 97.44 | 97.20 | 90.00 |
| Ca ₅ Si ₆ O ₁₇ •5H ₂ O | Exp. | | 11.2740 | 7.3440 | 11.4680 | 99.18 | 97.19 | 90.03 |
| Triclinic/C1 | % diff | | -0.77 | -0.86 | 0.04 | 1.75 | -0.01 | 0.04 |
| T11A ⁴⁴ | Theory | 0.67 | 6.7404 | 7.4511 | 22.6521 | 89.71 | 90.56 | 122.43 |
| Ca ₄ Si ₆ O ₁₅ (OH) ₂ •5H ₂ O | Exp. | | 6.7350 | 7.3850 | 22.4870 | 90.00 | 90.00 | 123.25 |
| Monoclinic/B11m | % diff | | -0.08 | -0.90 | -0.73 | 0.32 | -0.62 | 0.67 |
| T14A ⁴⁵ | Theory | 0.83 | 6.7012 | 7.4131 | 28.5517 | 90.64 | 92.48 | 122.66 |
| Ca ₅ Si ₆ O ₁₆ (OH) ₂ •7H ₂ O | Exp. | | 6.7350 | 7.4250 | 27.9870 | 90.00 | 90.00 | 123.25 |
| Monoclinic/B11b | % diff | | 0.50 | 0.16 | -2.02 | -0.71 | -2.75 | 0.48 |

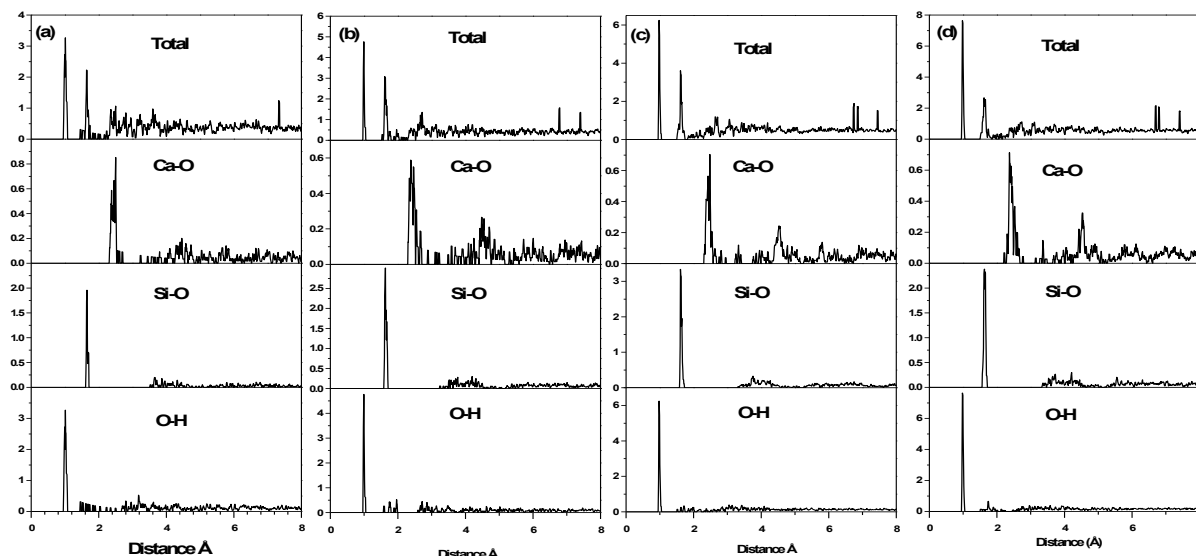


Figure 2. Total and Partial Radial Pair Distributions of (a) jennite, (b)T9A, (c)T11A and (d) T14A.

The relaxed structural parameters of the four crystals are listed in **Table 1**. They vary with reported experimental values by as much as 2.8%, which is larger than the usual differences between measured values and DFT calculations on simpler crystals. The large difference reflects the uncertainty in the experimental measurements, most likely due to the lack of high quality single phase samples of the complex CSH crystals. The structure of T14A as reported in literature^{47b} has partial occupancy of 0.5 for one of

the Ca sites and three water molecules. To account for the partial occupancy in the calculation, a full cell was used with removal of some atoms at the partially occupied sites to correctly match the experimentally observed stoichiometry. To appreciate complexity of these CSH crystals, **Figure 2** shows total and partial pair distribution functions (PDFs) for the four crystals. The two distinct peaks at 1Å and 1.6Å originate from covalent O-H bonds and Si-O bonds respectively. The Ca-O bonds are not prominent but can be seen as a broader peak around 2.6Å. This study finds no considerable deviation in average bond lengths compared to those reported in a recent paper about CSH nano-crystals³⁹.

3.3.2 Electronic structure of relaxed crystals

From VASP relaxed structures it is possible to calculate band structure using the OLCAO method. **Figure 3** shows the band structures of the four CSH crystals of jennite, T9A, T11A and T14A before (upper panel) and after (lower) relaxation. The zero of the energy was set at the highest occupied state. They are very different in terms of the presence of defect-like states and the location of HOMO (highest occupied molecular orbitals) and LUMO (lowest unoccupied molecular orbitals). CSH are inorganic crystals and generally expected to have a large band gap. The initial crystal structures were directly obtained from literature and H atoms for water added appropriately. T14A has additional complications of partially occupied sites as discussed above. The band structures of all four crystals after relaxation are much more realistic with clear band gaps. The main source of difference in the band structures between the unrelaxed and relaxed structures is the positions of the water molecules. In the x-ray diffraction

experiments^{47a, 47b, 48} the hydrogen bonding and water positions were determined somewhat arbitrarily using an empirical bond-valence scheme⁵². **Figure 3** show that jennite has an indirect band gap of 4.3eV. The top of VB is at M and the bottom of the CB is at Γ . All other crystals have relatively flat VB and hence direct band LDA gaps of 4.6 eV, 4.2 eV and 4.0 eV for T9A, T11A, and T14A respectively. Thus for the CSH crystals, it is necessary to accurately relax the measured crystal structure for electronic structure and bonding calculations.

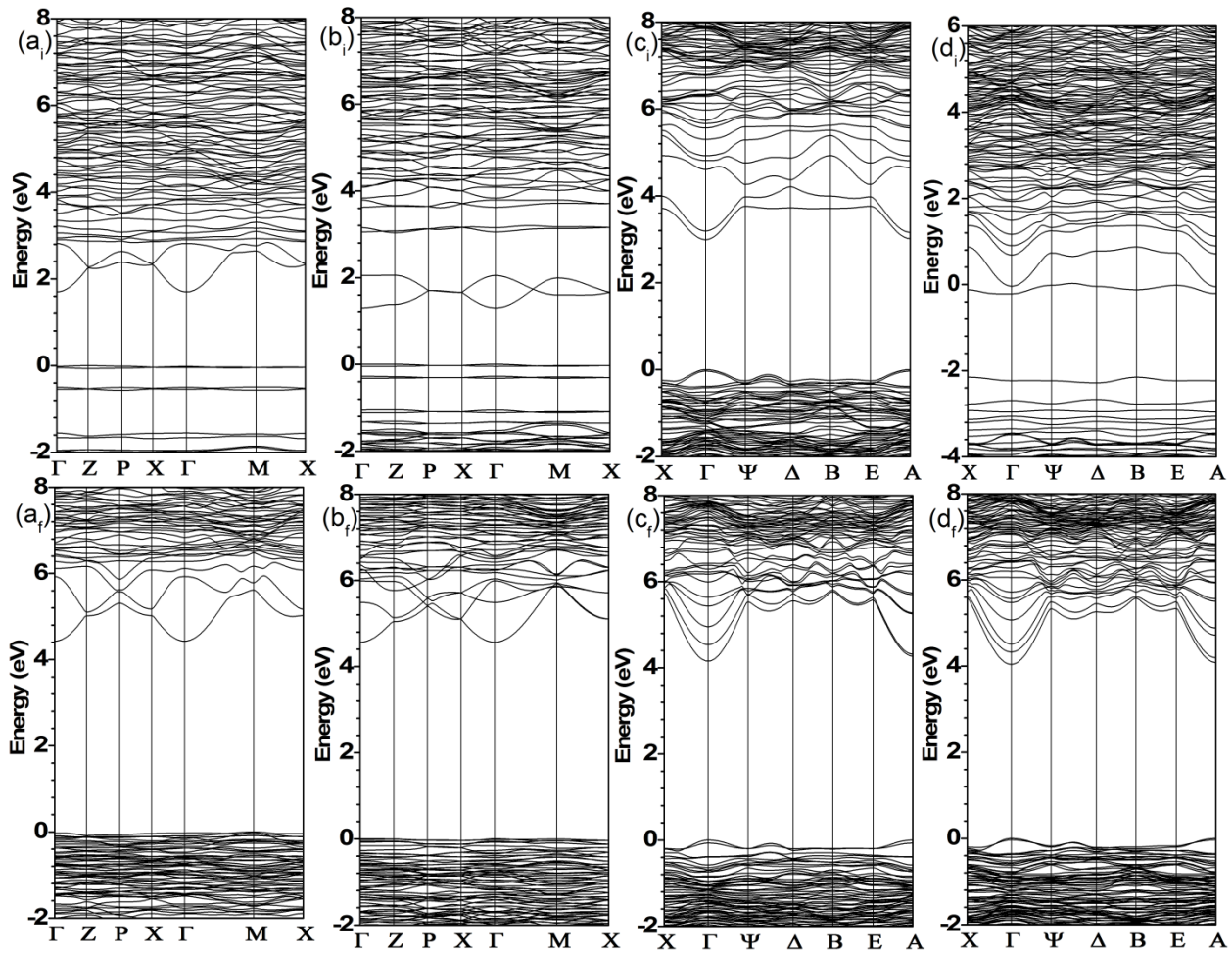


Figure 3. Upper panel: calculated band structure of (ai) jennite, (bi) T9A, (ci) T11A and (di) T14A before geometric optimization. Lower panel: calculated band structure of (af) jennite, (bf) T9A, (cf)T11A and (df) T14A after geometric optimization.

Further analysis of electronic structure calculations show total density of states (TDOS) and element/orbital resolved partial DOS (PDOS). **Figure 4** shows the TDOS and PDOS for Jennite, T9A, T11A and T14A respectively. **Figure 5**, shows orbital-decomposed PDOS of T14A as an example since those for other CSH crystals are quite similar. It further shows that the lower part of the VB is from O-2s and the upper part is from O-2p of the non-water oxygen whereas the lower CB originates from Ca-3d orbitals. There is a significant contribution from Si-3d orbitals on the upper part of the VB. The element resolved PDOS also shows the sp^3 hybridization between Si and the non-water O. The most interesting feature is that the PDOS from water molecules (O plus H) is very different from those of pure water which has distinct sharp peaks⁵³. In CSH, water molecules are in the confined interlayer region and they interact with all other elements within the crystal. The prominent features between -7.6 eV to -6.6 eV are from O-H covalent bonds in water. Furthermore, it was observed the significant role played by the semi-core Ca-3p orbitals at about -18 eV. Its interaction with non-water O contributes to the interlayer Ca-O bond order responsible for interlayer cohesion which will be described later. Such detailed interatomic bonding information has not been discussed in the existing literature.

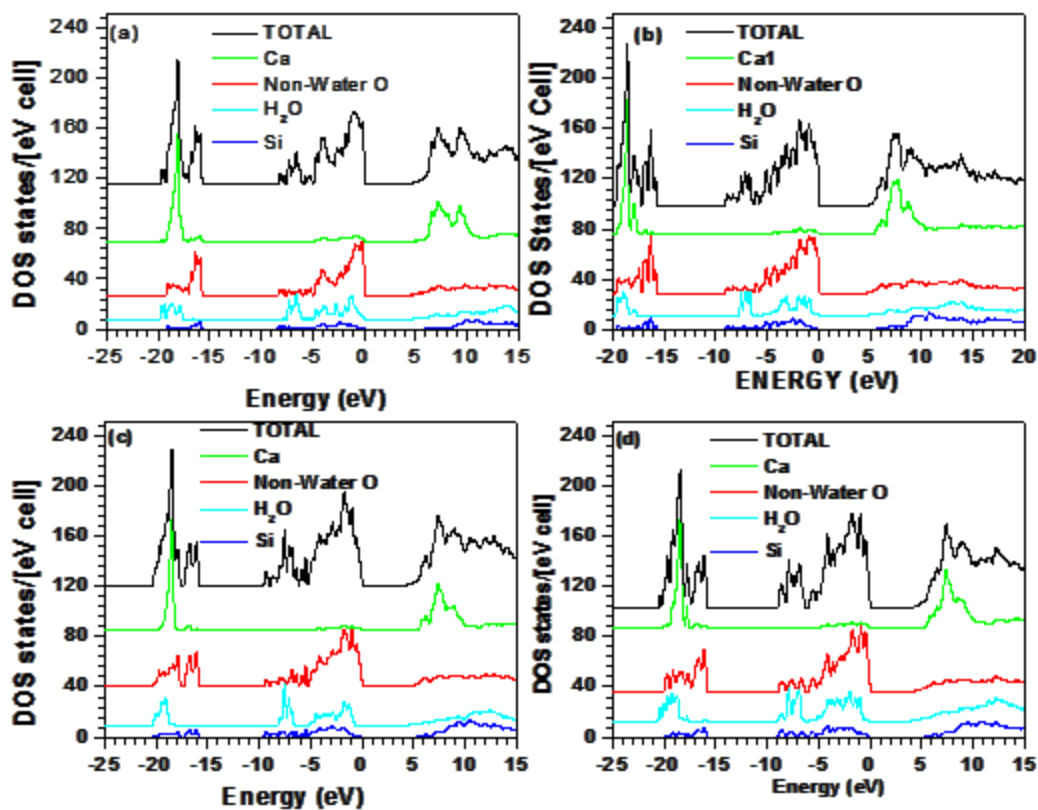


Figure 4. (color online) Total and element resolved partial density of states of (a) jennite, (b) T9A (c) T11A (d) T14A.

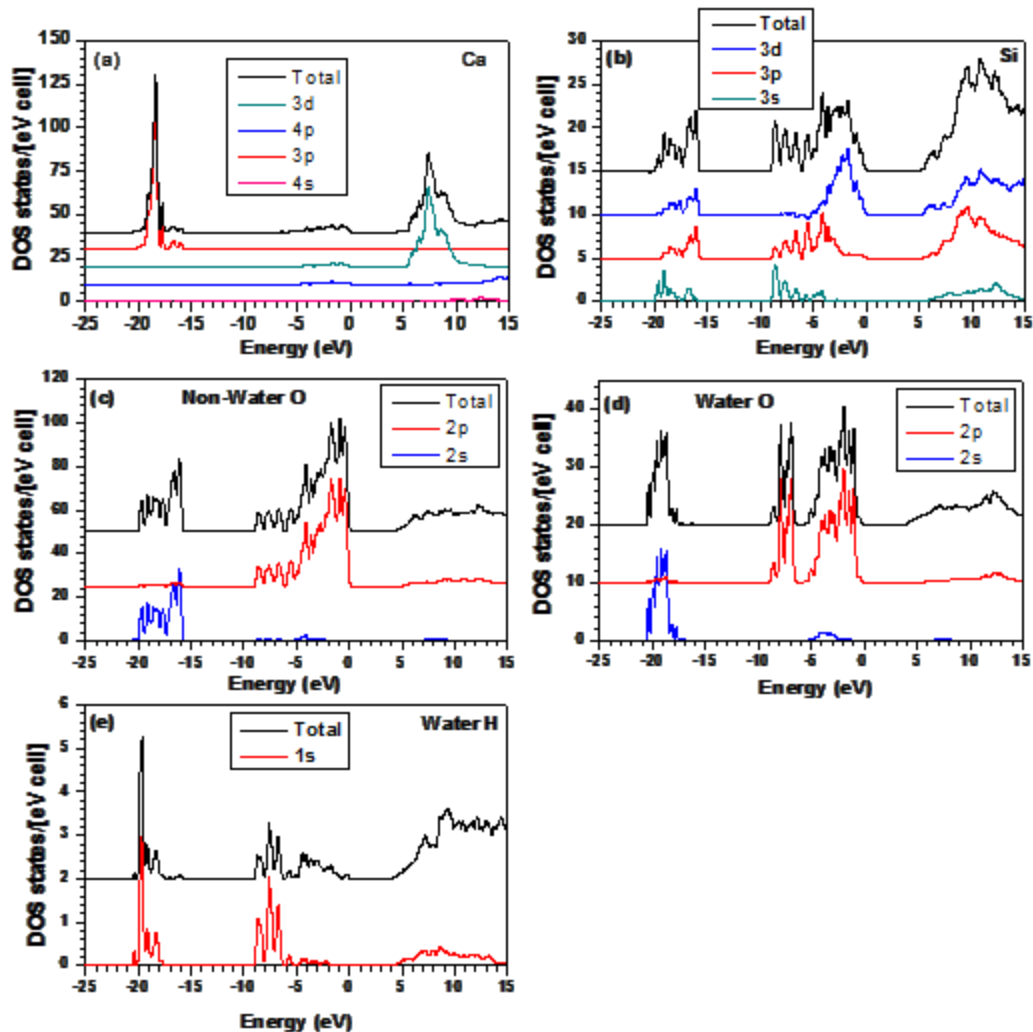


Figure 5. (color online) Total and orbital-resolved partial density of states of T14A: (a) Ca, (b) Si, (c) O (non-water), (d) O (in H₂O), (e) H.

3.3.3 Bond order and hydrogen bonding

The totality of bond orders depends on the number of bonds and the strength of each bond is a compelling indicator of the overall crystal cohesion. **Figure 6** shows the distribution of the calculated BO values of different types of bonds (Si-O, Ca-O (intra layer), Ca-O (inter layer), H-O-H (water), -O-H (hydroxyl ions), H₂O---H, -O---H) in the four CSH crystals where the “---” represents HBs. **Table 2** lists the contributions from each type of bond, their total BO values, the percent BO and the bond order density

(BOD) defined as the total bond order per unit volume. For example, T14A has 13% of its total BO values from intra layer Ca-O bonds, 2.8% from inter layer Ca-O bonds, 49% from Si-O bonds and 35% from all O-H bonds (covalent and HB). Thus, the Si-O bonds are the dominant contributor and the overall stiffness and the anisotropy must be related to the silicate chain orientation in CSH crystal in line with expectations. However T9A and T11A cannot be viewed as typical layered structures because they have bridging silicates connecting the layers. The Si-O bond order for T9A and T11A is very high (> 55%) compared to the other two crystals. It is also interesting to note that overall, the O-H bonds contribute more than the Ca-O bonds. BOD is a quantitative measure of the overall internal cohesiveness of the crystal. T11A has the largest BOD among the four crystals. BOD values of Jennite and T14A and the contributions from each bond type are very close although they have very different crystal structure. These results show that Jennite and T14A have a similar bonding character which alludes to their possibility of coexisting in the larger CSH structure as speculated by previous models ⁴.

Table 2. Summary of bond order for each type of bond (BO%).

| | Jennite | T9A | T11A | T14A |
|----------------------------|---------------|---------------|----------------|----------------|
| Ca-O | 3.825 (22.4%) | 4.305 (19.3%) | 3.603 (15.1%) | 4.407 (16.3%) |
| Si-O | 6.615 (38.7%) | 13.175 (59%) | 13.169 (55.2%) | 13.155 (48.8%) |
| O-H(All bonds) | 6.65 (38.7%) | 4.84 (21.7%) | 7.07 (29.7%) | 9.41 (34.9%) |
| H-O-H | 4.13 (24.2%) | 4.25 (19%) | 5.28 (22.2%) | 7.23 (26.8%) |
| -O-H | 1.63 (9.5%) | 0.00 (0%) | 1.08 (4.5%) | 1.09 (4%) |
| H ₂ O---H | 0.22 (1.3%) | 0.15 (0.7%) | 0.56 (2.4%) | 0.46 (1.7%) |
| -O---H | 0.67 (3.9%) | 0.44 (2%) | 0.15 (0.6%) | 0.63 (2.4%) |
| Total BO | 17.1006 | 22.3312 | 23.8374 | 26.9673 |
| Cell Volume Å ³ | 764.5264 | 948.8569 | 960.2136 | 1191.9475 |
| BOD | 0.0224 | 0.0235 | 0.0248 | 0.0226 |

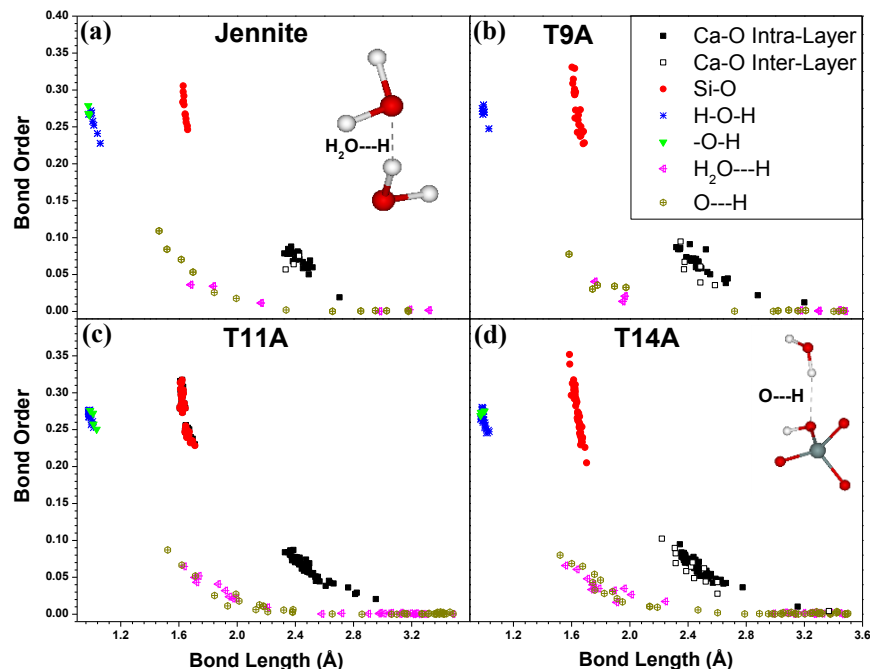


Figure 6. (color online) Distribution of bond order vs. bond length in: (a) jennite, (b) T9A, (c) T11A, and (d) T14A. The color code is Ca-O intra layer (solid black), Ca-O inter layer (open black), Si-O (red), covalent O-H in water (H-O-H) (blue), Non-water -O-H (green), HBs within water (H₂O---H) (pink), and non-water HBs (dark yellow). (color online) The schematic diagrams of the two types of HBs. (a) between H and O in two water molecules; (b) between H in a water molecule and a non-water O.

There are two types of O-H bonds; the strong covalent O-H bonds with a bond length (BL) of about 1 Å and the weaker HBs with BLs larger than ~1.5 Å. The covalent O-H bonds can be sub-divided into two categories; those within the water molecules (H-O-H) and those in the hydroxyl ions (-O-H). Similarly HBs can also be sub-divided into two categories: HB between water molecules (H₂O---H) and HBs between H atoms in water and O atoms connected to Ca and/or Si (-O---H) as illustrated in the inset of **Figure 6**. Both types of the HB contribute to the interlayer cohesion. The HBs have a much broader spread of both BL and BO values, and in some instances can be even stronger than the Ca-O bonds with shorter BLs. The cohesion in CSH crystals in the *c* direction depends on the total bond order in the inter-layer region relative to the intra-layer region. Hence the inter-layer Ca-O bonds (**Table 2**) and HBs control inter-layer

cohesion in the *c* direction. This description holds in general but is particularly true for jennite and T14A, because there are no linkages between the bridging silicates (see **Figure 1**). Conversely T9A and T11A have connected bridging Si tetrahedra which are greatly influenced by the strong covalent Si-O bonds (>55%). T11A has the weakest HBs while jennite and T14A show a substantial increase in HBs, both in BO values and in abundance as shown in **Figure 6**. The BO results clearly indicate the critical role played by HBs in the inter-layer cohesion in the absence of silicate chain connections. The ability to relate the electronic structure results in the form of quantified bond order data to the mechanical properties of the crystal (see the following section) is a significant step forward in the analysis of the mechanical properties of CSH crystals.

3.3.4 Mechanical properties and interlayer cohesion

To further elaborate on the bond order calculations in the four CSH crystals presented above, their elastic coefficients were calculated and are listed in **Table 3**. The elastic constants C_{11} , C_{22} , and C_{33} represent stiffness in *a*, *b*, and *c* crystal axes respectively, are important for understanding the layered structures. The results show that the crystals are generally stiffer in *a* and *b* directions than the *c* (inter-layer) direction. This is caused by the strong covalently bonded silicate chains running along those directions. A closer inspection of **Figure 1** shows some common features between jennite and T14A. In the interlayer region, there is only water and ionic Ca-O bonds and no covalent bonds connecting the layers. Hence the C_{33} is considerably lower than C_{11} and C_{22} . For T9A and T11A, the layers are connected by bridging tetrahedra, consequently resulting in much larger stiffness in *c* direction due to strong

Si-O covalent bonds. Thus, it clearly shows silicate chains are an important factor in the mechanical properties of CSH.

Table 3. Calculated elastic constants for the four CSH crystals in units of GPa.

| C _{ij} | jennite | T9A | T11A | T14A |
|-----------------|---------|--------|--------|--------|
| C ₁₁ | 107.09 | 135.58 | 137.34 | 112.23 |
| C ₂₂ | 122.97 | 152.96 | 145.41 | 125.58 |
| C ₃₃ | 73.45 | 146.89 | 141.17 | 82.83 |
| C ₄₄ | 25.11 | 45.63 | 38.91 | 29.77 |
| C ₅₅ | 23.38 | 22.48 | 28.23 | 25.11 |
| C ₆₆ | 39.45 | 38.90 | 48.99 | 40.51 |
| C ₁₂ | 40.52 | 41.05 | 52.89 | 47.14 |
| C ₁₃ | 37.30 | 28.77 | 36.47 | 24.92 |
| C ₂₃ | 35.39 | 57.18 | 49.66 | 31.09 |

Table 4. Average mechanical properties including comparison with existing work

| GPa | Jennite | | T9A | | T11A | | T14A | |
|-----|---------|---|---------|--|---------|--|---------|---|
| | Present | Others | Present | others | Present | others | Present | others |
| K | 62.65 | 40.2 ^a 31.83 ^b 32.0 ^e | 78.09 | 68.95 ^c 71.42 ^b | 77.19 | 73.57 ^d 66.65 ^b | 56.42 | 44.8 ^a 35.91 ^b 38.6 ^e |
| G | 35.02 | 22.1 ^a 21.96 ^b 19.9 ^e | 43.18 | 37.44 ^c 37.18 ^b | 40.42 | 29.19 ^d 32.03 ^b | 31.65 | 19 ^a 20.61 ^b 22.5 ^e |
| E | 88.56 | 56.06 ^a 53.55 ^b 49.5 ^e | 109.39 | 95.11 ^c 95.06 ^b | 103.25 | 77.34 ^d 82.82 ^b | 80.00 | 49.94 ^a 51.90 ^b 56.5 ^e |
| γ | 0.2752 | 0.31 ^a | 0.27 | 0.27 ^d | 0.28 | 0.32 ^d | 0.26 | 0.31 ^a |

a: ref. ⁵⁴, b: ref. ⁵³, c: ref. ⁵⁵, d: ref. ⁵⁶, e: ref. ⁵⁷

Based on the calculated elastic coefficients, study obtained bulk mechanical properties such as bulk modulus (K), shear modulus (G), and Young's modulus (E), and Poisson's ratio (γ) under the VRH approximation ³⁷ as listed in **Table 4**. Also listed are calculated values for the mechanical properties from some existing work ^{54, 55, 56, 6}. Calculated values in this study are generally higher compared to other calculations,

which can partly be attributed to the refined crystal structure and higher energy cutoff with sufficient k points used in present calculations. Other, secondary, differences are likely hidden in the details of the calculation methods adopted by the various investigators. The method employed in this study has been applied to a wide range of crystalline materials in the past with excellent agreement to the respective experimental data ^{34, 25b, 58}. Due to practical limitations in synthesizing single crystals of complex hydrated crystals, reliable measurements of the elastic constants or the average mechanical properties of CSH crystals are typically unavailable. In a recent publication, the bulk modulus for T14A crystalline powder was reported to be 47 GPa by “Rietveld refinement” using high pressure synchrotron x-ray investigation ⁵⁹. Other experimental studies ^{60, 61} have reported the Young's modulus for portlandite to be 35-49 GPa. However, experimental measurements performed with crystalline powders or hardened CSH paste likely incorporate the effects of crystal defects as well as the presence of larger-scale microstructures, such as porosities, grain boundaries and grain orientations. Therefore, it is not surprising to find that the calculated properties for ideal CSH crystals are generally higher than the experimental values. **Figure 7**, displays data points of BOD, C/S ratios, and the calculated mechanical parameters (K, G and E) for the four CSH crystals. A comparison of the upper and lower frames of **Figure 7** indicates a qualitative correlation between K, G, and E with the BOD but an anti-correlation with the C/S ratio. Therefore, it is possible to conclude that the BOD can serve as a critical electronic-scale measure for classifying broad range of CSH crystals complimenting the C/S ratio and other physical parameters.

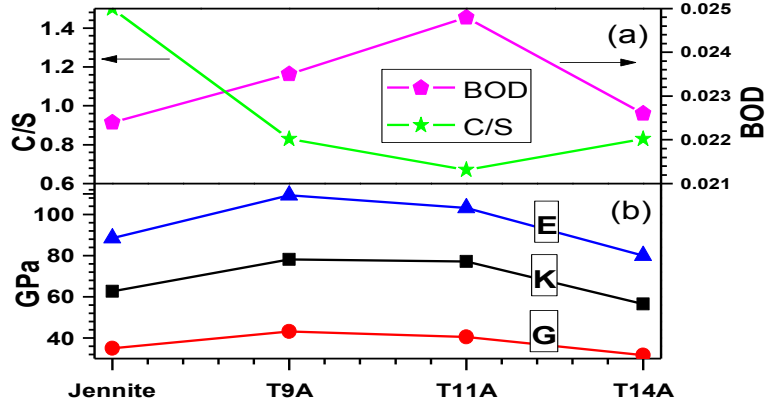


Figure 7. (color online) (a) Plot of the BOD and C/S ratios in the four CSH crystals; (b) Plot of mechanical parameters (K, G, E) in the four crystals.

3.4 Summary and conclusion

In summary, detailed electronic structure calculations using *ab initio* methods clearly show the origins of the mechanical anisotropy and interlayer cohesion in CSH crystals. Calculations in this study show the necessity of refining the crystal structure of these complex hydrated crystals that are not completely accessible experimentally. In the inter-layer region, the strong Si-O bond order is predominant in T9A and T11A compared to jennite and T14A. On the other hand HBs are more significant in jennite and T14A providing the overall stiffness of the material and contributes to the mechanical anisotropy. Thus is correct to conclude that jennite and T14A show similar electronic and mechanical properties and so do T9A and T11A. However their C/S ratios do not follow such a trend. Traditionally, the C/S ratio is the dominant parameter used to characterize CSH materials both experimentally and in modeling studies^{41, 42, 43, 44}. A considerable body of experimental evidences shows that C/S ratios vary with time and are inhomogeneous in the cement sample⁵⁷ and it fails to relate to mechanical properties. Considering the results found in this study and the fact that BOD contains all

the essential physical and chemical information of the crystal, BOD could be considered as an excellent electronic-scale measure for classifying CSH crystals. Thus, this change in paradigm will provide a much more reliable means in identifying the structure; composition and properties of CSH in hardened cement. This fundamental understanding of cements might provide ways to engineer new materials with suitable additives, such as polymers that can alter the interlayer HB's, in constructing more durable cements.

CHAPTER 4

QUANTUM MECHANICAL METRIC FOR INTERNAL COHESION IN CEMENT CRYSTALS

4.1 Introduction

Electronic structure and inter-atomic bonding characteristics are central to the comprehensive understanding of the atomic-scale structure and properties of calcium silicate hydrates (CSH) that are synthesized as Portland cement hydration products. The emerging interest in atomic structure-property relationships is due to the increasingly significant environmental, social and economic impact of the global Portland cement usage and production, which currently stands at 2 billion metric tons. Current experimental findings based upon a variety of spectroscopic and high-resolution microscopic techniques suggest a poorly crystalline or completely disordered atomic structure of these hydrates in hardened cement paste ⁴. Based on these experimental data, a number of structural models have been proposed, either as binary solutions ⁶² or through theoretical modeling using Jennite and Tobermorite type crystals as starting structures ^{4, 41, 45, 63}. These efforts have resulted in a wide range of models for C-S-H ^{8, 13, 15} that are either based on solution theory or limited atomistic simulations using classical molecular dynamics (MD). A key missing ingredient in these efforts is the understanding of bonding characteristics of both the crystalline CSH as well as the more disordered C-S-H. Thus, it is necessary to follow the cement chemistry notation of CSH and CS to represent calcium silicate hydrate and anhydrate crystals, respectively, and

C-S-H to exemplify the more general structure of calcium silicate hydrate found in hardened cement paste.

Crystalline CSH phases range from almost amorphous to highly ordered crystalline phases. Due to their varying degree of crystallinity and the difficulties associated with isolation of pure phases, many uncertainties remain about the composition and structure even for CSH phases of high crystallinity. Moreover, due to the complexity of CSH structures, quantitative bonding information; especially hydrogen bonding (HB), are not accessible purely by experimental means without the aid of robust atomistic model for proper interpretation. In the light of this critical gap in knowledge, it is of paramount importance to investigate a wide variety of crystalline CSH phases with well-documented crystal structures. Such studies will provide an in-depth insight on the variations in bonding characteristics in relation to the composition and structures of these materials. Without this information, the atomistic models of C-S-H proposed ⁶⁴ in the literature remain speculative.

The uncertainty with respect to position of “H” was discussed previously in a study of four crystalline CSH crystals (See chapter 3). Since HB has a significant presence in CSH, it plays a crucial role in the behavior of these materials. This fact has been generally recognized but rarely studied quantitatively. Clearly, even for crystalline phases, the bonding information cannot be determined purely from experimental data in the absence of refined structures of these phases. Thus this study intends to use materials genomic approach and theoretically investigate a broad range of CSH crystals using accurate first principles methods. Out of the 30 crystalline phases listed by Richardson 2008 review ⁴, this study focus on 15 CSH crystals with well-documented

structural information, four anhydrous precursors, and portlandite. The procedure begins with fully optimized atomic structures of these crystalline phases (see section 2.3.1). So called supercell approach was used to address the issue of partial occupancy at certain sites in some crystals. The electronic structures of the refined structures were then calculated. Subsequently, quantitative evaluation was done on bonding characteristics of these crystals through bond order (overlap population) calculations. Results were analyzed following the modified Strunz classification of minerals⁶⁵ according to the degree of polymerization of the silicate chains in these crystals. The data obtained from crystalline phases helps in interpreting experimental spectroscopic measurements leading to realistic models that are consistent with both electronic-scale and atomistic-scale behaviors for the C-S-H phase in hardened Portland cement.

4.2 Computational modeling details

The technical details of VASP relaxations (see section 2.3.1) for all crystal structures in this work are briefly outlined as follows: (1) the PAW-PBE potentials^{30, 50} is used with the generalized gradient approximation (GGA). (2) The electronic convergence criterion set at 10^{-6} eV. (3) The force convergence criterion set at 10^{-5} eV/Å for ionic relaxation. (4) A high energy cutoff of 500 eV was adopted and (5) A sufficiently large number of *k*-point-meshes ranging from 2 to 85 k-points were used depending on the actual crystal structure and size. The electronic structure and bond order (BO) and total bond order density (TBOD) calculations were carried out using the OLCAO method as discussed in section 2.2. The parameters were close to what was used in chapter 3 but varies because of the number of different crystals used here.

4.3 Classifications and structural details of CSH crystals

A comprehensive review by Richardson *et. al.*⁴ includes an extensive list of 30 CSH crystal phases that are categorized into six groups following Taylor *et al.*^{63a}. However, the CSH crystals can be more appropriately classified according to the Strunz classification⁶⁵ by considering the silicate chain polymerization. The notion of silicate chain polymerization also has implications on the products of the complex hydration process^{66, 67} and carbonation or biological degradation^{68, 69} that occurs in Portland cement paste. It has been speculated that the maturation of cement paste involves increasing polymerization of primarily isolated Si tetrahedra to dimers, trimmers and pentamers, eventually forming a 3-dimensional silicate framework⁷⁰.

Table 5 lists 20 crystal phases with well-documented atomic positions used in this study placed into four groups: **a**, Clinker and hydroxide phase; **b**, nesosubsilicates; **c**, sorosilicates; and **d**, ionosilicates. Each group in **Table 5** is arranged in ascending order of calcium to silicon (C/S) ratio. The clinker phases (a.1 and a.2) and the Portlandite (a.3) are placed in **group a**. Portlandite is included in this group since it forms the basis for hydration of cement. The remaining crystals are grouped according to the Strunz scheme. In this scheme, the silicate units at each polymerization step are indicated by Q^n , where the Si tetrahedron is connected to n other silicate tetrahedral via n bridging oxygen. For example, an isolated silicate tetrahedron not connected to any other is denoted by Q^0 . The nesosubsilicates with isolated $[SiO_4]^{-4}$ groups are placed in **group b**. These CSH phases possess the lowest degree of polymerization. The sorosilicates with $[Si_2O_7]^{-6}$ groups in the next polymerization step are placed under **group c**. For these phases, the $[Si_2O_7]^{-6}$ is connected to two isolated tetrahedra via one

bridging-O to form the so-called pyrogroups. Thus, all silicon tetrahedra are Q^1 . These silicon tetrahedra are linked via non-bridging O, to six-, seven- or even eight fold-coordinated Ca atoms. A special case of sorosilicate structures are those with mixtures of isolated tetrahedra (Q^0) and finite triple chains (Q^2), in which the silicon tetrahedra are connected to 6 and 8-fold coordinated Ca atoms. The **group d** contains the inosilicates. These comprise structures with infinitely long chains with a wide variety of C/S ratios, ranging from 0.50 in Nekoite (d.1) to 1.5 in Jennite (d.8). According to the degree of polymerization, the phases in this group could be subdivided into inosilicates with single chains (all tetrahedra are Q^2), and double chains ($2/3 Q^2$ and $1/3 Q^3$). Ball and stick diagrams of all 20 crystals are displayed in the **Figure 8**. Groups are not separated to save space but show the designated group number and the mineral name instead.

Some of the crystals listed in **Table 5** were not accurate enough as originally reported in the literature. For example, Alite crystal structure reported by De la Torre et. al.⁷¹ was not accurate. The positions for atom Ca_{28} and Ca_{29} were assigned the same coordinate and an O position was missing from the Si_2 tetrahedral unit, which is needed to recover the chemical formula. Thus, appropriate changes were made accordingly and the fully relaxed structure was used in the present study.

The Killalite (c.4) is a complex crystal with partial occupancy⁷². It is non-stoichiometric with a composition that is intermediate between the theoretical end members $Ca_6[Si_2O_6(OH)]_2(OH)_2$ and $Ca_7[Si_2O_7]_2(OH)_2$. The Ca_5 , H_2 (H_9) have occupancies that are 0.32, 0.68 respectively⁷². A 3x1x1 supercell was used to address this issue by removing partially occupied atoms from the supercell appropriately to get

the correct stoichiometry and full occupation of atomic sites in the supercell. Fully relaxed crystal structures for Alite and Killalite are available on request.

Table 5. Mineral names, crystal symmetry and space group symmetry, chemical formulas, Calculated C/S, density, and band gap (in eV) of the 20 crystals in this study.

| | Mineral Name | sy:sg | Chemical formula | Ca/Si | ρ (g/cc) | E_g |
|-------------------------------|----------------|--------------------------|--|-------|------------------|-------|
| (a). Clinker/Hydroxide phases | | | | | | |
| a.1 | Belite | O: $P 1 21/n 1$ | $2(\text{CaO}) \text{SiO}_2$ | 2.00 | 3.316 | 4.65 |
| a.2 | Alite | M: P-1 | $3(\text{CaO}) \text{SiO}_2$ | 3.00 | 3.084 | 3.68 |
| a.3 | Portlandite | M: $P -3 m 1$ | $\text{Ca}(\text{OH})_2$ | Inf | 2.668 | 3.50 |
| (b). Nesosubsilicates | | | | | | |
| b.1 | Afwillite | M: P1 | $\text{Ca}_3(\text{SiO}_3\text{OH})_2 \cdot 2\text{H}_2\text{O}$ | 1.50 | 2.590 | 4.26 |
| b.2 | α -C2SH | O: $P 2_1/b 2_1/c 2_1/a$ | $\text{Ca}_2(\text{HSiO}_4)(\text{OH})$ | 2.00 | 2.693 | 4.37 |
| b.3 | Dellaite | Tc: P-1 | $\text{Ca}_6(\text{Si}_2\text{O}_7)(\text{SiO}_4)(\text{OH})_2$ | 2.00 | 2.929 | 4.12 |
| b.4 | Ca Chondrodite | M: $P 1 1 2_1/b$ | $\text{Ca}_5[\text{SiO}_4]_2(\text{OH})_2$ | 2.50 | 2.828 | 4.24 |
| (c). Sorosilicates | | | | | | |
| c.1 | Rosenhahnite | Tc: P-1 | $\text{Ca}_3\text{Si}_3\text{O}_8(\text{OH})_2$ | 1.00 | 2.874 | 4.49 |
| c.2 | Suolunite | O: $F d 2 d$ | $\text{Ca}_2[\text{Si}_2\text{O}_5(\text{OH})_2]\text{H}_2\text{O}$ | 1.00 | 2.649 | 4.87 |
| c.3 | Kilchoanite | O: $I 2 c m$ | $\text{Ca}_6(\text{SiO}_4)(\text{Si}_3\text{O}_{10})$ | 1.50 | 2.937 | 4.40 |
| c.4 | Killalaite | M: $P 1 2_1/m 1$ | $\text{Ca}_{6.4}(\text{H}_{0.6}\text{Si}_2\text{O}_7)_2(\text{OH})_2$ | 1.60 | 2.838 | 3.85 |
| c.5 | Jaffeite | Tg: $P 3$ | $\text{Ca}_6[\text{Si}_2\text{O}_7](\text{OH})_6$ | 3.00 | 2.595 | 3.92 |
| (d). Inosilicates | | | | | | |
| d.1 | Nekoite | Tc: P1 | $\text{Ca}_3\text{Si}_6\text{O}_{15} \cdot 7\text{H}_2\text{O}$ | 0.50 | 2.204 | 4.29 |
| d.2 | T11 Å | M: $B 1 1 m$ | $\text{Ca}_4\text{Si}_6\text{O}_{15}(\text{OH})_2 \cdot 5\text{H}_2\text{O}$ | 0.67 | 2.396 | 4.15 |
| d.3 | T14 Å | M: $B 1 1 b$ | $\text{Ca}_5\text{Si}_6\text{O}_{16}(\text{OH})_2 \cdot 7\text{H}_2\text{O}$ | 0.83 | 2.187 | 4.04 |
| d.4 | T 9 Å | Tc: C1 | $\text{Ca}_5\text{Si}_6\text{O}_{17} \cdot 5\text{H}_2\text{O}$ | 0.83 | 2.579 | 4.57 |
| d.5 | Wollastonite | Tc: P-1 | $\text{Ca}_3\text{Si}_3\text{O}_9$ | 1.00 | 2.899 | 4.62 |
| d.6 | Xonotlite | Tc: A-1 | $\text{Ca}_6\text{Si}_6\text{O}_{17}(\text{OH})_2$ | 1.00 | 2.655 | 4.27 |
| d.7 | Foshagite | Tc: P-1 | $\text{Ca}_4(\text{Si}_3\text{O}_9)(\text{OH})_2$ | 1.33 | 2.713 | 4.41 |
| d.8 | Jennite | Tc: P-1 | $\text{Ca}_9\text{Si}_6\text{O}_{18}(\text{OH})_6 \cdot 8\text{H}_2\text{O}$ | 1.50 | 2.310 | 4.43 |

Sy = crystal symmetry

Sg = space group symmetry

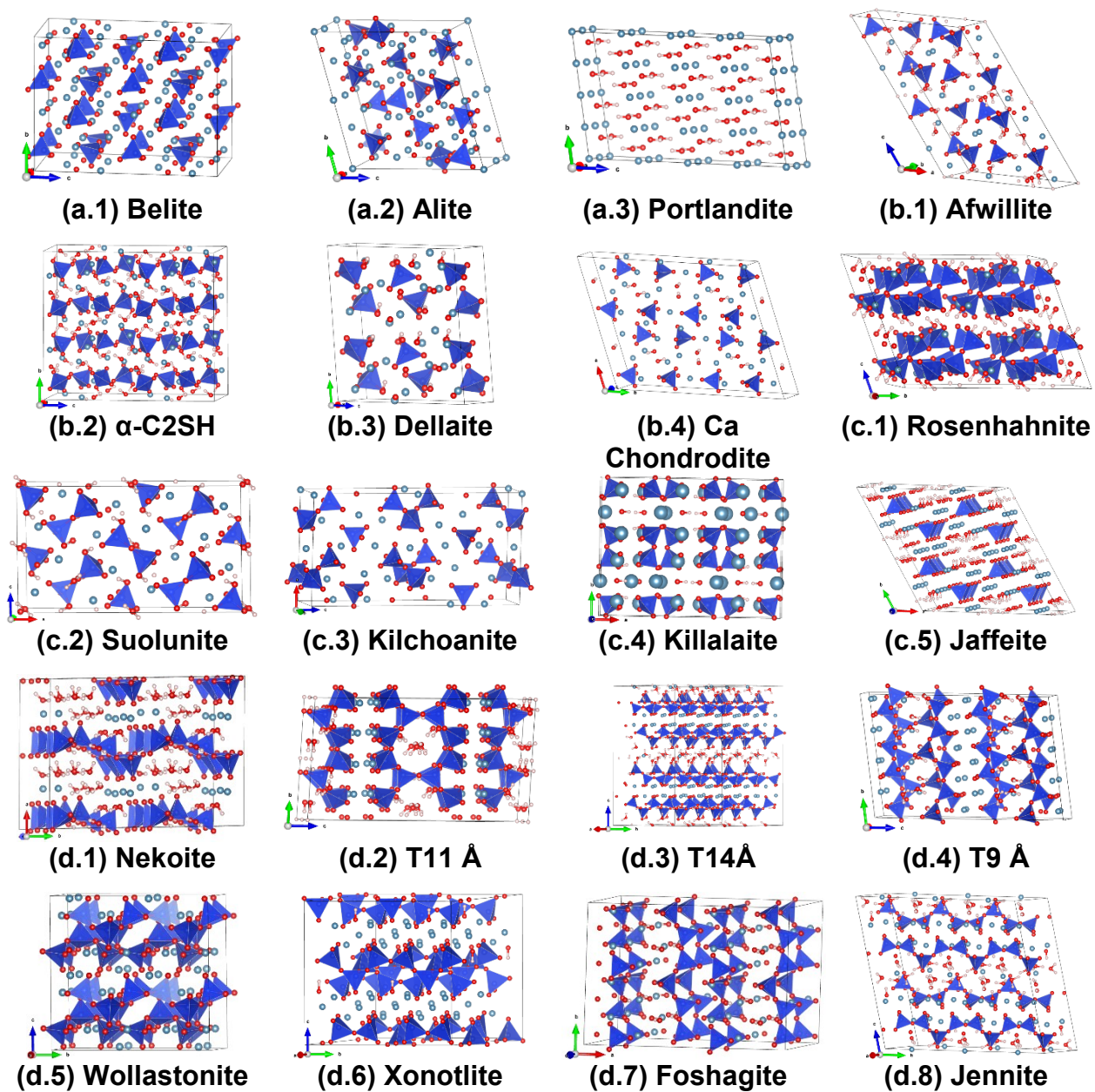


Figure 8 Ball and Stick diagrams of 20 CSH and CS crystal structures.

Table 6 provides experimental crystal structure parameters a , b , c and α , β , γ directly as reported in the references for the interested reader. Almost all structures were found in Richardson *et al.* ⁴ and Manzano's thesis ⁶, and references therein.

Table 6. Experimental crystal parameters of the 20 crystals.

| | a(Å) | b(Å) | c(Å) | α° | β° | γ° |
|-----|--------|--------|--------|----------------|---------------|----------------|
| a.1 | 5.504 | 6.762 | 9.328 | 90.00 | 94.17 | 90.00 |
| a.2 | 11.639 | 14.172 | 13.643 | 104.98 | 94.62 | 90.11 |
| a.3 | 3.593 | 3.593 | 4.905 | 90.00 | 90.00 | 120.00 |
| b.1 | 16.330 | 5.639 | 11.685 | 90.08 | 126.45 | 89.95 |
| b.2 | 9.487 | 9.179 | 10.666 | 90.00 | 90.00 | 90.00 |
| b.3 | 6.850 | 6.950 | 12.900 | 90.75 | 97.33 | 98.25 |
| b.4 | 8.921 | 11.448 | 5.076 | 90.00 | 90.00 | 108.32 |
| c.1 | 6.955 | 9.484 | 6.812 | 108.64 | 94.84 | 95.89 |
| c.2 | 19.776 | 5.990 | 11.119 | 90.00 | 90.00 | 90.00 |
| c.3 | 11.420 | 5.090 | 21.950 | 90.00 | 90.00 | 90.00 |
| c.4 | 20.472 | 15.465 | 6.839 | 90.00 | 97.69 | 90.00 |
| c.5 | 10.035 | 10.035 | 7.499 | 90.00 | 90.00 | 120.00 |
| d.1 | 7.588 | 9.793 | 7.339 | 111.77 | 103.50 | 86.53 |
| d.2 | 6.735 | 7.385 | 22.487 | 90.00 | 90.00 | 123.25 |
| d.3 | 6.735 | 7.425 | 27.987 | 90.00 | 90.00 | 123.25 |
| d.4 | 11.274 | 7.344 | 11.468 | 99.18 | 97.19 | 90.03 |
| d.5 | 7.940 | 7.320 | 7.070 | 90.03 | 95.37 | 103.43 |
| d.6 | 8.712 | 7.363 | 14.023 | 89.99 | 90.36 | 102.18 |
| d.7 | 10.320 | 7.360 | 7.040 | 90.00 | 106.40 | 90.00 |
| d.8 | 10.576 | 7.265 | 10.931 | 101.30 | 96.98 | 109.65 |

4.4 Electronic band structures of CSH

Although the atomic structures of the crystals in **Table 5** are generally available⁷¹, inaccuracies exists along with some missing data. Section 4.3 gives additional information on the fully relaxed and corrected structures to reconcile with the chemical formula where applicable. **Table 5** gives summary of the crystal symmetry, chemical formulas, theoretical density, C/S ratio and calculated electronic band gap. Out of the 20 crystals studied, 4 are anhydrate phases; 2 contain purely isolated water molecules, 5 include both isolated water and hydroxyl groups, and rest has only hydroxyl groups. In CSH, hydroxyl groups are mostly connected to Si (Si-OH) but in some instances (b.1, b.2, b.3, c.2, c.4, c.5, d.6 and d.7) they are connected to Ca (Ca-OH) as well. The calculated band structures for the 20 crystals are displayed in **Figure 9**. The zero

energy was set at the highest occupied state, or the top of the valence band (VB). As expected, all crystals have large band gaps ranging from 3.50 eV to 4.87 eV and exhibit flat top of VB except a.3. The bottom of the conduction bands (CB) of all crystals have large curvatures suggesting small electron effective mass. Analysis of the partial density of states (PDOS) indicates that the lower part of the VB is from O-2s orbitals and the upper part is from O-2p orbitals of the non-water O whereas the lower CB originates mostly from Ca-3d orbitals. There is a significant contribution from Si-3d orbitals to the upper part of the VB as well. High quality band structure based on accurately relaxed structure is important in assessing the electronic structure because experimentally measured structures are usually not sufficiently accurate. This is particularly true for hydrated crystals with water molecules. Discrepancy with the experimentally assigned “H” positions was pointed out in earlier work ⁷³. **Table 7** shows the VASP relaxed crystal parameters and the percent deviation from the experimentally reported values. The experimental crystal parameters are given in the **Table 6**. The relaxed crystal parameters in general vary 1-2% compared to the reported experimental values but in some cases such as b.1 and b.4, they can be as high as -4.1%. The highest deviation is in the angle γ of the awfillite (b.1) crystal structure. This is a highly hydrated phase and with considerable deviation in the hydrogen positions from the reported structure. These deviations are larger than those usually found in other inorganic crystals. Obviously, there are large uncertainties in the data reported by different groups using different methods measured at different times for some of these CSH crystals. Hence, accurate theoretical computations based on DFT can provide the much needed consistency for CSH crystal structures, based upon which reliable properties can be evaluated.

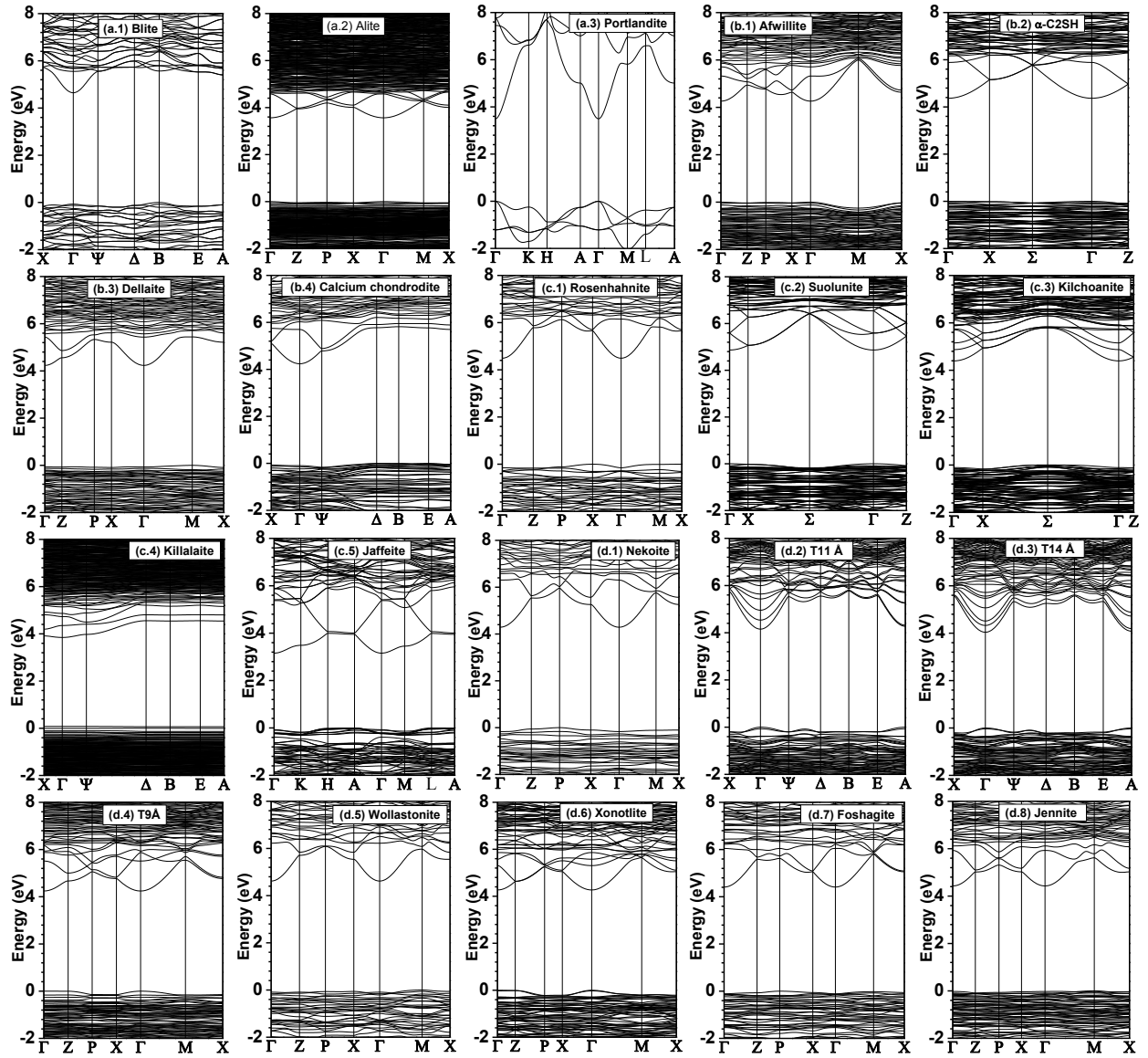


Figure 9. Band Structures of 20 CSH and CS crystal structures.

Table 7. The crystal parameters (% error from experimentally reported values).

| | a(Å) | b(Å) | c(Å) | α° | β° | γ° |
|-----|--------------|--------------|--------------|----------------|---------------|----------------|
| a.1 | 5.565(-1.1) | 6.8(-0.6) | 9.363(-0.4) | 90(0) | 94.70(-0.6) | 90(0) |
| a.2 | 11.733(-0.8) | 14.298(-0.9) | 13.743(-0.7) | 104.80(0.2) | 94.36(0.3) | 90.11(0) |
| a.3 | 3.614(-0.6) | 3.614(-0.6) | 4.958(-1.1) | 90.18(-0.2) | 89.82(0.2) | 120.025(0) |
| b.1 | 16.57(-1.5) | 5.719(-1.4) | 11.764(-0.7) | 87.59(2.8) | 127.06(-0.5) | 93.65(-4.1) |
| b.2 | 9.535(-0.5) | 9.228(-0.5) | 10.777(-1) | 90(0) | 90(0) | 90(0) |
| b.3 | 6.888(-0.5) | 7.028(-1.1) | 12.952(-0.4) | 90.10(0.7) | 97.29(0) | 98.28(0) |
| b.4 | 8.956(-0.4) | 11.556(-0.9) | 5.111(-0.7) | 90.56 (-0.6) | 89.28(0.8) | 108.71(-0.4) |
| c.1 | 7.052(-1.4) | 9.548(-0.7) | 6.883(-1) | 108.78 (-0.1) | 95.73(-0.9) | 95.34(0.6) |
| c.2 | 19.988(-1.1) | 6.036(-0.8) | 11.239(-1.1) | 90(0) | 90(0) | 90(0) |
| c.3 | 11.527(-0.9) | 5.13(-0.8) | 22.204(-1.2) | 90(0) | 90(0) | 90(0) |
| c.4 | 20.638(-0.8) | 15.607(-0.9) | 6.898(-0.9) | 90(0) | 97.17(0.5) | 89.87(0.1) |
| c.5 | 10.085(-0.5) | 10.084(-0.5) | 7.538(-0.5) | 90 (0) | 90(0) | 120(0) |
| d.1 | 7.665(-1) | 9.797(0) | 7.418(-1.1) | 110.94(0.7) | 103.59(-0.1) | 86.69(-0.2) |
| d.2 | 6.736(0) | 7.451(-0.9) | 22.73(-1.1) | 89.63(0.4) | 90.42(-0.5) | 122.22(0.8) |
| d.3 | 6.706(0.4) | 7.416(0.1) | 28.589(-2.1) | 90.70(-0.8) | 92.45(-2.7) | 122.65(0.5) |
| d.4 | 11.414(-1.2) | 7.416(-1) | 11.48(-0.1) | 98.36(0.8) | 97.05(0.1) | 90.23(-0.2) |
| d.5 | 8.009(-0.9) | 7.381(-0.8) | 7.139(-1) | 90.08(-0.1) | 95.53(-0.2) | 103.44(0) |
| d.6 | 8.786(-0.8) | 7.422(-0.8) | 14.193(-1.2) | 89.95(0) | 90.66(-0.3) | 102.25(-0.1) |
| d.7 | 10.423(-1) | 7.367(-0.1) | 7.159(-1.7) | 90.07(-0.1) | 106.48(-0.1) | 89.98(0) |
| d.8 | 10.732(-1.5) | 7.349(-1.2) | 10.784(1.3) | 103.22(-1.9) | 94.78(2.3) | 110.24(-0.5) |

4.5 Main types of bonds in CSH

The bond order (BO) between each pair of atoms represents the quantitative measure of the bond stiffness and strength ⁷⁴. They are important in revealing the origin of internal cohesion in the CSH crystals. Thus BO values were obtained between every pair of atoms in the crystal using the first-principles orthogonalized linear combination of atomic orbitals (OLCAO) method ^{25a}. **Figure 10** shows the BO vs bond length (BL) distributions for four representative CSH crystals from each group (a: alite, b: afwillite, c: suolunite, and d: jennite). Different bond types in each crystals (Ca-O, Si-O, H-O-H, -(O-H), H₂O...H₂O and -(O...H)) are as indicated in **Figure 10**. As evident, there are two types of OH bonds. The strong covalently bonded ones and the weaker HBs. Further, there are two types of covalent O-H bonds: those within the water molecules (H-O-H) which do not contribute to internal cohesion, and those in the hydroxyl ions -(O-H),

which attach to silicates (Si-OH) or Ca ions (Ca-OH). The HBs also have two categories: HBs between water molecules ($\text{H}_2\text{O}\cdots\text{H}_2\text{O}$, shown as inset of **Figure 10** for b.1), and all other types of HBs that are not exclusively between two isolated water molecules. For example, the HBs, such as $\text{Si}-(\text{O}\cdots\text{H})\text{O}-\text{Si}$ and $\text{H}_2(\text{O}\cdots\text{H})\text{O}-\text{Si}$, that are particularly significant are shown as inset of **Figure 10** for c.2 and d.8, respectively. As an overall measure of the crystal cohesion, the total BO (TBO) can be defined (see section 2.2).

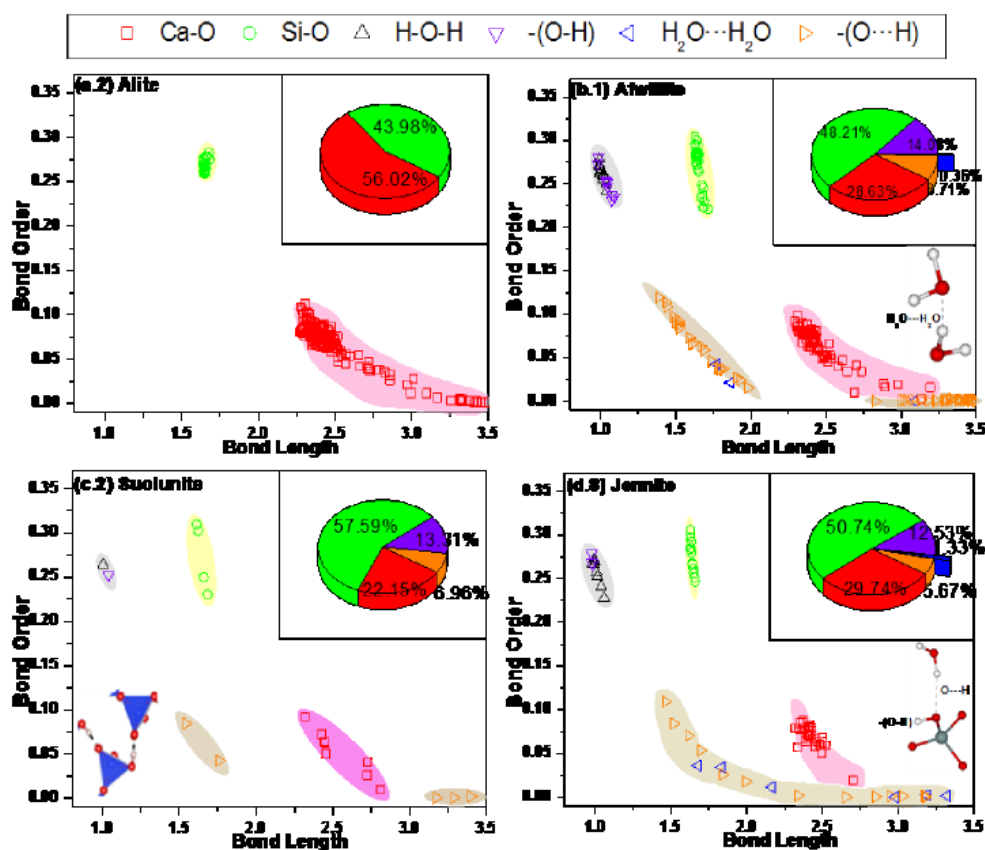


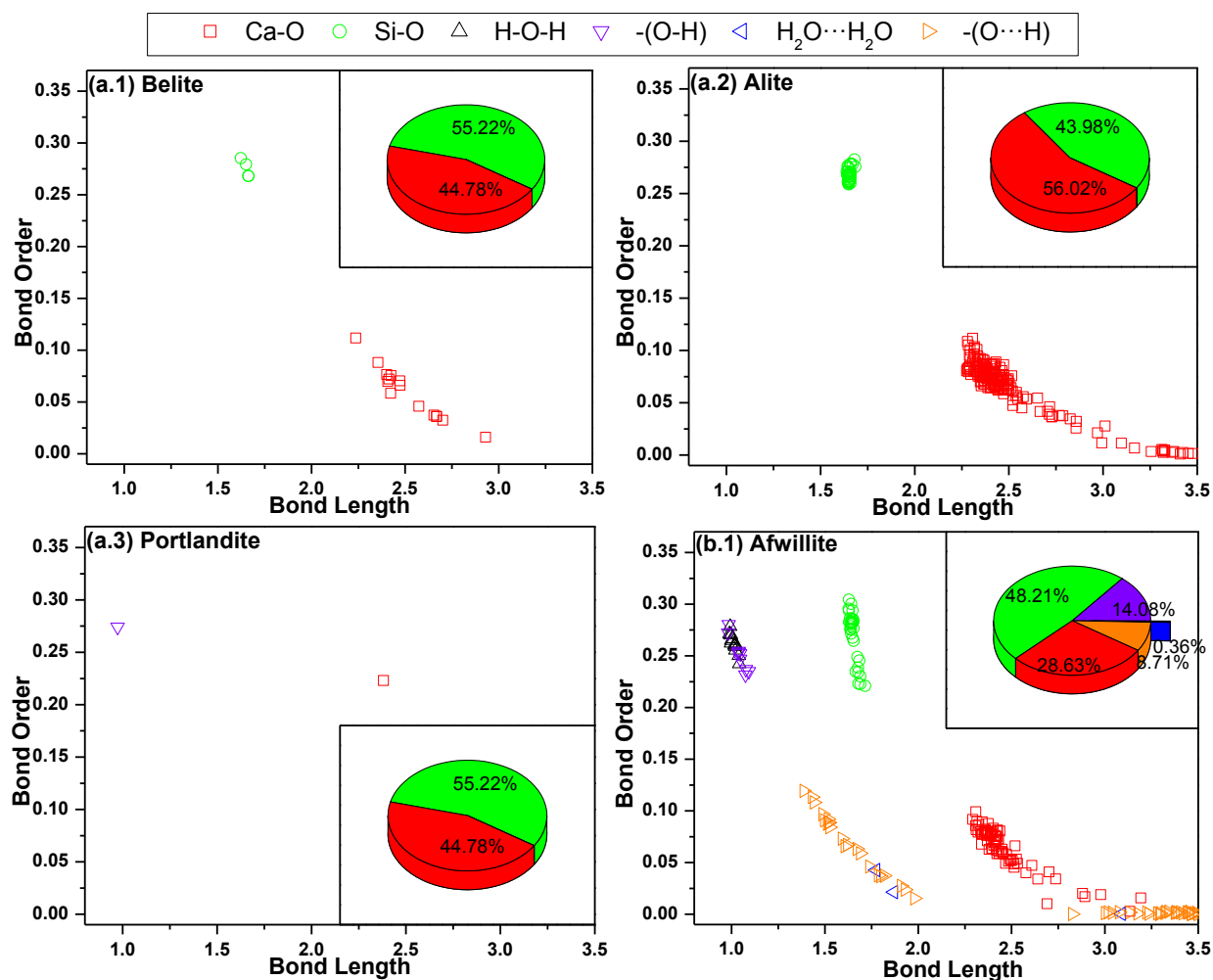
Figure 10. Distribution of bond order vs. bond length in four representative crystals. (a.2) Allite; (b.1) Alwillite; (c.2) Suolunite; and (d.8) Jennite. Symbols for different types of bonds are shown at the top, “-” for covalent bond, “...” for hydrogen bond. The pie chart in the inset shows the percentage of different types of bonding: red, Ca-O; green, Si-O; violet covalent $-(\text{O}-\text{H})$; orange, other HB; blue, HB between H_2O . Lower insets show different types of hydrogen bonds.

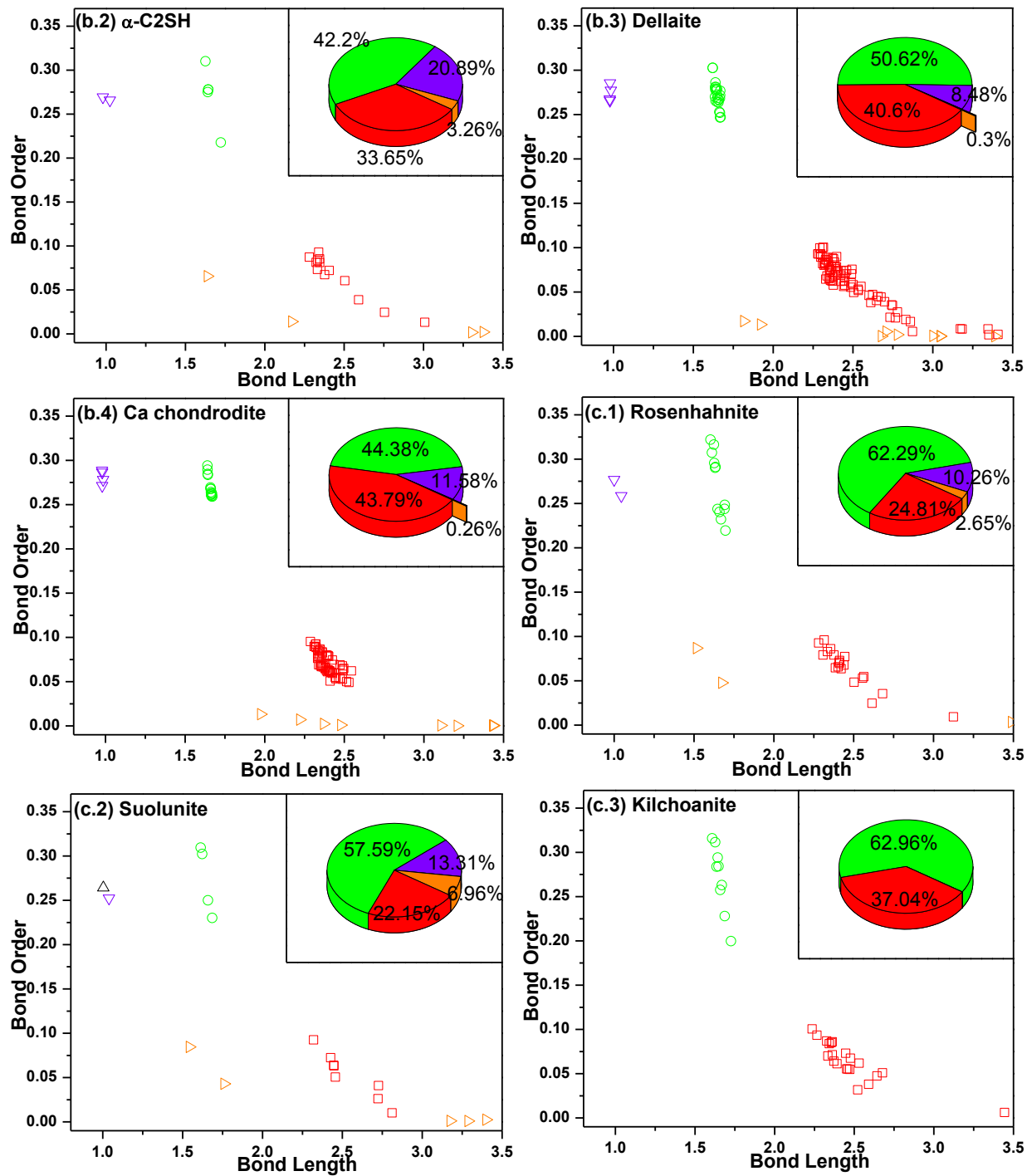
The pie charts in **Figure 10** give the percentage contribution from different types of bonds to the TBO (Note: BO contribution from covalent O-H bonds from water molecule was ignored in calculating the percentage contributions since they do not directly contribute to the overall cohesion). **Figure 10** gives an overall representative picture of the distribution and relative strengths of different bond species in CSH crystals. The broad, almost continuous distribution of Si-O BO values within a fairly narrow range of Si-O BL clearly indicates that the bond stiffness/strength, not the bond length is primary reason as to why the spectral features associated with Si-O bond often appear as broad peaks [30]. It is also remarkable to note that HBs cover a wide range of BO and BL in these materials and have a significant contribution to the TBO. The effects of HBs were widely speculated in experimental spectroscopic techniques but never clearly explained. The following section describes the BO distributions for crystals in each group in relation to their structural characterization, showing the complex picture of different BO contributions to the crystal cohesion.

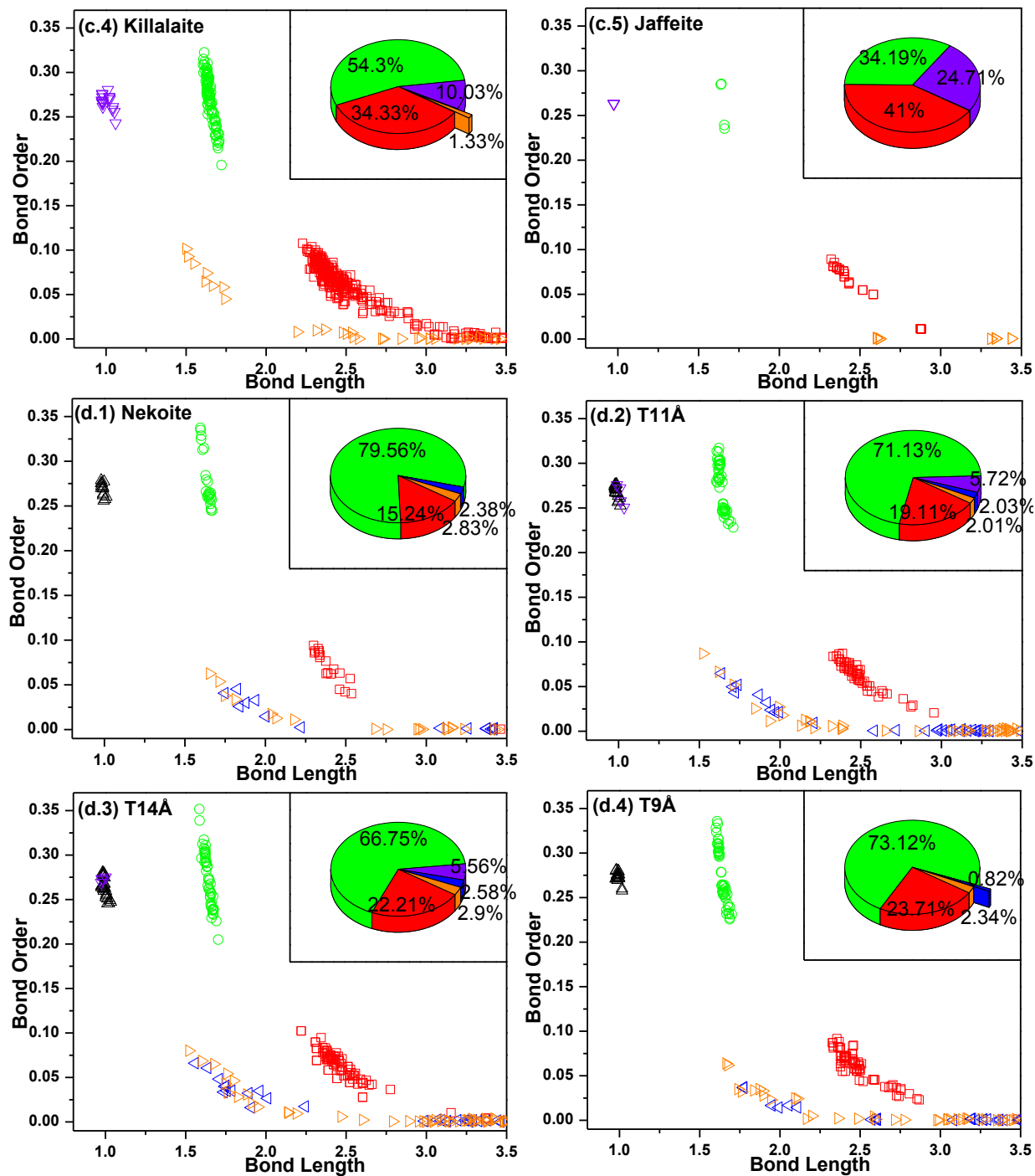
4.6 Bond order distribution for each group

Figure 11 displays the plots of BO versus BL and the percentage contribution from different types of bonds to the TBO for all 20 crystals. In **group a**, Belite (a.1) and Alite (a.2), contain only Q^0 silicates. The Si-O bonds have a narrow BO distribution centered at ~ 0.27 with BL centered at ~ 1.65 Å. The much weaker Ca-O bonds exhibit a larger BO and BL dispersion ranging from 0.02 to 0.10 and 2.25 Å to 3.50 Å, respectively. The Ca-O bonds in Belite have almost evenly spread BO and BL, while those in Alite show some clustering between 2.27 Å to 2.55 Å. These BO and BL

distributions clearly explain why strong and considerably sharper Si-O peaks dominate experimental vibrational spectroscopic analyses of these minerals in contrast to the broad and weaker peaks associated with Ca-O bonds ⁷⁵. It is noteworthy that in Portlandite (a.3) the BO for Ca-O bonds (0.223 with a BL of 2.381 Å) is much stronger than the Ca-O bonds in the above CS crystals and all other CSH crystals.







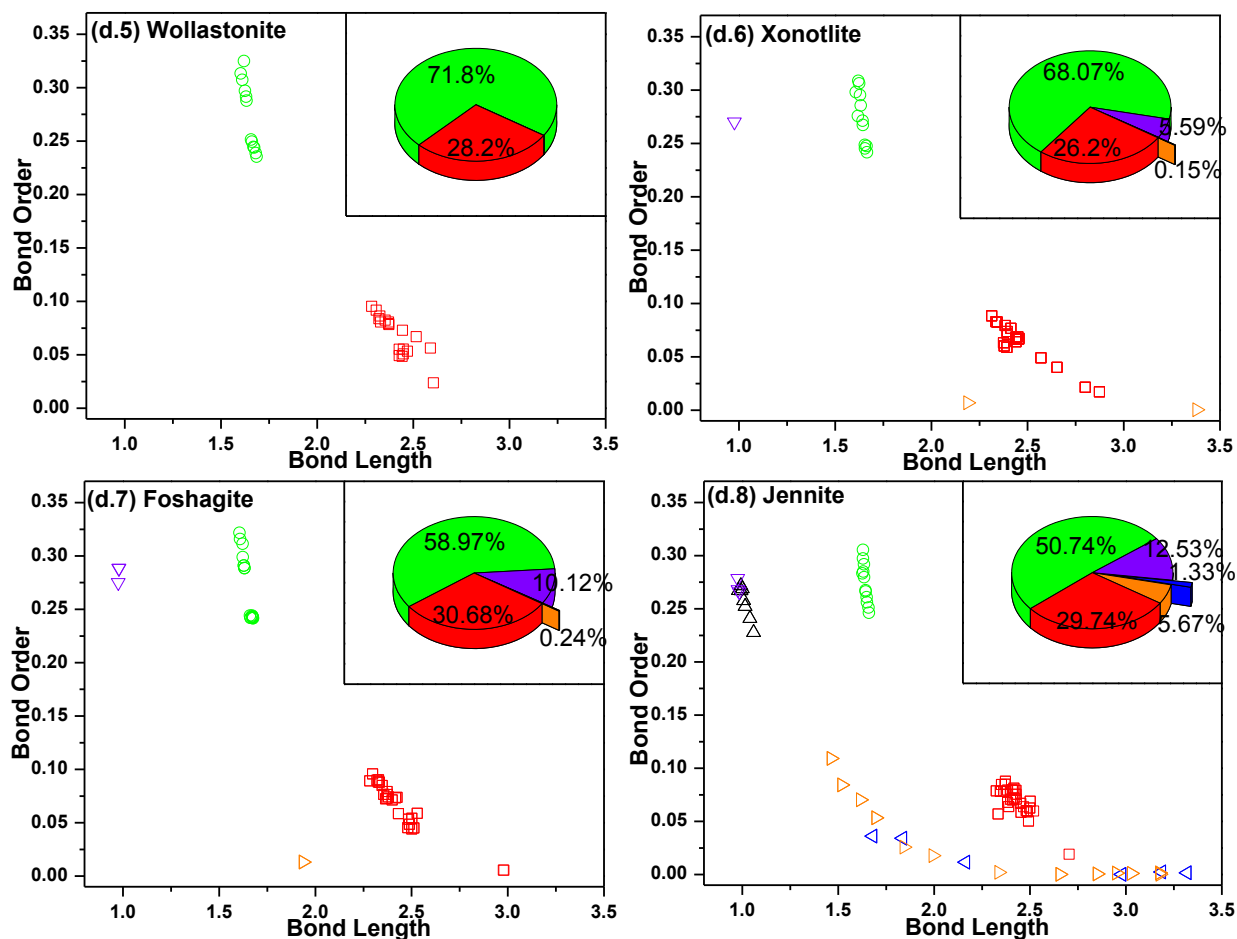


Figure 11. BO distribution of main bond types in 20 CS/CSH crystals. Pie charts in corresponding insets show % BO of each types of bond except covenant bond of H₂O. Color scheme given in the legend is common to both scatter plots and pie charts.

The **group b** crystals contain the **Q⁰** silicates as well as covalent O-H bonds and HBs. In this group, only Afwillite contains water molecules (**Figure 11**). These crystals have a broadly dispersed Si-O BO although with well-defined narrowly ranged BL. The lower Si-O BO is generally associated with the Si-OH (hydroxyl) bond, while the higher BO with Si-O bonds within the tetrahedral unit. The Ca-O BO in **group b** crystals is significantly smaller and shows a narrow distribution over a wide range of BL. Further, the covalent O-H bonds and HBs exhibit a wide range of BO and BL as expected. For all the crystals in this group, the contributions from Ca-O, O-H bonds and HBs to the

TBO are almost 50% or more. For example, in Afwillite (b1), the contributions to the TBO are as follows: Si-O (48.2%), Ca-O (28.6%), O-H (14.1%) and O...H (8.7%). Here the covalent O-H bonds are connected to the silicate tetrahedral units $[\text{HSiO}_4]^{-3}$ through HBs whose BLs varies between 1.38 - 1.98 Å with significant BO values. Therefore, the -O...H contribution in Afwillite is the highest (8.71%) in this group. Rastsvetaeva et al.⁷⁶, in their IR spectrum analyses of Afwillite⁷⁷, have assigned the characteristic vibrational modes of the so-called zundel cation $(\text{H}_2\text{-O}\cdots\text{H}\cdots\text{OH}_2)^+$, or (H_5O_2^+) ⁷⁸. However, in present BO analysis, it was not observed this zundel cation structure. Instead, two HBs connecting water molecules with close proximity on either side of CaO layer (parallel to b-c plane) was found as shown in **Figure 8** (b.1). Clearly, the interpretation of the IR spectrum could have immensely benefitted from the relaxed structure and BO calculations. In contrast, for α -C2SH (b.2), which contains both Si-OH and Ca-OH, the HB related to Si-OH is relatively stronger (BO = 0.066) compared to those linked to Ca-OH (BO = 0.014). The stronger HBs in α -C2SH (b.2) can be attributed to the fact that this crystal is formed under the high temperature hydrothermal conditions and is stable up to very high temperature⁷⁰. The other two crystals in **group b**, Dellaite (b.3) and Ca-Chondrodite (b.4), show negligible contribution from the HBs because of the larger O...H separations. The Si-O bond, the Ca-O bond and the covalent O-H bond make primary contribution to TBO in these two crystals.

Crystals in the **group c** have an even wider distribution of Si-O BO values than **group b**, ranging from 0.18 to 0.35 (**Figure 11**). The contribution from Si-O bonds to TBO, in general, larger in **group b** whereas contribution from HBs is comparatively less. In this group, Kilchoanite (c.3) is a naturally occurring anhydrous crystal⁷⁹ with two

types of silicate chains (Q^0 and Q^2) coexists⁸⁰. For crystals other than Kilchoanite (c.3), the O-H covalent bonds are clustered in a very narrow range similar to **group a and b** and the HBs follow the similar range as in **group b** (1.5 Å - 1.80 Å). Although the **group c** crystals share the Strunz classification, they exhibit wide differences in structural and bonding characteristics. For example, the Killalaite (c.4) is a complex non-stoichiometric crystal with partial occupancy. It is composed of Q^1 silicate chains via a corner sharing O with the Si-O-Si angle of 124.8°. This crystal contains both Si-OH and Ca-OH units. The Si-O BO distribution is very broad (0.195 - 0.322) over a relatively narrow range in BL (1.60-1.72 Å). The HBs have relatively high BOs (0.045 – 0.102) with a BL in the range of (1.50-1.74 Å). The highest BO of HBs is Si-OH...O and Ca-OH...O. The percentage contribution to TBO from Si-O, Ca-O, O-H, and HBs are 54.3%, 34.33%, 10.03% and 1.33% respectively. On the other hand, Jaffeite (c.5) has a completely different structure and bonding with 12 covalent OH bonds in the form of Ca-OH but virtually no HBs. All the hydroxyl groups connected to Ca are directed away from the disilicate chains. Clearly, Jaffeite (c.5) is an outlier in terms of BO contributions compared to the other crystals in **c**. It has the lowest Si-O contribution (34.1%) among the 20 crystals considered, hence the lowest TBOD. Of all the crystals in **group c**, Suolunite (c.2) is the most conspicuous. It contains primarily Q^1 Si-tetrahedra, as opposed to others that have both Q^0 and Q^2 . Suolunite (c.2) is the only crystal in this group that contains water molecules, and is the only naturally occurring CSH crystal to have a CaO:SiO₂:H₂O ratio of 1:1:1⁸¹. All water molecules in Suolunite (c.2) have a consistent covalent bond length of 1.0033 Å. Since these water molecules are far apart so the H₂O...H type HBs are absent. All the other HBs have short BL (1.5 - 1.76 Å) and

relatively strong BO (0.042 – 0.084). Both Q^0 and Q^1 type silicates units in Suolunite (c.2) have one covalent O-H bond which also make HBs with the nearby O of the silicate chain with a BL (1.543 Å) and BO (0.085). The rest of HBs are from water molecule to the O of the adjacent silicate chains. It is interesting to note that $-O\cdots H$ has twice as large BO value than the HBs from water molecules. Suolunite (c.2) and Rosenhahnite (c.1) have same C/S ratio but the latter has no water molecules. Hence, the HBs contributions to the TBO are significantly small. More focused discussion on Suolunite to be done in later section.

In **group d** crystals, the contribution of Si-O bonds in the infinite silicate chain structures dominates the TBO (**Figure 11**). However, the Si-O contribution to the TBO generally decreases as the C/S ratio increases. In addition, the layer separation, H_2O/OH content and crystal symmetry also affect the BO contributions. The CSH crystals in this group are amongst the most hydrated, except Wollastonite (d.5) which is an anhydrous precursor phase with 71.8% Si-O bonds and 28.2% Ca-O bonds ⁸². The Si-O BO values of this group exhibit dispersion primarily due to small distortions from the ideal tetrahedral unit and the hydroxyl ions connecting the silicate chains and Ca. Two types of silicate chains are observed: (1) the single silicate chain as those found in d.1, d.3, d.4, d.5, d.7 and d.8; and (2) the double silicate chain in which 2 silicate chains from either side of the interlayer are connected via a bridging-O as in d.2 and d.6 ⁷⁰. The presence of silicate chains leads to a layered structure of these minerals as well as high contribution of Si-O to the TBO. The interlayer separations between layers range from 4.95 Å in Foshagite (d.7) to 14 Å in T14 (d.3). The layered structure formed by these chains has a significant effect on the mechanical anisotropy of these crystals. Typically,

water molecules and Ca reside in interlayer cavities and govern the interlayer cohesion⁷³. For example in Nekoite (d.1), the interlayer (of separation 7.6Å) contains all Ca and H₂O. In this case, the Ca-O bond contributes 15.24% and the HBs contribute 5.21% to the interlayer cohesion. In contrast, the T11 (d.2) has H₂O in the interlayer but no Ca, thus HBs contribute 4.04%, whereas in T14 (d.3) and T9 (d.4), which has both Ca and H₂O, the Ca-O bond contributes 4.07% and 4.86% and the HBs contribute 5.48% and 3.17%, respectively to the interlayer cohesion. The difference in T14 (d.3) and T9 (d.4) is attributed to the lack of double silicate chains in former and the presence in later. Further, Xonotlite (d.6) and Foshagite (d.7) have unusually low contribution of HBs since these crystals contain only hydroxyl ions. In **group d**, Jennite (d.8), which has been widely considered as part of the C-S-H phase in hydrated cement, has the highest contribution of HBs (6.99%) to the interlayer cohesion.

4.7 Quantum mechanical metric for internal cohesion in CSH

This study presented the calculated electronic structure of 15 CSH crystals, 4 anhydrous precursor crystals and portlandite crystal. Band structures show all crystals are large band gap insulators. The BO topology and their contribution to the overall cohesion via TBO were also analyzed. Thus, no specific rule common to all crystals were found but observed some trends for each group separately. The BO, TBO and TBOD of the various crystals clearly shows (1) the diverse degree of contributions of the various bond types to the overall crystal cohesion, (2) the variety of HBs, (3) the BO dispersion within each bond types in CSH, and (4) the importance of accurate crystal structure whose volume determines the TBOD. The traditional criterion for classifying

CSH crystals using C/S ratio is rather rudimentary in view of these diversities. This study proposes the total bond order density (TBOD) as an accurate quantum mechanical metric to classify the CSH crystals that provides far deeper insight to cohesion and strength of these materials.

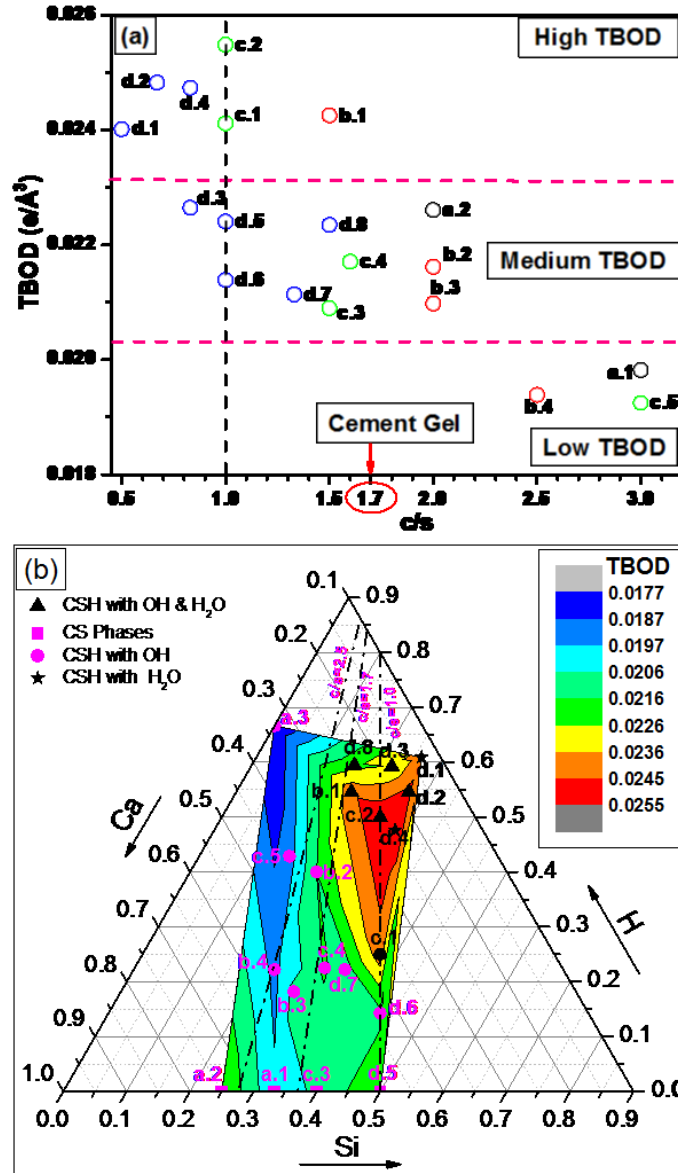


Figure 12. (a) Total bond order density vs. C/S ratio in 19 crystals. (Portlandite (a.3) was excluded since it has no Si atoms.); (b) TBOD distribution map vs. the composition of Ca:Si:H. The color bar labels the values for the TBOD. The dot-dash lines indicate specific C/S ratios.

Figure 12 (a) shows the plot of TBOD vs the C/S ratio showing an approximate inverse relationship. It is apparent that crystals with the same C/S ratio can have very different TBOD. Since TBOD is more sensitive to the bonding and relevant to cohesion, use of it for classifying CSH crystals is more appropriate. This plot also shows that the four groups discussed above do not cluster together in relation to the TBOD. **Group c** has a wide range of C/S as well as TBOD. However, **group d**, believed to be closest to hydrated cement, has a narrow distribution in C/S but a wider TBOD range. Roughly speaking, it is possible to divide the 20 crystals into 3 groups according to their TBOD – high, medium and low. Crystal's a.1, b.4 and c.5 belong to the low TBOD group mainly because of the high C/S ratio. On the opposite end, b.1 from **group b**, c.1 and c.2 from **group c** and d.1, d2 and d4 from **group d** belong to the high TBOD group. The rest of 10 crystals belong to the medium TBOD group which mostly from **group d** crystals. The mixing of groups based upon Strunz classification and a weak correlation of TBOD with C/S ratio signifies the complex interplay and tradeoffs between the covalent bonds and HBs in these CSH structures. Although, Q^n chains in **group d** crystals tend to reduce C/S ratio, interlayer hydroxyl; water and HBs drastically alter the TBOD by increasing the effective volume without modification to C/S ratio. For example, crystal T14 (d.3) has a low C/S ratio but still has medium TBOD. The reason is that there are two types of silicate. Both d.2 and d.4 structures have double silicate chains whereas d.3 has only single silicate chains, which affects the TBOD considerably.

Measured mechanical properties for CSH crystals are difficult to obtain due to various practical limitations such as challenges in synthesizing single crystals, fast reaction with atmospheric water etc. Thus, there are only a few of CSH/CS phases

where the mechanical properties were obtained experimentally. For example, the clinker phases Belite (a.1) and Alite (a.2), which have well-defined stoichiometric structures, are reported to have experimentally measured Young's modulus (E) between 140-130 GPa and 147-135 GPa respectively ⁸³. Similar experiments reported the E for Portlandite (a.3) to be in the range 36-48 GPa ^{60-61, 83b, 84} depending on the porosity and a bulk modulus value of 39.65 GPa ⁵⁵. The bulk modulus of the crystal Toberomite 14Å (d.3) obtained recently using high pressure synchrotron X-ray diffraction to be 47 GPa ⁵⁹. Using these limited experimental values, this study found that the average of the measured E values for a.1, a.2 and a.3 crystals increase as a function of TBOD and show a near linear fit. In addition, the measured bulk modulus found for the two crystals, i.e. a.3 and d.3 also increase with TBOD. At this stage it is premature to correlate experimental mechanical properties with calculated TBOD. Thus it is necessary to study this further with the calculated mechanical properties to find possible trends of mechanical properties with the TBOD.

Since Ca, Si and H are the primary components of the various bond types in CSH, it is useful to examine the complex interactions amongst the bond types by investigating the TBOD as function of Ca:Si:H ratio. **Figure 12 (b)** shows the color-coded ternary plot of TBOD map with respect to Ca:Si:H composition. The resultant contour plot gives a vivid illustration of the possible locations for phases with high TBOD which appear to concentrate in the region where Ca:Si:H = 0.25:0.25:0.5. It was noted that Soulunite (c.2) with C/S ratio equal to 1 has the highest TBOD out of the 20 crystals investigated and according to applied criterion, would be closest to the ideal

composition and structure. The narrow green and yellow areas in **Figure 12 (b)** represent the medium TBOD. The wider blue regions represent the low TBOD regions.

4.8 Electronic structure of suolunite

As shown in the previous section, Suolunite (C.2) has shown a unique bonding and an ideal composition for CSH. Thus it is worth investigating further. The electronic structure and bonding of Suolunite has not been investigated until now. Thus, further discussion was done on its electronic structure with the presentation of its total density of states (DOS) and partial density of states (PDOS) resolved in accordance with the atoms involved in different types of bonding. To analyze the electronic structure of CSH crystals, the total density of state (DOS) and atom-resolved partial DOS are very illuminating. Here it is possible to present (see **Figure 13**) the calculated total and partial DOS of Suolunite, the crystal highlighted in the main text as the one with highest TBOD and most ideal structure and composition. The top panel shows the total DOS and six panels beneath show the PDOS of isolated H₂O, the -OH hydroxyl group, the HB with O (O-HB), the bridging O between 2 Si tetrahedra, the Si and Ca atom respectively. For clarity, the scale of Y-axis were set different in different panels (see **Figure 13**). In the total DOS the lower energy states within -15 eV to -20 eV are from Ca 3p, Si 3s/3p and 2s orbitals of O as marked. The main contributors to the DOS at the top of the valence band come from the O-HBs and -OH. The peaks in the range from -5 eV to -7.5 eV are from O-2p orbitals of -OH, H₂O and 1s orbitals of the H. The peaks between -7.5 eV and -10 eV are from Si-3p, bridging-O and -OH. The conduction band states are mostly from the 3d states of the Ca. However, some contribution from the 3d

states of the Si and 2p states of O-HBs, -OH and H₂O can also be observed. Similar TDOS and PDOS for all 20 crystals are available but are not presented here.

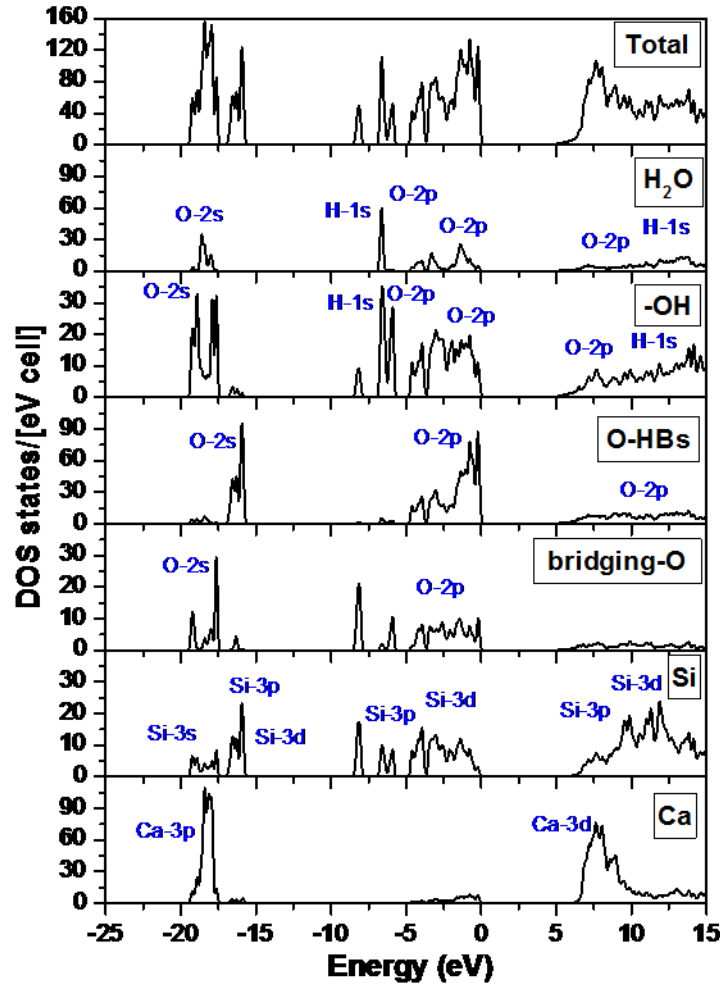


Figure 13. Total and partial DOS of Suolunite. The DOS scale is made different for PDOS for clarity.

4.9 Discussion and conclusion

In C-S-H (cement hydrates), it is known that infinite chain structures are absent⁴. On the other hand, it is widely believed that mixtures of tobermorite (d.2-d.4) and jennite (d.8) form the template or backbone of the C-S-H disordered structure. However, the TBOD and the BO calculations show that C-S-H structures in hydrated cements cannot

simply be surmised as mixtures of CSH crystals or even some disordered form of these mixtures. In this regard, the following three aspects become clear: (1) the significant contribution of HBs and their role in affecting the BO of each bond type, (2) the significant dispersion in BO of the strong Si-O bonds with small BL variation, and (3) the variation in the BO of relatively weaker Ca-O bond. Since the interplay between different components from the structures cannot be explicitly quantified by known experiments^{63b}, detailed electronic structure and bonding information are necessary to interpret experimental findings, especially in spectroscopic studies such as in Raman, IR and NMR measurements^{68, 76, 85}. The implication is that attempts to use vibrational spectroscopy, such as IR or Raman, for structural interpretation have to be viewed carefully with special attention paid to small features and nuances, such as peak width and asymmetry.

From the viewpoint of mechanical properties, which are highly important for this material class, it was noted that silicates with strong covalent bonds are expected to contribute significantly to the overall crystal stiffness under small deformation. However, hydrated crystals with a low degree of polymerization may have considerable contributions to the materials stiffness via HBs in the HB network. Bond order analysis on crystals with finite silicate chains shows that H₂O, OH and HB network all play a key role in the cohesion of crystals. More significantly, the Si-O covalent bonds are unlikely to be the main source of crystal strength as often reported in the literature⁶. In multi-component crystals that include ionic, covalent and hydrogen bonds and the nonlinearity of mechanical response, the failure and the fracture behavior is often controlled by the weaker ionic or hydrogen bonds. Indeed, in these complex material

systems, different atomic-scale deformation mechanisms trigger and persist under different loading paths⁸⁶. For the CSH crystals as well as the more disordered C-S-H, both the silicate polymerization and the BO of various bond types will affect the deformation mechanisms. In this respect, highly polymerized structures, such as Tobermorite and Jennite, are likely to have highly anisotropic mechanical response with stiff response along the silicate chains complimented by planes of weaknesses. Suolunite, which has the highest TBOD, a high contribution of HBs and a low degree of polymerization of silicates, is likely to have a comparably high stiffness and absence of weak planes.

In conclusion, this study has presented a compelling argument for using a quantum mechanical metric, the BO and the TBOD as the most important criterion to assess the crystalline cohesion in CSH crystals. This metric encompasses effects of both the geometric factors and the interatomic interactions. Therefore, the BO and TBOD provide a much more in depth measure for the overall behavior of this diverse class of materials. The TBOD should certainly replace the long-standing and traditionally used C/S ratio in classifying cement materials. Of the 15 CSH crystals studied, the inconspicuous crystal Suolunite turns out to have the highest TBOD, and the ideal composition, structure and bonding characteristics for cement hydrate. This finding should serve as an impetus for cement scientists engaged in molecular scale engineering of hydraulic cements. Synthesis of new anhydrous precursors or hydration pathways that lead to Suolunite type hydration products could yield robust infrastructural materials. Furthermore, the results of this study make it amply clear that the understanding of electronic structure and inter-atomic bonding characteristics is

essential for the interpretation of experimental spectroscopic data as well as for the development of realistic structural models of disordered cement hydrates. The approach used in this study has application to a broad class of complex material systems that incorporate covalent, ionic and hydrogen bonds, such as the apatite mineral class relevant to biological systems.

CHAPTER 5

NATURE OF INTERATOMIC BONDING IN CONTROLLING THE MECHANICAL PROPERTIES OF CALCIUM SILICATE HYDRATES

5.1 Introduction

The demand for cementitious materials is expected to continually increase as the global need for modern infrastructure grows. Hydraulic cements are the key material for the construction industry. Calcium silicate hydrate (C-S-H) is the most important phase of hydrated cement gel comprising more than 60% of its volume ⁴. Based upon experimental techniques such as neutron scattering ^{38, 87} and synchrotron X-ray diffraction ³⁹ the structure of C-S-H was suggested as composed of lamellar stacks that form ~4 nm-sized blocks. In general, the C-S-H gel is amorphous with no long-range order. However, it is generally accepted that in short range order, crystalline minerals such as tobermorite or jennite may exist ⁴⁵. It is also well-accepted that hardened cement paste consists of either poorly crystalline or completely disordered phases. In all cases, the C-S-H in hardened hydraulic cements typically has complex atomic-scale structures with a variety of inter-atomic interactions. As a consequence, a myriad of speculative atomistic models of disordered C-S-H were proposed (see ^{7, 45} for review). However, the fundamental basis of structure-property relationships connecting the different types of inter-atomic bonding to the mechanical stiffness and cohesion in C-S-H remain elusive.

This study intends to address this lack of connection between interatomic bonding and mechanical properties by means of accurate *ab-initio* calculations on crystalline calcium silicate hydrate (CSH) which provide a quantitative measure of inter-atomic bond cohesion and test its correlation to mechanical properties. It is shown that the mechanical behavior of CSH crystals are controlled by the electronic structure and a delicate balance of different types of inter-atomic bonding characteristics including hydrogen bonding ⁷³. To avoid any ambiguity in describing two different types of materials, the symbol C-S-H (with dashes) is used to refer to the more general class of calcium silicate hydrate gels which is typically noncrystalline and of larger scale as compared to CSH (no dash) that refers to the specific crystalline phases with well-defined atomic positions. Although one may argue that the complex non-crystalline C-S-H gel may not represent crystalline CSH phases, there are compelling reasons for investigating CSH crystals as the baseline for revealing the fundamental nature of C-S-H. These reasons are (1) The difficulty of constructing reliable and representative atomic models for C-S-H, and (2) Lack of definitive conclusions from experimental analyses of the hydrated cement paste based on poorly defined and hard to measure parameters such as atomic composition, elastic properties, and water content in presence of different and defective CSH phases. In fact, accurate assessment of mechanical properties of even the crystalline phases is a daunting task ^{60, 88}. Reliable measurements are very arduous to perform due to practical limitations such as difficulty in synthesizing single crystals, presence of small impurities, reaction with atmospheric water etc. On the other hand, it is possible to mitigate these practical limitations by using accurate *ab-initio* simulations to present both the mechanical properties and the

electronic structures of CSH crystals. Precise quantification of bonding characteristics based upon quantum mechanical calculations and their relationship to mechanical properties can then serve as a platform for systematic evaluation of a wider class of calcium silicate hydrates. Such quantification can suggest novel hydrate structures of optimal compositions and superior properties⁸⁹, thus guide design of new hydraulic cementitious materials. Previous studies show that the CSH phases can serve as a point of departure for establishing features of the electronic structure and inter-atomic bonding characteristics within cement hydrates^{25e}. In particular, a single quantum mechanical metric, the total bond order density (TBOD), can predict the most robust CSH phase instead of relying on the traditional Ca/Si (C/S) ratio (see chapter 4).

5.2 Computational modeling details

The technical details of VASP relaxations (section 2.3.1) for all crystal structures in this work are briefly outlined as follows: (1) The PAW-PBE potentials within the generalized gradient approximation(GGA) for the exchange-correlation potential; (2) electronic convergence criterion set at 10^{-6} eV with an energy cutoff of 500 eV; (3) The force convergence criterion set at 10^{-5} eV/Å for each ionic step relaxation.; (4) sufficiently large number of *k*-point-meshes ranging from 4 to 85 k-points are used depending on the actual crystal structure and size. The VASP relaxed crystal structures are used to calculate the elastic tensors for these four crystals using an efficient method discussed in section 2.3.2. The choice of $\pm 0.5\%$ strain for calculating the elastic tensor within the framework of stress-strain method discussed in chapter 2. The electronic structure and

BO calculations and TBOD were carried out using the OLCAO method as discussed in section 2.2.

5.3 Results and discussion

5.3.1 Relationship of CSH minerals with cement gel

Over the past century there were numerous experiments undertaken in an attempt to understand micro and/or nano structure of cement gel. At this point it is useful to establish a connection of CSH crystals with the hydrated cement gel which has undergone experimentation for decades. The 20 CSH crystals considered in this study are listed in four groups (**a**, **b**, **c**, **d**) using the modified Strunz classification⁶⁵ in accordance with silica chain polymerization [11]. For a complete description of Strunz groups as considered in this thesis are given in section 4.3. A suite of experimental techniques including small angle neutron scattering (SANS), nuclear magnetic resonance, X-ray diffraction, micro-Raman spectroscopy and different types of IR spectroscopies as well as controlled drying of hydrated samples were used in the past to determine the structural water content and to identify an overall chemical composition of cement gel^{38, 63b}. It is a popular belief that structural water holds the key to understand the micro/nano structure of the cement gel^{63b}. Cong and Kirkpatrick performed drying experiments for 40 days under N₂ gas (to avoid carbonation with CO₂) on single phase C-S-H prepared by hydration and pozzolanic reactions to identify structural water content variation with the Ca/Si (C/S) ratio to derive a chemical formula^{63b}. They proposed an ideal formula $\text{Ca}_{4.5} [\text{Si}_3\text{O}_8(\text{OH})](\text{OH})_4 \cdot n\text{H}_2\text{O}$, for C-S-H with a C/S

ratio of 1.5. Drying experiments were uncertain as it may affect microstructure in cements. SANS experiments done by Allen *et. al.* ³⁸ avoid this drawback of the drying experiments by directly characterizing hydrated gel where cements were mixed with a 0.4 w/c mass ratio, hydrated for 28 days in H₂O at 20 °C. They proposed an overall chemical formula, (CaO)_{1.7}(SiO₂)(H₂O)_{1.80} for C-S-H particles with a density of 2.604 gcm⁻³ ^{63b}. However, this value was judged to be inaccurate due to calculation error ⁷. The variations of H₂O/Si ratio with the C/S ratio for C-S-H cement gel from both these experiments are shown in **Figure 14** (solid symbols) which have a rough linear relationship indicated by the solid line. Recent simulation study by Qomi *et. al.* ⁹⁰ on CSH also show a linear trend in agreement with the experiments. They suggest that a “good measure” to compare simulation results with experiment is to use “effective water content” which is defined to include both H₂O and OH such that 2 OH units account for 1 effective H₂O, and not the actual water content. **Figure 14** also shows the H₂O/Si verses C/S data (open symbols) from present study for the CSH crystals. Different colors and shape of symbols designate each Strunz group ^{25e} (see **Table 8**). The CSH considered in this study falls into two separate trends shown in red and blue dashed lines. The crystals related to red dashed line are close to the experimental trend than the crystals related to the blue dashed line. The 7 CSH crystals related to blue dashed line consists of only OH (converted into “effective water”). The data for c.5 (jaffeite) is an outlier for both linear trends. Jaffeite (c.5) crystal has Ca-OH unit and the hydroxyls are oriented in such a way that virtually no hydrogen bonds can be formed based on the distance of ~2.75Å for hydrogen bonding ⁹¹. The experimental data from both drying experiments of Cong *et al.* ^{63b} and SANS experiments of Allen *et al.* ³⁸ on cement paste

relate reasonably close to the red dashed line but with slightly different slopes. Based on this result it is possible to infer that in cement paste, both water and hydroxyls groups may exist. This conjecture is quite intuitive because there are overwhelming evidence that cement gel consists of both H_2O and OH . Conversely, it could be argued that in real cement paste there may exist many CSH phases that have not been considered in prior proposed models. For example the crystals c.2 (suolunite) and b.1 (afwillite) have a H_2O/Si and C/S ratio that is closer to what experimentally observed in cement gel. Both phases are high in hydration and strong mechanical properties (see **Section 5.3.2** below).

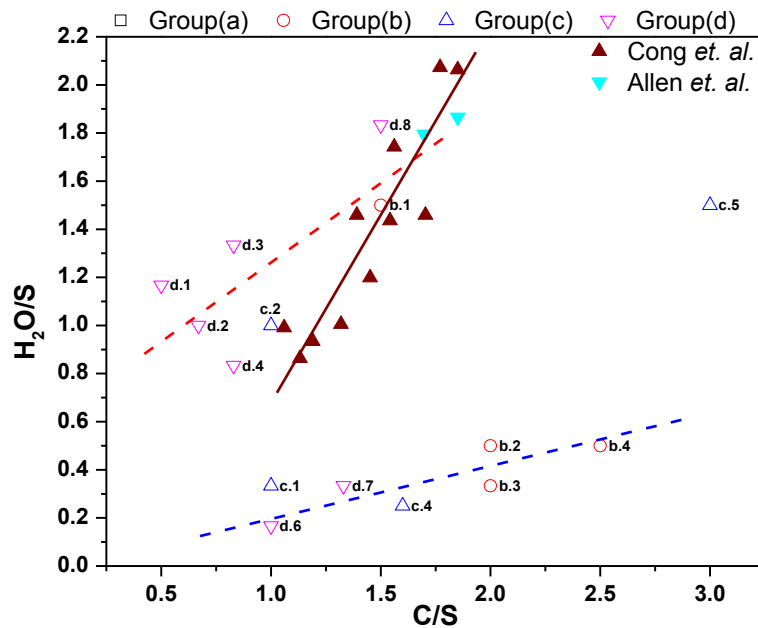


Figure 14. Effective water content to Si ratio (H_2O/Si) vs C/S ratio in the present study (open symbols for different groups). The effective water content is comparable with total water measured in SANS performed by Allen *et. al.* ³⁸ and a set of controlled drying experiments by Cong and Kirkpatrick ³⁷ (solid symbols). The solid and dashed lines are guides to the eye for an approximate linear correlation.

Table 8. Designated label for each class, mineral name[chemical formula], SiO-BOD, CaO-BOD and HB-BOD, TBOD, (BOD x 10⁻³) Bulk modulus (K), shear modulus (G) and Young's modulus (E) (GPa) of 20 crystal phases.

| # | Crystal | SiO-BOD | CaO-BOD | OH-BOD | HB-BOD | TBOD | K | G | E |
|-----|--|---------|---------|--------|-------------|--------------|------|------|-------|
| a.1 | Belite [2(CaO) SiO ₂] | 12.47 | 10.11 | 0.00 | 0.00 | 22.59 | 96.8 | 49.0 | 125.7 |
| a.2 | Alite [3(CaO) SiO ₂] | 8.68 | 11.06 | 0.00 | 0.00 | 19.74 | 97.5 | 53.1 | 134.9 |
| a.3 | Portlandite [Ca(OH) ₂] | 0.00 | 7.96 | 9.78 | 0.00 | 17.73 | 35.1 | 17.2 | 44.4 |
| b.1 | Afwillite [Ca ₃ (SiO ₃ OH) ₂ ·2H ₂ O] | 9.71 | 5.77 | 6.97 | 1.81 | 24.26 | 70.3 | 33.5 | 86.7 |
| b.2 | α-C2SH [Ca ₂ (HSiO ₄)(OH)] | 9.12 | 7.27 | 4.52 | 0.70 | 21.61 | 71.9 | 36.8 | 94.2 |
| b.3 | Dellaite [Ca ₆ (Si ₂ O ₇)(SiO ₄)(OH) ₂] | 10.60 | 8.52 | 1.78 | 0.06 | 20.96 | 82.2 | 43.8 | 111.7 |
| b.4 | Ca Chondrodite [Ca ₅ [SiO ₄] ₂ (OH) ₂] | 8.60 | 8.49 | 2.24 | 0.05 | 19.39 | 82.3 | 42.5 | 108.8 |
| c.1 | Rosenhahnite [Ca ₃ Si ₃ O ₈ (OH) ₂] | 15.02 | 5.98 | 2.47 | 0.64 | 24.12 | 76.2 | 43.6 | 109.9 |
| c.2 | Suolunite [Ca ₂ (Si ₂ O ₅ (OH) ₂)H ₂ O] | 12.88 | 4.95 | 6.10 | 1.56 | 25.49 | 75.3 | 50.1 | 123.0 |
| c.3 | Kilchoanite [Ca ₆ (SiO ₄)(Si ₃ O ₁₀)] | 13.16 | 7.74 | 0.00 | 0.00 | 20.90 | 83.1 | 45.5 | 115.5 |
| c.4 | Killalaite [Ca _{6.4} (H _{0.6} Si ₂ O ₇) ₂ (OH) ₂] | 11.78 | 7.45 | 2.18 | 0.29 | 21.70 | 83.2 | 49.3 | 123.5 |
| c.5 | Jaffeite [Ca ₆ [Si ₂ O ₇](OH) ₆] | 6.58 | 7.89 | 4.76 | 0.02 | 19.25 | 66.1 | 36.2 | 91.8 |
| d.1 | Nekoite [Ca ₃ Si ₆ O ₁₅ ·7H ₂ O] | 13.18 | 2.52 | 7.44 | 0.86 | 24.01 | 62.0 | 34.1 | 86.4 |
| d.2 | T11 Å [Ca ₄ Si ₆ O ₁₅ (OH) ₂ ·5H ₂ O] | 13.65 | 3.73 | 6.57 | 0.84 | 24.80 | 67.7 | 37.1 | 94.1 |
| d.3 | T14 Å [Ca ₅ Si ₆ O ₁₆ (OH) ₂ ·7H ₂ O] | 11.01 | 3.69 | 6.96 | 0.90 | 22.56 | 49.3 | 30.2 | 75.3 |
| d.4 | T 9 Å [Ca ₅ Si ₆ O ₁₇ 5H ₂ O] | 13.85 | 4.48 | 5.71 | 0.63 | 24.66 | 75.6 | 39.7 | 101.3 |
| d.5 | Wollastonite [Ca ₃ Si ₃ O ₉] | 16.09 | 6.32 | 0.00 | 0.00 | 22.41 | 91.9 | 47.3 | 121.0 |
| d.6 | Xonotlite [Ca ₆ Si ₆ O ₁₇ (OH) ₂] | 14.56 | 5.60 | 1.20 | 0.03 | 21.39 | 79.7 | 49.6 | 123.3 |
| d.7 | Foshagite [Ca ₄ (Si ₃ O ₉)(OH) ₂] | 12.46 | 6.48 | 2.14 | 0.05 | 21.14 | 73.6 | 41.4 | 104.7 |
| d.8 | Jennite [Ca ₉ Si ₆ O ₁₈ (OH) ₆ ·8H ₂ O] | 8.61 | 5.05 | 7.50 | 1.19 | 22.34 | 56.1 | 29.1 | 74.4 |

Table 9. . Major elastic constants (GPa), Poisson's ratio (γ) percentage Ca, Si, hydroxyl (OH) and H₂O atoms (in the simulation cell) of 20 crystal phases.

| label | C ₁₁ | C ₂₂ | C ₃₃ | C ₄₄ | C ₅₅ | C ₆₆ | C ₁₂ | C ₁₃ | C ₂₃ | γ | Ca% | Si% | OH% | H ₂ O% |
|------------|-----------------|-----------------|-----------------|-----------------|-----------------|-----------------|-----------------|-----------------|-----------------|----------|------|------|------|-------------------|
| a.1 | 170.1 | 199.3 | 170.9 | 46.7 | 31.2 | 54.1 | 46.7 | 64.7 | 58.2 | 0.284 | 66.7 | 33.3 | 0.0 | 0.0 |
| a.2 | 161.7 | 190.2 | 165.2 | 61 | 53.8 | 43 | 56.3 | 56.3 | 72.8 | 0.270 | 75.0 | 25.0 | 0.0 | 0.0 |
| a.3 | 102 | 99.9 | 45.9 | 8.1 | 6.3 | 33.5 | 34.6 | 12.1 | 10.4 | 0.289 | 33.3 | 0.0 | 66.7 | 0.0 |
| b.1 | 115.8 | 126.6 | 146.8 | 20.5 | 38.4 | 33.7 | 41.1 | 48.5 | 35.2 | 0.294 | 33.3 | 22.2 | 22.2 | 22.2 |
| b.2 | 115.7 | 110.7 | 125.3 | 44.1 | 37.7 | 35.3 | 48.3 | 50.3 | 49.5 | 0.282 | 50.0 | 25.0 | 25.0 | 0.0 |
| b.3 | 151.8 | 133.9 | 152.8 | 38.9 | 53.2 | 35.6 | 44.3 | 54.5 | 53.7 | 0.274 | 54.5 | 27.3 | 18.2 | 0.0 |
| b.4 | 131.6 | 120.5 | 144.1 | 50.6 | 49.5 | 41.5 | 61.5 | 55.4 | 56.8 | 0.280 | 55.6 | 22.2 | 22.2 | 0.0 |
| c.1 | 136.3 | 168.4 | 146.7 | 57.5 | 32.7 | 32.3 | 38.8 | 30.3 | 56.8 | 0.260 | 37.5 | 37.5 | 25.0 | 0.0 |
| c.2 | 130.5 | 124.1 | 147.2 | 56.9 | 58.9 | 51.1 | 55.8 | 46.1 | 36.8 | 0.228 | 28.6 | 28.6 | 28.6 | 14.3 |
| c.3 | 140.2 | 157.4 | 124.5 | 51.4 | 43.6 | 48.3 | 55.8 | 55.4 | 53.4 | 0.268 | 60.0 | 40.0 | 0.0 | 0.0 |
| c.4 | 140.4 | 166.5 | 164.4 | 58.8 | 42 | 39.9 | 40.9 | 43.6 | 56.9 | 0.253 | 51.2 | 32.5 | 16.3 | 0.0 |
| c.5 | 118.4 | 117.1 | 133.2 | 29.8 | 30.3 | 38.4 | 40.3 | 36.7 | 36.5 | 0.269 | 42.9 | 14.3 | 42.9 | 0.0 |
| d.1 | 97.3 | 115.7 | 126.9 | 36.7 | 32.7 | 31.5 | 38.2 | 35.2 | 43.6 | 0.268 | 18.8 | 37.5 | 0.0 | 43.8 |
| d.2 | 120.8 | 125.2 | 135.2 | 38 | 25.1 | 47.5 | 43.2 | 31.4 | 45.8 | 0.268 | 23.5 | 35.3 | 11.8 | 29.4 |
| d.3 | 98.7 | 106.6 | 79 | 30.2 | 23 | 41.1 | 37.8 | 22 | 27 | 0.246 | 25.0 | 30.0 | 10.0 | 35.0 |
| d.4 | 134.6 | 157.9 | 148.8 | 46.7 | 23.6 | 38.4 | 42.2 | 29.4 | 60.2 | 0.277 | 31.3 | 37.5 | 0.0 | 31.3 |
| d.5 | 146.8 | 191.1 | 171.3 | 44 | 31.7 | 56.6 | 60.9 | 52.3 | 50 | 0.280 | 50.0 | 50.0 | 0.0 | 0.0 |
| d.6 | 149 | 191.2 | 124.7 | 57.2 | 42.9 | 50.4 | 50 | 33.6 | 56.2 | 0.242 | 42.9 | 42.9 | 14.3 | 0.0 |
| d.7 | 121 | 175.7 | 115 | 37 | 34.5 | 53.9 | 54.5 | 41.4 | 40.3 | 0.263 | 44.4 | 33.3 | 22.2 | 0.0 |
| d.8 | 106.3 | 120.9 | 69.8 | 26.5 | 23.5 | 39.5 | 39.9 | 36.8 | 35.1 | 0.279 | 31.0 | 20.7 | 20.7 | 27.6 |

Table 10. Minor elastic constants (GPa) of 20 crystal phases.

| label | C ₁₄ | C ₂₄ | C ₃₄ | C ₁₅ | C ₂₅ | C ₃₅ | C ₄₅ | C ₁₆ | C ₂₆ | C ₃₆ | C ₄₆ | C ₅₆ |
|-------|-----------------|-----------------|-----------------|-----------------|-----------------|-----------------|-----------------|-----------------|-----------------|-----------------|-----------------|-----------------|
| a.1 | -0.2 | -0.2 | -0.2 | -10.1 | 0.4 | -9.8 | 0.0 | 0.0 | 0.0 | 0.0 | 4.9 | 0.0 |
| a.2 | 0.9 | -0.7 | 1.0 | -8.9 | -8.9 | -2.7 | -2.6 | 0.1 | 1.4 | -0.1 | 0.1 | 0.7 |
| a.3 | 0.3 | -3.6 | -0.1 | 5.8 | 0.4 | 1.6 | -0.1 | -3.4 | 0.6 | -0.1 | 1.1 | 3.4 |
| b.1 | 0.5 | -1.2 | 2.4 | 1.2 | -7.2 | 3.4 | -6.9 | 6.1 | -3.1 | -6.6 | -4.6 | 3.7 |
| b.2 | 0.0 | 0.0 | 0.0 | 0.0 | 0.0 | 0.0 | 0.0 | 0.1 | 0.1 | 0.1 | 0.0 | 0.0 |
| b.3 | -2.2 | -2.6 | 1.9 | -3.7 | 1.1 | -8.9 | -2.5 | 3.5 | -5.2 | 0.3 | 0.4 | 1.3 |
| b.4 | -0.2 | 0.4 | 3.1 | 0.5 | 1.5 | 2.3 | 1.6 | 3.4 | 3.5 | 5.9 | 0.4 | 0.7 |
| c.1 | 5.1 | 5.9 | -5.1 | 10.2 | -1.0 | 6.6 | -3.4 | -4.6 | -4.8 | -0.4 | -2.5 | 6.3 |
| c.2 | 0.3 | 0.4 | 0.3 | -2.3 | -3.2 | -1.5 | 0.6 | 0.5 | 0.0 | -0.1 | 0.3 | 0.0 |
| c.3 | 0.0 | 0.0 | 0.0 | 0.0 | 0.0 | -0.1 | 0.0 | 0.0 | 0.0 | 0.0 | 0.0 | 0.0 |
| c.4 | -1.8 | 1.1 | -0.2 | 5.2 | -3.3 | -3.7 | 1.1 | -2.0 | 0.3 | 0.8 | -1.5 | -0.8 |
| c.5 | -0.4 | 0.6 | 0.0 | -0.8 | 0.4 | -0.1 | -0.1 | 0.3 | 0.2 | 0.1 | 0.6 | -0.3 |
| d.1 | 0.9 | -0.7 | -5.9 | 0.0 | -3.7 | -7.5 | -1.0 | -3.7 | -16.1 | -5.2 | -4.5 | -1.8 |
| d.2 | -0.5 | 0.8 | 0.4 | -1.7 | -0.6 | -3.6 | -10.3 | -4.3 | -15.4 | -11.2 | -0.7 | -0.5 |
| d.3 | 2.3 | 4.7 | 6.0 | -0.7 | -1.7 | -5.4 | -9.3 | -0.5 | -9.1 | -5.7 | -1.4 | 1.4 |
| d.4 | -1.4 | 4.3 | 4.3 | 8.9 | 11.8 | 8.1 | -0.8 | -1.0 | -0.9 | -0.5 | 10.6 | -1.3 |
| d.5 | 3.5 | 3.0 | -0.2 | 12.8 | -1.8 | -0.9 | -2.8 | -1.9 | 0.3 | 0.3 | 3.1 | 3.0 |
| d.6 | -4.5 | 0.6 | 5.1 | -7.7 | 7.4 | 19.1 | -5.0 | -2.1 | -13.9 | -6.5 | -1.5 | -3.6 |
| d.7 | 0.8 | 0.8 | -0.7 | 3.6 | -4.6 | -18.0 | 1.0 | -0.3 | -1.8 | -0.5 | -0.3 | -0.6 |
| d.8 | 0.1 | -1.3 | -2.1 | -1.6 | -5.1 | 2.7 | 0.9 | -3.0 | -6.9 | 0.8 | -2.6 | 1.0 |

5.3.2 Elastic and mechanical properties of CSH crystals

The linear elastic coefficients C_{ij} and the mechanical properties (**Table 8**) derived from them for the 20 CSH crystals, including one CH and four CS crystals, were computed using *ab-initio* method (described in **Section 2.3.2**). The full set of elastic constants C_{ij} for each crystal are listed in **Table 9** and **Table 10**. Although CSH is a quaternary system, it is labeled as a “ternary” system in practice because oxygen is the common element. The C:S:H composition relates to CaO:SiO₂:H₂O ratio. The H₂O is usually assumed to be the effective water content including H₂O and (OH) collectively. The bulk mechanical properties K, G, E are shown in colored maps as a function of C:S:H (**Figure 15**). These plots show Portlandite to have lowest values for bulk mechanical properties and CS phases (a.1, a.2, c.3 and c.5) have the highest values.

Experimental studies report E for a.1 (Belite) and a.2 (Alite) to be in the range 140–130 GPa and 147–135 GPa respectively ⁸³, which are close to the results of 125.7 and 134.9 GPa respectively in the current study. For the same phases, the Poisson's ratio γ is found to be 0.30 ⁹² also close to results of current study and shown as 0.284 and 0.270 respectively. Experimental results of K, G, E and γ for Portlandite a.3 are 39.65 GPa ⁶¹, 16.36 GPa ⁶¹, 40.3 ⁶⁰ - 36 ^{83b} GPa and 0.30-0.325 ⁶¹ respectively. Results of current study are very close to these experimental values (See **Table 8**). The distribution of calculated mechanical properties shown in the **Figure 15** can provide useful trends in interpreting experimentally measured mechanical properties. Firstly, Portlandite shows lowest mechanical properties. Other 19 crystals can be divided in to 4 classes in terms of bulk mechanical properties. These are, i) clinker and other CS phases, ii) crystals with only hydroxyls (CS-OH), iii) crystals with only water (CS-H₂O), and iv) crystals with both water and hydroxyls. From **Figure 15**, it can be seen that the ascending order of mechanical properties is roughly as follows: Portlandite < [class (iii), class (iv)] < class (ii) < class (i). However, c.2 (Suolunite) is an exception to above rule with unusually high mechanical properties. For all mechanical properties Suolunite is as much or greater than class (ii). Suolunite crystal structure and its electronic properties were discussed in ref ^{25e}.

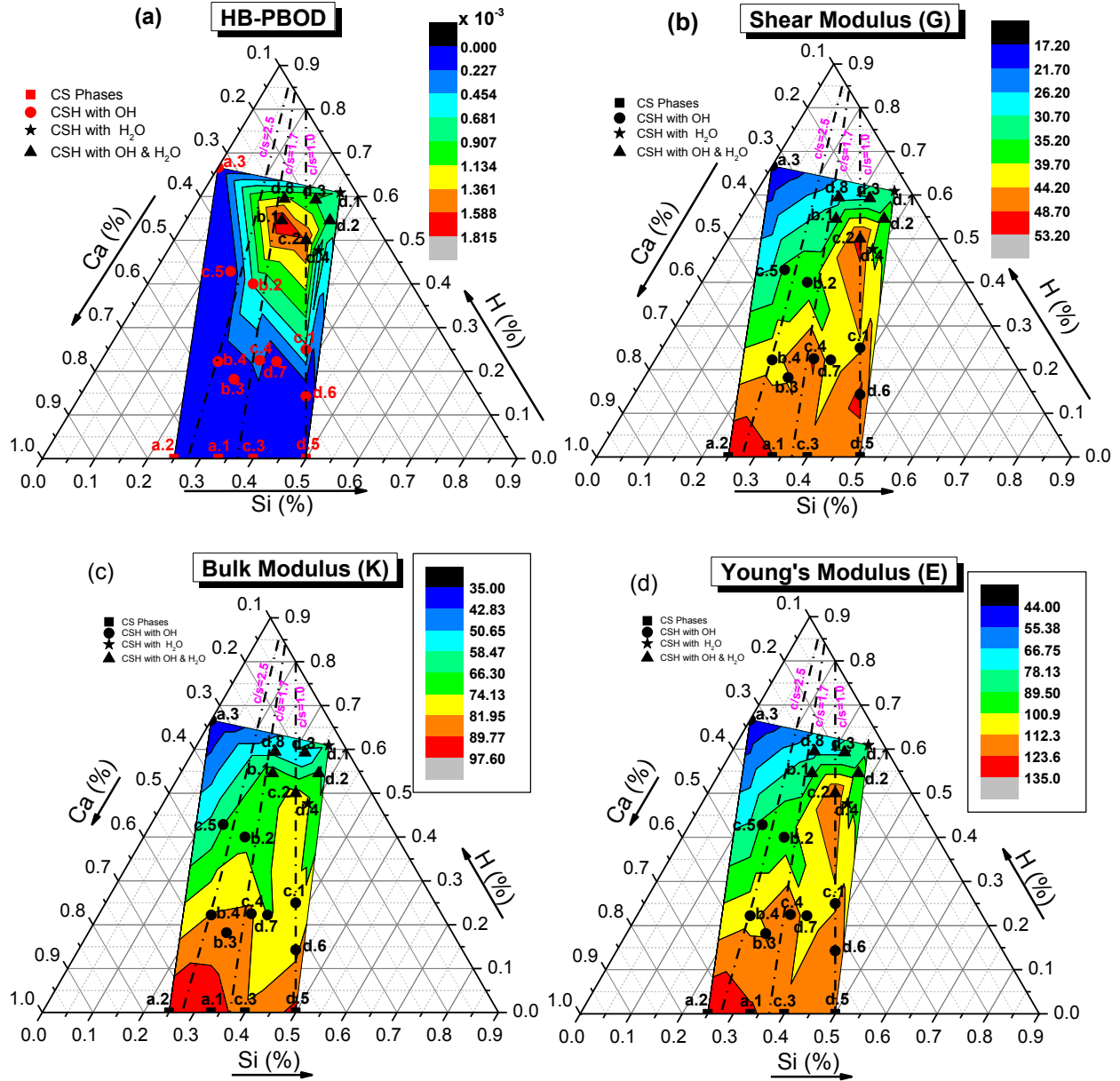


Figure 15. (a) Ternary map of HB-PBOD distribution vs. Ca:Si:H ratio. The color bar label the values for HB-BOD. The dot-dash lines indicate specific C/S ratios. Each data point is marked and represents a crystals according to Table1. (b) Similar ternary maps for the calculated shear modulus G (in unit of GPa) vs. the composition of Ca:Si:H, (c) same for bulk modulus K and, (d) Young's modulus E .

ab initio calculation used in this study provides the full set of elastic coefficient. It is conceivable that the mechanical property of a crystal depends upon its crystal

symmetry which varies greatly in CSH crystals ⁷³. CSH crystals studied here are complex and different from each other making it difficult to interpret the full elastic tensor. Nevertheless, some features can be related to the specific structural details. For example, clinker phase *a.1* and *a.2* have relatively weak mechanical properties in the ***b***-direction whereas Portlandite *a.3* has mechanical anisotropy showing twice as strong in ***a***- and ***b***-directions compared to ***c***-direction. This can be explained from the crystal structure. The hydroxyl groups in Portlandite are sandwiched between the Ca layers in the ***a-b*** plane. The Ca-O bond in Portlandite is particularly strong ^{25e} in comparison with the other CSH crystals. **Group b** and **c** show some anisotropy in the principal elastic constants but it is difficult to relate that to the structural features owing to the lack of long silicate chains. Close inspection of these crystal structures shows some correlation with spatial distance of silicate units to each other in different directions but this is a vague argument. **Group d** has infinitely long silicate chains and identifiable layers. Thus, their mechanical anisotropy is related to the layer and silicate chain directions. In Nekoite (*d.1*), a member in inosilicate with lowest C/S considered in this study is soft in ***a***-direction and stiff in ***c***-direction. This is a sheet structure with silicate sheet in the ***b-c*** plane. Thus the interlayer between the silicates sheets which include water and Ca ions and in the ***a***-direction is mechanically softer compared to ***b*** & ***c*** direction. Wollastonite, the only CS phase in the **Group d** has relatively high stiffness in ***b***-direction due to the silicate chains parallel to ***b***-direction. Xonotlite can be seen as the hydrated phase of wollastonite, having only hydroxyl groups connected to Ca atoms in the intralayer, thus weak in ***c***-direction. Electronic structure calculations show Xonotlite has negligible HBs. Foshagite (*d.7*) has a very similar structure to Xonotlite but has a larger interlayer

separation. Elastic moduli of d.7 in (010) direction is 175.7GPa (**Table 9**) and is close to the DFT calculations reported by J.L. Laugensen (unpublished) 190GPa and the experimentally measured and interpolated from Hertz theory ⁹³ $E_{\text{Hertz}} = 193 \pm 26$ GPa and from JKRS theory ⁹⁴ $E_{\text{JKRS}} = 184 \pm 22$ GPa ⁹⁵. It is necessary to mention here that the mechanical anisotropy and it's relation to the electronic structure was also explained in in chapter 4 for a limited set of 4 crystals ⁷³. All these indicate that the mechanical anisotropy of CSH crystals is complex to analyze.

5.3.3 Relationship of bonding, atomic ratios and H/S ratio to mechanical properties

There are four main types of bonding in CSH crystals ⁷³: The strong Si-O and O-H covalent bonds; Ca-O ionic bonds and the weaker hydrogen bonds (HBs). The inter-atomic bond cohesion for every pair of atoms in the system was quantified in terms of calculated bond order (BO) values (see **Chapter 2**). The BO and bond length (BL) distribution of O-H covalent bonds (both in connected network with Si, Ca and in H₂O molecule) have a very narrow range ^{25e, 73}. They have only minor effect on internal crystal cohesion and bulk mechanical properties. However, the ionic Ca-O bonds and HBs have a much wider range of BO and BL whereas the Si-O covalent bonds show a wide BO range but a narrow BL range. Therefore Si-O, Ca-O and HBs are expected to directly affect the variation of the mechanical properties in different CSH crystals. To establish the relative contributions from different bond types, it is possible to quantify them by defining the partial bond order density (PBOD) as the total BO values of a given bond type divided by the cell volume. These PBOD are designated as SiO-BOD

for Si-O bonds, CaO-BOD for Ca-O bonds and HB-BOD for HBs. The summation of all PBOD gives the total BOD (TBOD). It is listed in **Table 8**, the PBOD, TBOD for each crystal along with the calculated mechanical properties bulk (K), shear (G) and Young's (E) moduli.

As a structural material, the most important property of cement is its mechanical properties. Main objective of this study is to identify some underlying electronic structure/bonding characteristics that relate to the mechanical properties of the CSH crystals. Traditionally, mechanical properties of cement gel were analyzed in terms of atomic compositions, the Ca/Si (C/S) ratio and other empirical parameters. Thus, this study attempt to correlate mechanical properties of the CSH crystals to atomic composition and compare with those derived from accurate quantum mechanical calculations such as TBOD or PBOD. **Figure 16** shows the plots of calculated K, G and E values versus the SiO-BOD, CaO-BOD and HB-BOD in these 20 crystals. Remarkably, the SiO-BOD (**Figure 16-a**), which has the highest contribution for BOD for almost all crystals, does not show any significant correlation with the mechanical moduli. However, **group d** crystals does show an increasing trend with SiO-BOD which is the consequence of the polymeric silicate chain structure. This is a rather surprising and important finding that the increasing contribution of SiO-BOD does not always result in enhanced mechanical properties. On the other hand, the CaO-BOD (**Figure 16-b**) and the HB-BOD (**Figure 16-c**) affect the variation of the mechanical properties more significantly (with the exception of a.3; portandite which contains no silicates and hence much weaker mechanical strength). The fact that mechanical properties having a positive linear correlation with the CaO-BOD indicate that the increased Ca in CSH

generally enhances the stiffness of CSH crystals. The HB-BOD, in contrast, has a rather intricate relationship with mechanical properties. For crystals with very low hydration, the contribution of HB-BOD, and consequently, its effect on mechanical property is negligible. For crystals with significant hydration, the mechanical properties have a negative correlation with the HB-BOD for certain crystal types, mostly with the **group d** crystals, in which increasing contribution of weak HBs results in decreasing mechanical properties. However, crystals with some high HB-BOD such as c.2 (suolunite) and b.1 (afwillite) show enhanced mechanical properties, which is attributed to their specific compact structure and the nature of HBs involved (see **Section 5.3.4** below).

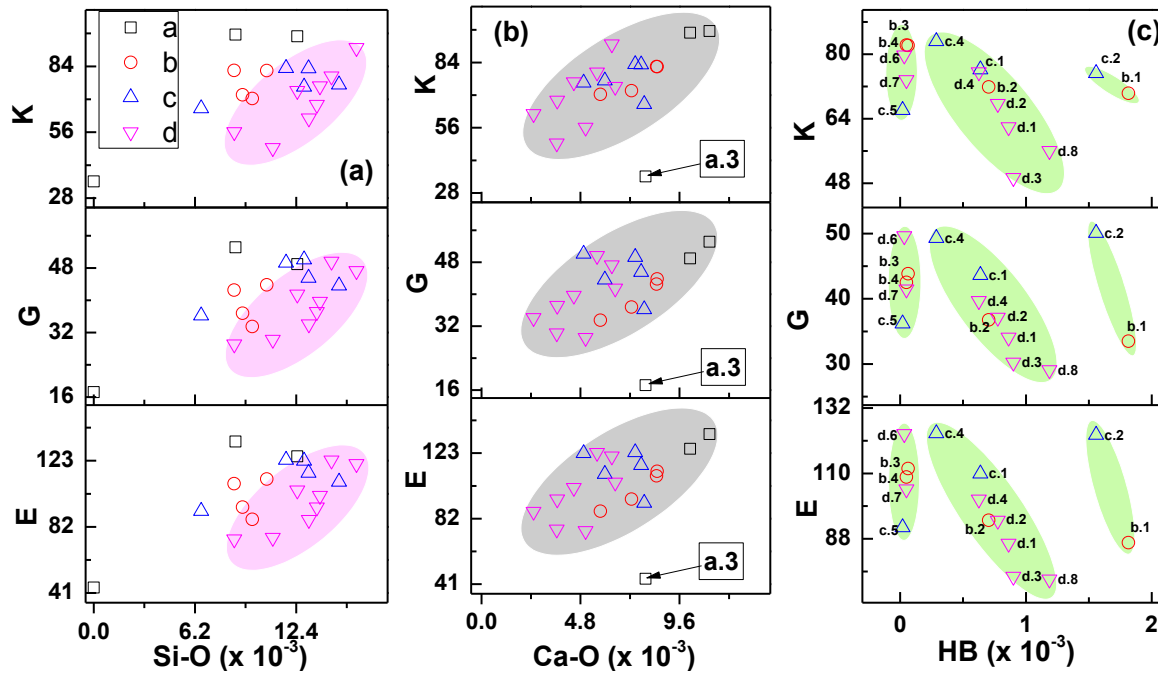


Figure 16. Distribution of mechanical parameters K, G and E (GPa) as a function of PBOD of: a) Si-O, b) Ca-O and c) HBs. Different symbols designate four different groups of crystals: a (open square), b (red circle), c (blue triangle up), and d (pink triangle down).

In contrast with the relationship of the PBOD with mechanical properties, the relationship of the K, G, and E values vs the atomic percentage is quite different. The CSH crystals are made up of CaO, SiO₂ and H₂O. The best way is to represent the composition is in terms of the percentages of elements. i.e. Ca%, Si% and H% which include both OH and H₂O. The calculated mechanical properties as a function of Ca%, Si% and H% are shown in **Figure 17**. As before, different colors and shape of symbols designate each Strunz group (see **Table 8**). This type of analysis is important because atomic percentages are readily measurable quantities. **Figure 17 (a)** reveals that there is an approximately linear correlation with the Si atomic percentage which is related to the number of Si atoms irrespective of its local geometry. **Figure 17 (b)** for Ca atomic percentage reveals the usual correlation with the number of Ca atoms which is the basis of using C/S ratio as the common parameter in assessing C-S-H materials. **Figure 17 (c)** appears to have weak negative correlations with H atomic percentage. However, such correlations do not distinguish the H from H₂O or OH group. They do not show any meaningful correlation when separately plotted see (**Figure 18**).

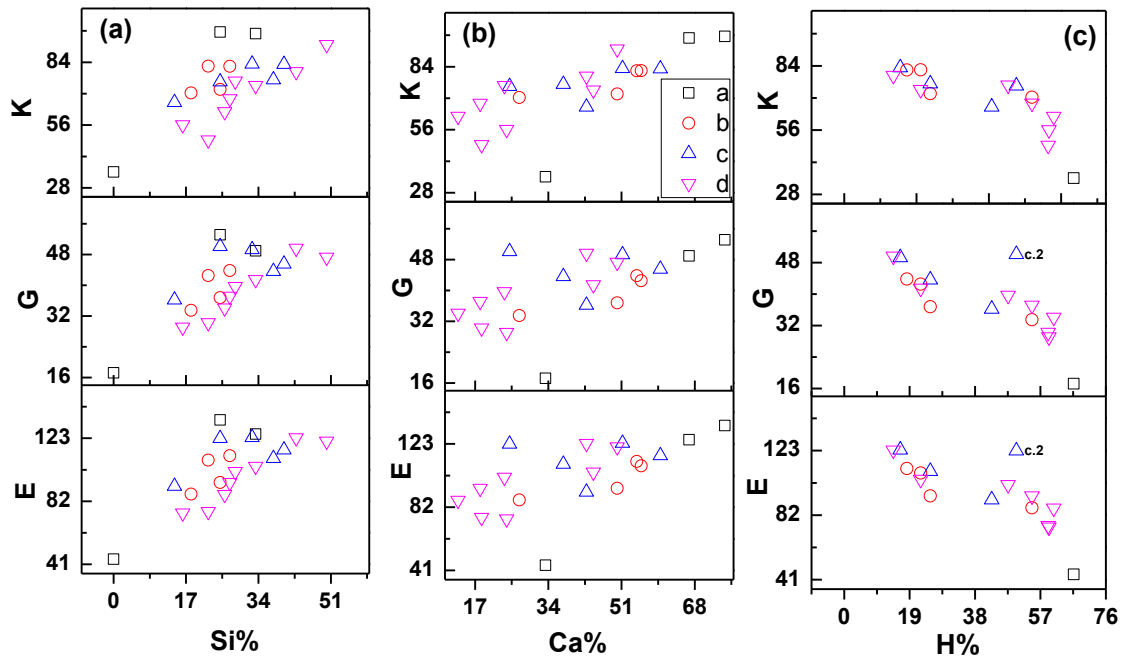


Figure 17. Distribution of K, G and E as a function of atomic percentage of (a) Si, (b) Ca and (c) H.

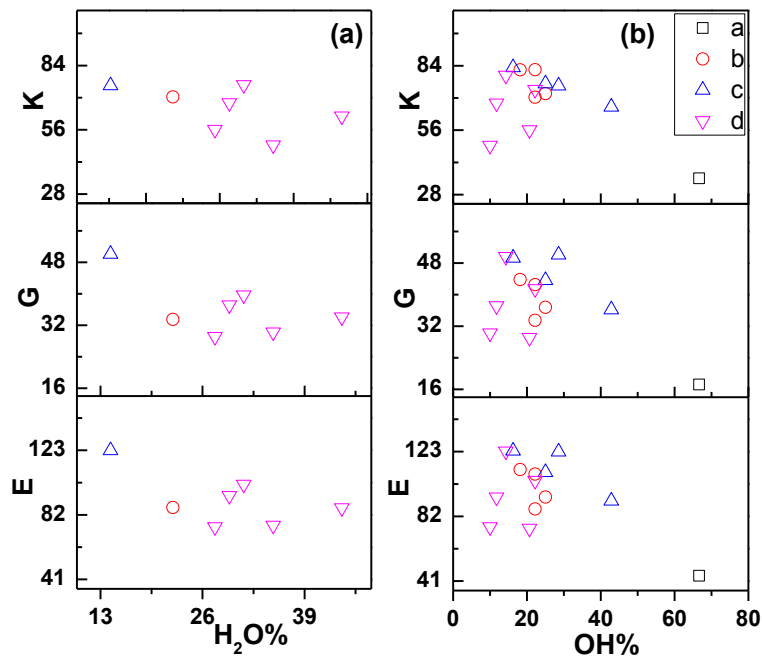


Figure 18. Distribution of K, G and E as a function of percentage of (a) H₂O and (b) OH.

Traditionally C/S ratio has been the main parameter to characterize the mechanical properties of cement paste ⁹⁶. However, it shows contradictory trends in different experiments by different authors. Plassard *et. al.* ⁹⁵ and Contantinides *et. al.* ⁸⁸ used nano-indentation and showed that the elastic modulus of C-S-H increase with C/S ratio. Their results show some differences that were attributed to the nature of the samples used. The former used single C-S-H gel derived from synthetic C-S-H and the latter used the network C-S-H derived from Portland cement paste. In contrast, Alizadeh *et. al.* ⁹⁷ using dynamic mechanical analysis (DMA) observed the exact opposite trend for synthetic C-S-H formed by hydrating ordinary Portland cement (OPC). Thus a systematic study of CSH single crystals is useful to shed light on these conflicting results. Present study has searched for trends in three possible ratios in CSH: C/S, H/S and C/H. Study found no correlation of mechanical properties with the C/S and C/H ratio **Figure 19 (a)**. However, **Figure 19 (b)** shows a near inverse correlation of the mechanical property with H/S ratio. This relation is quite intuitive in the sense that higher degree of hydration increases the effective volume and lowers the density. This in turn reduces the bulk mechanical properties. Here, H includes both from OH group or water in the sense of the vaguely defined term of “effective water” ⁹⁰. The H/S ratio can be thought of as the ratio of degree of hydration to the degree of polymerization. From **Figure 19 (a)** it can be seen that H/S ratio is much better parameter to characterize CSH than the traditional C/S ratio.

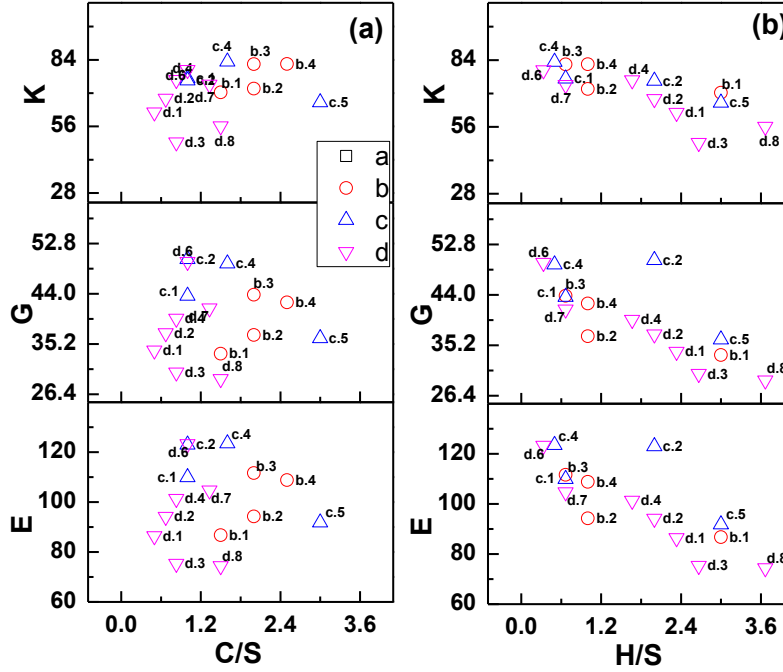


Figure 19. Bulk mechanical properties as a function of (a) C/S ratio and (c) H/S ratio.

5.3.4 Role of hydrogen bonding in controlling the mechanical properties

The unusual behavior with respect to the HBs stems from the complex structures in CSH as well as the variety of HBs formed that warrants an in-depth analysis. In this regard, it is possible to classify HBs in CSH into different types based on their local geometry and extend the analysis to include the possibilities of HB with next nearest neighbor (NNN). This study commenced by identifying four different local structural units for oxygen and hydrogen depicted in **Figure 20 (a)** as **T** (tetrahedron SiO_4), **TH** (SiO_4 with hydroxyl), **W** (water), and **CH** (Ca bonded hydroxyl) respectively. For H atoms, only **TH**, **W**, **CH** are relevant. Considering all possible combinations of these four structural units, there are 12 distinctively different types of HBs (indicated by "...") as shown in **Figure 20 (b)** and are respectively named as follows: 1) $\text{T} \cdots \text{TH}$, 2) $\text{T} \cdots \text{W}$, 3) $\text{T} \cdots \text{CH}$, 4)

TH...TH, 5) TH...W, 6) TH...CH, 7) W...TH, 8) W...W, 9) W...CH, 10) CH...TH, 11) CH...W, 12) CH...CH. By distinguishing these 12 types, it is possible to trace which of the 12 possible types of HBs are most relevant for their role in CSH crystal cohesion. **Figure 20 (c)** shows the scattered plot of BO vs. BL for all HBs in 15 hydrated CSH crystals that have HBs (open symbols with different colors for different types of HBs). For comparison, it was also shown in **Figure 20 (c)** the Ca-O bonds (green open star). The pie chart in the inset shows the percentage of HB-BOD for different types of hydrogen bonding. The top three contributors are 1) T...TH, 2) T...W and 8) W...W with 39.4%, 38.1%, and 15.2% respectively. A detailed inspection reveals that Type 4 (TH-TH), Type 5 (TH...W), Type 6 (TH...CH) and Type 10 (CH...TH) do not present in all CSH crystals. This is because these structural units do not occur in close proximity for HBs to be formed. Given the relatively large collection of 15 hydrated CSH crystals, it is expected that all conceivable HB environments in non-crystalline C-S-H gel are fully represented. The most common HB is the Type 2 (T...W) which involves W (water) unit, and they spread rather evenly in BO and BL. It should be stressed that this HB is between an O covalently bonded to a Si in T and an H in water which is very different from say type 7 (W...TH) which is between an O in water and H attached to TH. The HBs that has CaOH (Unit CH) such as Type 3(T...CH), Type 9 (W...CH), Type 11(CH-W) and Type 12 (CH-CH) are relatively weak compared to other HBs. For example, Type12 (CH...CH) have BO values less than 0.0071 whereas Type 8 (W...W) between two water molecules have relatively higher BO (≤ 0.0608). It is also noteworthy to observe in **Figure 20 (c)** that the Ca-O bonds, which have comparable BO values as the HBs, have much larger BLs.

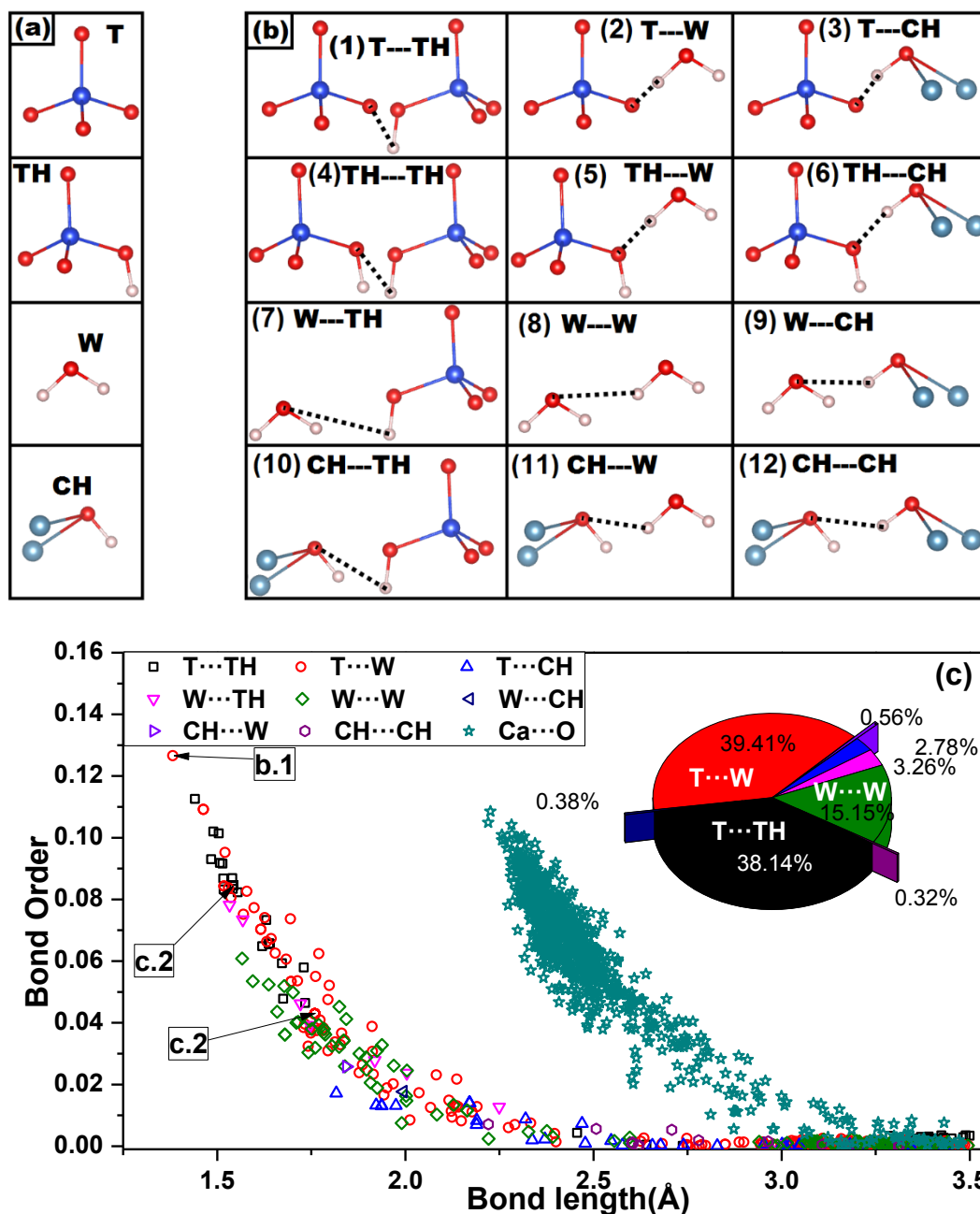


Figure 20. (a) Four different structural units: T (SiO₄ tetrahedron), TH (SiO₄-H), W (H₂O), CH (2Ca-O-H) of local environment for oxygen (T, TH, W and CH) and H (TH, W) in CSH. (b) 12 different types of hydrogen bonding between the four units in (a): (1) T-TH, (2) T-W, (3) T-CH, (4) TH-TH, (5) TH-W, (6) TH-CH, (7) W-TH, (8) W-W, (9) W-CH, (10) CH-TH, (11) CH-W, (12) CH-CH. (c) BO vs. BL distribution for HB and Ca-O bonds in 15 hydrated CSH crystals. Different types of HBs are labeled with different color and symbols. The inset pie chart shows the percentage BO for different types of hydrogen bonding. Specific BO for suolunite (c.2) and the highest BO from afwillite (b.1) are indicated by arrows.

It is not found in literature a study on any quantitative HB analysis as shown above for complex materials systems such as CSH. Thus, insight gathered is extremely valuable in constructing viable model for C-S-H gel. The main observations for this analysis are as follows: (1) the bond strength of HBs represented by the BO can be of the same order as Ca-O bonds in CSH crystals, and (2) certain types of HBs have significant contribution to the overall cohesion of CSH crystal which could be beneficial for cement gel. Close inspection of the structure of mineral Suolunite (c.2), which has a high contribution of HB-BOD and outstanding mechanical parameters (see **Table 8**), shows that silicate dimers in Suolunite are interconnected with a network of HBs that originate from OH groups ⁷³. The HBs that originate from water, although fairly strong, are localized to the dimeric silicate chain. This extraordinary network of HBs is responsible for its conspicuous mechanical properties. The crystal afwillite (b.1) has monomeric silicate chains and also a connected network of HBs originating from water and hydroxyls with equal percentage (22.2% each) of water and hydroxyls. However, its mechanical moduli are smaller than Suolunite (c.2) but comparable to other CSH crystals such as jennite (d.8), even though it has higher degree of hydration. Suolunite (c.2) has two types of distinctive HBs with BO of 0.085 (type 1, T···TH) and 0.044 (type 2, T···W) whilst afwillite (b.1) involve many different types of HB except types 3, 9, 11 and 12, with BO values ranging from highest (0.128) to a lower value (~0.04) as marked in **Figure 20 (c)**. This attests to the fact that an in-depth analysis at the atomistic scale structure and bonding is absolutely necessary to understand the complex cement chemistry and properties. Most of all, HB plays a significant role in determining the mechanical properties of CSH crystals. The whole structural-property complexity seen

in CSH crystals and in Portland cement gel in general could be traced to the intricate interplay of the HBs and its local structures.

To further dissect the effect of H bonding, it is necessary to return to the distribution map of HB-BOD in CSH crystals with respect to the C:S:H (H in H₂O and OH) ratio in a ternary diagram shown in **Figure 15(a)**. It has a maximum at the location close to suolunite (c.2) and afwillite (b.1), indicating that the most ideal ratio for C:S:H to be 1:1:1 as in suolunite $\text{Ca}_2[(\text{Si}_2\text{O}_7)(\text{OH})_2]\text{H}_2\text{O}$. The plots in **Figure 15** on mechanical properties show that CSH have higher values for larger Ca concentration, smaller Si concentration and close to zero H concentration. Although it appears to favor the use of C/S ratio as a useful parameter in characterizing the mechanical properties of CSH gel, it completely ignores the fact that CSH crystals contain H atoms and the role of HB must be properly accounted for. The attempt to relate mechanical properties to atomic composition could be overly simplistic as shown by the different correlations of K, G, and E values vs the atomic percentage and with the HB-BOD for Si, Ca, and H. The approximate linear correlation with the atomic percentage is a poor indicator of the internal cohesion and merely appears to state that as the materials tends towards either predominantly silicon based or calcium based compound it is likely to have better mechanical properties. The ternary plots in **Figure 15** demonstrate that for CSH crystals there can be an optimum composition based on the quantum mechanically derived HB-BOD which includes different types of HB and can accurately accounts for internal crystal cohesion. Suolunite (c.2) is the only known CSH crystal which has a $\text{CaO}:\text{SiO}_2:\text{H}_2\text{O}$ ratio of 1:1:1 and an orthorhombic crystal symmetry⁸¹. This can be an

optimum composition for mechanically superior cement and in turn a much better construction material.

5.4 Conclusion

The present study focuses upon the correlations between mechanical properties and electronic structure based upon TBOD and PBOD for each bond species in CSH crystals. The results indicate SiO-BOD has no direct correlation which is counterintuitive and against conventional wisdom. That is because silicate tetrahedral units (in chains) are tightly bound units that provide overall rigidity but not necessarily account for the variation of mechanical properties in different CSH crystals. The variations are determined more precisely by the overall atomic and electronic structure dictated by the Ca-O bonds and HBs. This is seen from a positive correlation with CaO-BOD indicating the presence of Ca have a significant bearing on the mechanical properties of CSH crystals. Most importantly, there is a multifaceted balance between different types of interatomic bonds and the HB in controlling mechanical properties. In certain crystals such as suolunite, the HB network is organized in such a unique way that enhances its mechanical properties. This approach and findings can serve as a broad roadmap for developing next generation cements.

CHAPTER 6

ELECTRONIC STRUCTURE OF C-(A)-S-H (I) PHASE: THE RICHARDSON-2014 MODELS

6.1 Introduction

As the most used construction material of human civilization, concrete has endured intense research effort for more than a century ⁴. C-S-H, or commonly known as the cement gel or hardened cement paste; is the main binding phase of concrete that is responsible for its unique mechanical properties. Thus, improvement of cement gel entails a significant environmental, social, and economic impact. Unlike most material, unraveling the structure at atomic or even micro level of C-A-S-H (A = Aluminum is the main substituent of Si) had proven to be a difficult task due to the nature the material ^{38-39, 49b}. C-S-H is virtually X-ray amorphous, compositionally variable, and structurally highly inhomogeneous. The problem is further complicated as cement is finely intermixed with other phases and impurities. So far no synthesis technique is capable of making pure single phase C-S-H but many researches have proposed clever techniques to minimize the inhomogeneity ^{4, 38, 98}. However, even small changes in the synthesis techniques, the crystallinity of single phase synthetic C-S-H varies considerably ¹⁶. Most popular parameter usually used in characterizing cement Ca/Si molar ration is denoted as C/S ratio. Synthetic C-S-H preparations varies considerably from very poor X-ray diffraction patterns that are similar to most commercial cement pasts to highly ordered diffraction patterns. The latter is divided in to two groups, C-S-H (I) for phases corresponding to $C/S < 1.4$ and C-S-H (II) for higher C/S ratios ⁹⁹. C-S-H

(I) is believed to be a structurally imperfect form of Tobermorite 14A ¹⁰⁰, and C-S-H (II) is similar to Jennite ⁹⁹. On a side, this study use cement chemist's notation which denote that C-S-H is both structurally and compositionally inhomogeneous phase with crystalline and/or amorphous structure.

A major substituent in C-S-H is Al and many studies have found the pathways possible to substitute Si with Al ¹⁰¹. Thus, an atomistic model must consider C-A-S-H as well as C-S-H to comprehensively describe the nature of cement at atomic scale. Though dozens of models for C-S-H has been proposed ⁷, a structurally and chemically plausible model that describes experimental observations is not available so far. Models proposed so far are based on structural and chemical similarities to the class of crystalline minerals known as Tobomorite and Jennite ⁷. But, within this family of minerals there are many variations in crystal structure. A detailed account of the models proposed for cement is stated in **Chapter 5** in this thesis.

A recent review by I. G. Richardson proposed 16 C-S-H (I) models based on crystal-chemical and geometrical reasoning and show consistency with the experimental observations for synthetic C-S-H (I) and crystalline minerals ¹⁶. Moreover, this review proposes chemical formula (**formula 3** of Richardson review [16]) for generating structural models with varying chain length, basal spacing...etc. The 16 crystal structures proposed show which types of structures are plausible and which structures are not, as a possible C-S-H (I) model. The review also gives guidelines to extend the C-S-H (I) models to build C-A-S-H (I) models. This further provides mechanisms for making more models using the given structures as templates. However, the proposed structures are purely C-S-H (I) phases. In order to build C-A-S-

H (I), certain alterations such as properly placing protons or Ca^{2+} for charge balancing are necessary. Therefore, a computational study is more suitable for building C-A-S-H (I) models. This study thus intends to first and foremost optimize a selected C-S-H (I) models proposed in Richardson review ¹⁶, and secondly build C-A-S-H (I) phases of those selected models. The study intends to go further to calculate electronic structure and bonding properties of Richardson-2014 models for further validation and also building viable alumino-silicate [C-A-S-H (I)] phases. The outline of this study is as follows. Next section, describes the methods used for the simulation and details of computation. Section 6.3, discuss about the basis for the proposed Richardson-2014 models ¹⁶ and making C-A-S-H (I) phase. Then a discussion and interpretation on electronic structure, bonding and interlayer cohesion of the selected phases are presented. Section 6.4 presents a summery and conclusion of this study.

6.2 Computational modeling details

The technical details of VASP relaxations (see section 2.3.1) for all crystal structures in this work are briefly outlined as follows: (1) The PAW-PBE potentials ^{30, 50} were used with the generalized gradient approximation (GGA); (2) electronic convergence criterion set at 10^{-6} eV; (3) the force convergence criteria set at 10^{-5} eV/Å for ionic relaxation; (4) a high energy cutoff of 550 eV is adopted with tests using 600 eV cutoff showing no discernible difference. (5) The *k*-point-meshes used are 2x3x1. The electronic structure and bond order (BO) and total bond order density (TBOD) calculations were carried out using the OLCAO method as discussed in section 2.2.

6.3 Results and discussion

This section outlines the results from data analysis and discussion of the outcome. First the Richardson-2014 models are discussed in comparison to the past experimental work. The crystal-chemical details and the overall chemical formula to build the class of structures to generate plausible C-S-H (I) structure are discussed. From this database, the models **Tinf_14sc** and **Tinf_sc_noCa_LS1** were chosen as a stepping stone to understand the electronic structure of the C-S-H (I) phase. Then the strategy of extending the structure to build C-A-S-H (I) phases are presented. Thereafter, electronic structure results of these two models and the respective aluminosilicate phases are presented. Finally, the bonding of the C-(A)-S-H (I) phase is summarized and main conclusions are drawn.

6.3.1 A realistic C-(A)-S-H (I) models: The Richardson-2014 models

In building realistic models, previous models as well as the specific synthesis procedure on what those models based on needs careful consideration. Richardson¹⁶ considered all major experimental work such as XRD and NMR spectroscopy and others up to date on the synthetic C-S-H (I) phases as well as the C-A-S-H (I) phases as a basis for the proposed Richardson-2014 models. The preparation of high quality C-S-H (I) samples are described in ref.¹⁶. A summary of the main findings from the early work pioneered by Taylor¹⁰², Richardson⁴ and many other investigations^{100a, 103,62b, 104} are compiled in Richardson review¹⁶. C-S-H (I) is structurally imperfect tobermorite with different basal spacing is one conclusion drawn in those work. The basal spacing is found to depend both on the C/S and H/S ratios. However, one needs to consider the

results from these studies has considerable scatter (see Figure 1 of Richardson review¹⁶) due to the specifics of the experimental conditions and the details of the characterization technique such as drying experiments which affect the parameters such as C/S, basal spacing and H/S ratio. A detailed account of the experimental data and the interpretation is given in Figure 1 of Richardson's review¹⁶.

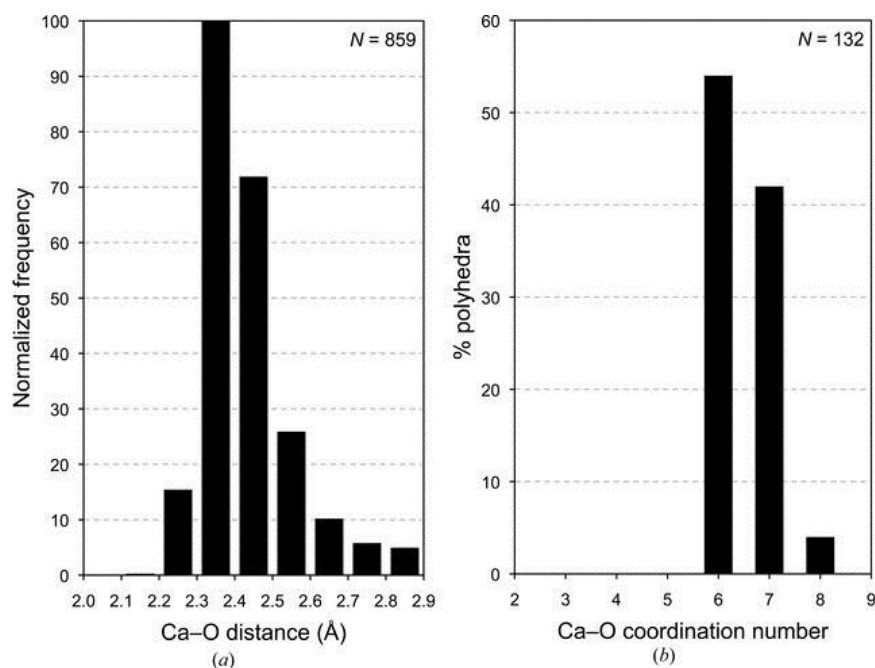


Figure 21. (a) Normalized frequency histogram for the Ca—O distances that are present in the crystal structures of 35 crystalline calcium silicate hydrates and related phases. (b) Histogram that shows the percentage of the Ca atoms in these phases that are coordinated to different numbers of O atoms. (see ref.¹⁶ and references there in)

The experimental data for synthetic C-S-H (I) phases for many parameters are scattered due to the inherent experimental difficulties mentioned earlier. However, there are 35 CSH crystalline minerals¹⁶ and thus, analysis of the structural motifs will help gain much needed insights into the C-S-H (I) phases. The Richardson-2014 models rely

heavily on the knowledge of the Ca polyhedra gained from the 35 known CSH crystals (see Figure 21). Chapter 4 shows the importance of a systematic study of the known crystalline structures to gain the electronic structure as well. Thus knowledge gained in Chapter 4 for a large subset of CSH of crystals is important to validate the Richardson-2014 models derived following a similar philosophy. The detailed account of the Ca polyhedra structure of these 35 CSH crystal minerals presented in the **Figure 21 (a), (b)**. Previous work of Dharmawardhana et al ^{25e} consisting 20 CSH minerals can be directly compared with results in **Figure 21**. The main purpose is to compare and contrast the structural features of the experimentally measured data against the VASP relaxed data within DFT. This will highlight the differences in BL and BA as well as the optimized hydrogen positions which may have impact upon the conclusions.

C-S-H (I) is a structurally imperfect form of tobermorite which mainly has 14, 11 and 9 Å basal spacing. However, it is believed that intermediate values can occur based on the broad basal peak visible in the XRD spectra. The main candidate T11 Å, comes in two forms. One having an orthorhombic (**ortho**-tobermorite) form and second one having a monoclinic (**clino**-tobermorite) form subcell ⁴. Approximate parameters for the orthorhombic subcell have been reported as: $a = 5.65$, $b = 3.66$, $c = 22.6 \text{ Å}$ ¹⁰⁵, space group $Imm2$ ^{47a, 51b}. Those parameters for the monoclinic subcell is reported as: $a = 5.593$, $b = 3.645$, $c = 22.456 \text{ Å}$, $\beta = 96.97^\circ$, space group $I2/m$ ¹⁰⁶. The structures in both families consist of layers of Ca-O polyhedra that have silicate chains clasped to each side that are kinked to produce a repeat of three tetrahedra chain per unit cell. The silicate tetrahedra that are closest to the Ca-O sheet are called paired tetrahedra (abbreviated as 'PT'), and those that are further away are called bridging tetrahedra

(BT). A schematic representation of these tetrahedra is given in **Figure 22**. The BT of adjacent layers shares an O atom forming double chains that run parallel to **b**-direction. The double chains in 11Å orthotobermorite display $2mm$ symmetry compared with $2/m$ symmetry in 11 Å clinotobermorite ¹⁰⁷. The individual layers in 14 Å tobermorite are too far apart to be linked, thus is a single-chain. The BT of adjacent layers are staggered with respect to one another with a corresponding shift of $b/2$ among the silicate chains ¹⁰⁷. Additional interlayer water molecules are present in the expanded interlayer.

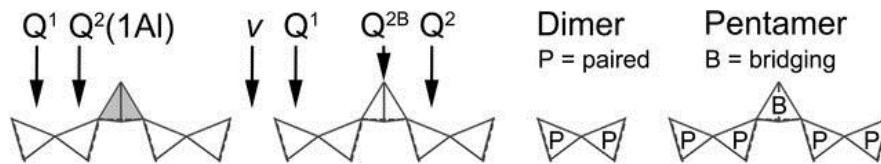


Figure 22. Representation of **BT**, **PT** and **v** (vacant) sites. The **Qⁿ** notation is NMR terminology.

All the models that include infinite silicate chains proposed by Richardson ¹⁶ follow the above explained crystal structures as a seed model. These are considered as best starting model for building a realistic C-S-H (I) phase model. Number of work has used the above crystal structures as a starting model for whole pattern or Rietveld-type refinements ^{108, 109, 110} to build C-S-H (I) models for specific research objectives. The main drawback of these studies is not refining the atomic positions due to lack of diffraction data. Thus, the refinements were limited to lattice parameters, site occupancies and other bulk data that limits the reliability of the proposed models. Richardson-2014 models refine the atomic positions as well by optimizing the c/z values for the simulated XRD patterns. Thus his models are much more realistic and give new

insights to the C-S-H (I) structure. The structural imperfections are included in the form of variable chain length by removal of bridging tetrahedra (BT) and addition of cations to charge balance the cell. The 16 structural models deposited in the supporting information of Richardson review ¹⁶ have the following naming criterion. Present study uses structures from this repository. The name of the datablock for each structure starts with 'T' to denote tobermorite-based structure; a number or 'inf' that denotes the mean length of the silicate chains; and an underscore. The rest of the datablock name can be understood using the following key: 11 or 14 = any infinite-chain part of the model structure has a layer spacing of approximately 11 or 14 Å; s = staggered; a = adjacent; o = *ortho*; c = *clino*; noCa = there are no interlayer Ca²⁺ ions; LS1 = the first of two alternative layer spacing; LS2 = the second of two alternative layer spacing. Present study also maintains the same naming convention.

Richardson-2014 models consist of T2, T3, T5 and Tinf models of the indicated silicate chain lengths. T2 and Tinf models are the end members of all possible models for C-S-H (I). It is also shown that the Si⁴⁺ substitution by Al³⁺ can only happen in the BT sites. Objective in this study is to extend the models to include the Al. Thus, Tinf models are the best models to choose for this purpose. This study limits to only Al substitution and refrain from adding **v** sites (**Figure 22**) as this require larger supercells. Ideally **v** sites are needed to be as close as to the cement gel. For every Si⁴⁺ → Al³⁺ substitution four-fold coordination is preserved and Ca²⁺ or proton must be appropriately placed closed to substituted BT site to compensate the charge. The chemical formula (1) in Richardson review ¹⁶ and others has to be considered to properly account for the partial occupancy and charge balancing of the cell. It is shown that clino-tobermorites with

staggered silicate chains are the best representation of C-S-H (I) that agrees well with experiments. Thus out of 7 Tinf models, two models were chosen, i.e. Tinf_14sc (**Figure 23**) and Tinf_sc_noCa_LS1 (**Figure 24**). The main differences of these two models are interlayer Ca^{2+} ions and partial occupancies. Tinf_14sc (**Figure 23 a**) has partial occupancies and Ca^{2+} ions in the interlayer region. Tinf_sc_noCa_LS1 (**Figure 24 a**) has neither partial occupancies nor Ca^{2+} ions in the interlayer region. These differences thus give an opportunity to investigate the effect of Ca^{2+} ions in the interlayer region. The partial occupancies are given in the supplementary material of the Richardson review ¹⁶. For example in the model Tinf_14sc, the water molecules Wat3 and Wat3A occupy the same position as the Ca3 and Ca3A atoms. The removal of atoms to obtain full occupancy is done in such a way that no two atoms occupy the same position and rest are removed to prevent large voids in the cell. VASP relaxation of the Tinf_14sc and Tinf_sc_noCa_LS1 models proved to be difficult as shown by the deviations in **Table 11**. A maximum deviation of 6.8% for β° is seen in Tinf_sc_noCa_LS1 model. The monoclinic symmetry is no longer preserved proving the necessity of the computational modeling for to validate Richardson-2014 models.

According to instruction of Richardson review ¹⁶, Al substitutions must only be done at BT sites to build C-A-S-H (I) models from the respective C-S-H (I) models. For Tinf_14sc charge balancing was done in two ways. First by adding Ca3A_1, and Ca3A_2 placed between Al2A_2, Al2A_4 and Al2A_1, Al2A_3 containing BT respectively (See **Figure 23 b**). Second by adding a proton to each free oxygen attached to Al2A_2, Al2A_4, Al2A_1 and Al2A_3 containing BT (See **Figure 23 c**). The C-A-S-H (I) models are aptly named for example Tinf_14sc+Al_model1 to signify the Al

substitution to Tinf_14sc. The H atoms for hydroxyl and water are added by hand and optimized using VASP. Favorability of substitutions is immediately known from the convergence of geometry and electronic structure. Many careful optimization techniques were necessary to build the C-A-S-H (I) phase. Care must be taken to remove the partial occupancies as the Ca^{2+} and the H_2O included for the purpose of charge balancing sometimes occupy the same position. A similar criterion was necessary to build the C-A-S-H model from Tinf_sc_noCa_LS1 model. However, the only option was to add Ca^{2+} (Ca3, Ca3A) as all BT in the cell are saturated with hydroxyl. Thus, only one C-A-S-H (I) model (**Figure 24 b**) was built from Tinf_sc_noCa_LS1. It must be noted here that VASP relaxation was difficult for all 5 models and quite a bit of deviation (11.2% for Tinf_sc_noCa_LS1+Al shown in **Figure 24 b**) can be seen for C-(A)-S-H (I) lattice parameters (**Table 11**) from initial structure. This show the Richardson-2014 models need to be relaxed before properties can be calculated and characterized. If mechanical property calculations are to be done for these models, further relaxation is necessary.

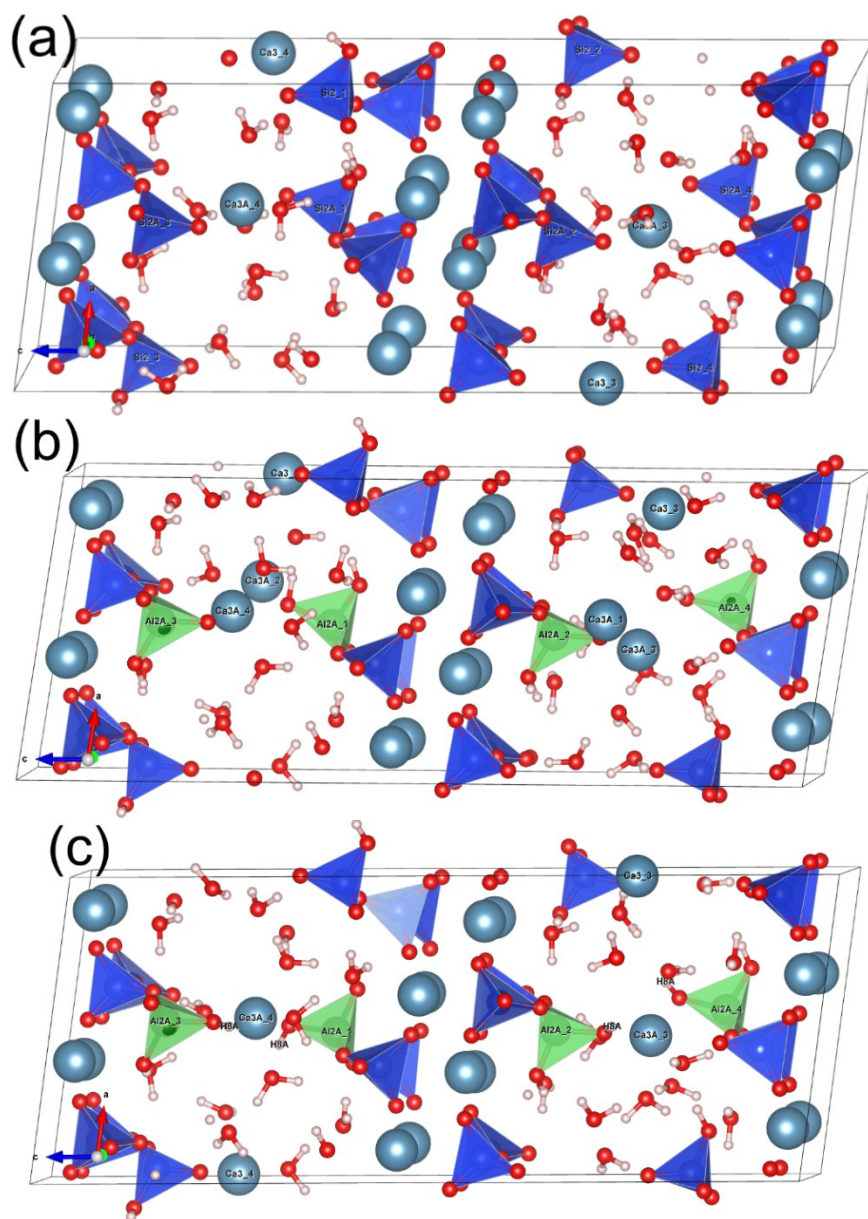


Figure 23. Ball&Stick diagrams of (a) Tinf_14sc (b) Tinf_14sc+Al_model1 and (c) Tinf_14sc+Al_model2.

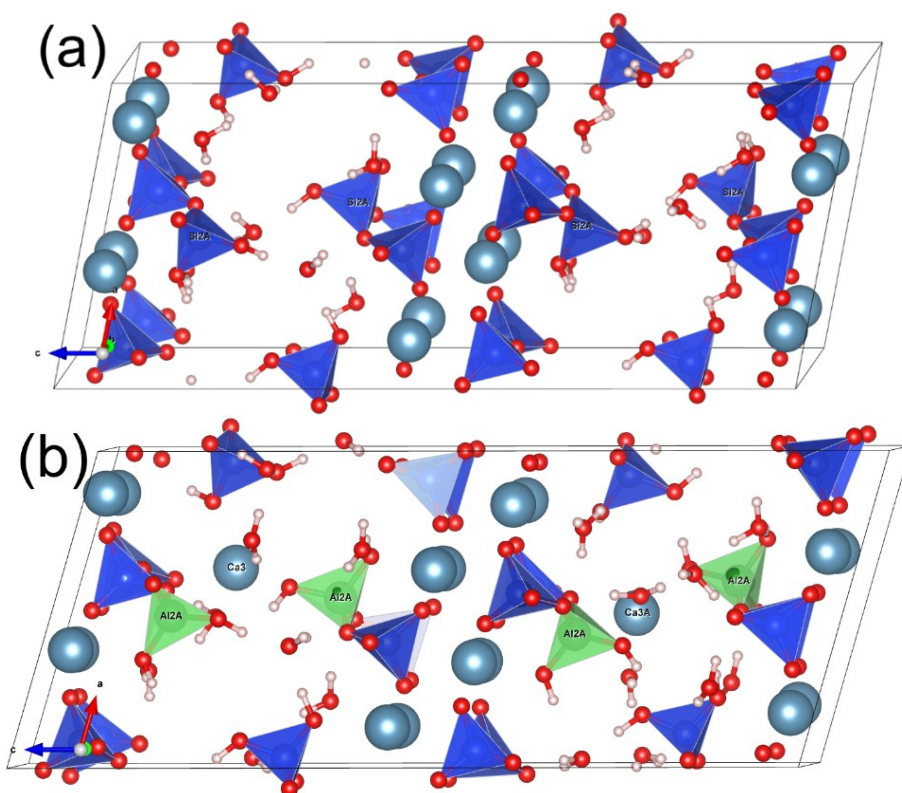


Figure 24. Ball&Stick diagrams of (a) Tinf_sc_noCa_LS1 and (b) Tinf_sc_noCa_LS1+Al.

Table 11. Reported/VASP relaxed lattice parameters and there % difference and lattice parameters for the proposed C-A-S-H phases.

| | Tinf_14sc | | | Tinf_sc_noCa_LS1 | | |
|----------------|---------------------|---------|---------------------|-------------------|---------------------|-------|
| | ref ¹⁶ | present | %diff | ref ¹⁶ | present | %diff |
| a (Å) | 11.350 | 11.294 | -0.5 | 11.35 | 11.35476 | 0.0 |
| b (Å) | 7.300 | 7.407 | 1.5 | 7.3 | 7.404177 | 1.4 |
| c (Å) | 28.800 | 28.423 | -1.3 | 26.715 | 26.70829 | 0.0 |
| α° | 90.000 | 90.394 | 0.4 | 90 | 91.0121 | 1.1 |
| β° | 95.500 | 98.252 | 2.9 | 95.5 | 101.9845 | 6.8 |
| γ° | 90.000 | 89.992 | 0.0 | 90 | 89.50042 | -0.6 |
| | Tinf_14sc+Al_model1 | | Tinf_14sc+Al_model2 | | Tinf_sc_noCa_LS1+Al | |
| | | | | | | |
| a (Å) | 11.300 | | 11.375 | | 11.276 | |
| b (Å) | 7.458 | | 7.459 | | 7.438 | |
| c (Å) | 28.981 | | 28.433 | | 27.134 | |
| α° | 91.990 | | 90.988 | | 94.037 | |
| β° | 98.777 | | 98.000 | | 106.235 | |
| γ° | 90.564 | | 90.768 | | 89.112 | |

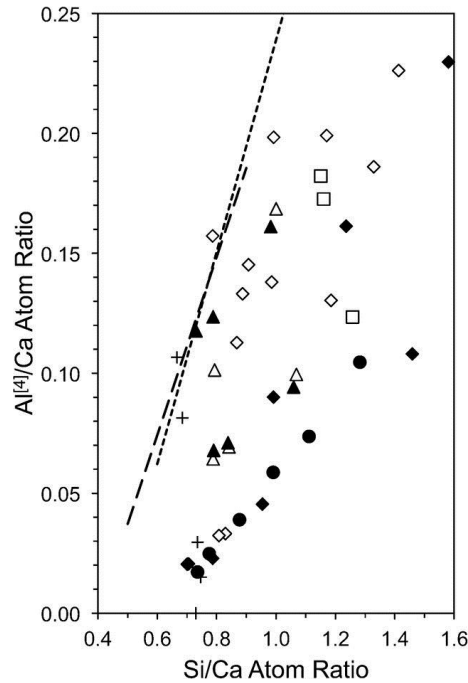


Figure 25. Degree of possible Al³⁺ substitutions in C-A-S-H (I) phases. (see ref ¹⁶ for experimental data and references).

The Al substitution, although the main impurity in C-S-H, there are compositional limitations according to experiments ^{111, 101}. It is found experimentally that there exists a maximum amount of Al for a given structure ^{111, 16, 101}. The possible Al³⁺ substitutions observed experimentally for C-A-S-H (I) phases are indicated in **Figure 25**. Collection of experimental data of the plot of Al/Ca vs Si/Ca ratios shows existent of maximum Al/Ca for a given Si/Ca. The upper bound is indicated by the dashed line. Thus, Al substitution in Richardson-2014 models to generate C-A-S-H phases must be done with care. For example in Tinf_14sc (See **Figure 23 a**) if all 8 BT sites (Si2/Si2A) are substituted by Al³⁺ the Al/Ca = 0.36 and Si/Ca = 0.73. According to **Figure 25**, this falls above the dashed line making it an unrealistic Al composition. This would render an implausible structure. Therefore, only 4 (See **Figure 23 b and c**) were substituted out of the 8

possible BT sites with Al. All three Al substituted models Tinf_14sc+Al_model1, Tinf_14sc+Al_model2, Tinf_sc_noCa_LS1+Al are according to **Figure 25** fall within the accepted range of experimental data and thus can be considered as realistic models.

6.3.2 Electronic structure of Richardson-2014 models

The electronic structure of the models discussed in Section 6.3.1 was calculated via OLCAO method (see Section 2.2). The TDOS and the element resolved PDOS are shown in **Figure 26** and **Figure 27** for the models Tinf_14sc and Tinf_sc_noCa_LS1 and their C-A-S-H (I) derivatives respectively. The DOS for Tinf_14sc (**Figure 26 a**) and Tinf_sc_noCa_LS1 (**Figure 27 a**) show very similar peak features. The core states are derived from Ca and O. The VB is dominated by O states. The CB has major contribution from the Ca. The energy range (-10 – 0) eV in the VB has some contribution from the Si and H. The main feature is similar to the T11, T14 DOS discussed in Section 3.3.2. This calculation is done at “level 0” in OLCAO with only 4/5 potential types. For further analysis on the different structural units such as silicate and water more potential types has to be added. This may be necessary as a future study to better understand the contribution from interlayer species such as Ca and H₂O. The PDOS of Al as shown in **Figure 26 b and c** and **Figure 27 b** shows that Al has only a minor contribution to the TDOS. This could be due to low composition of Al. However according to the experimental observation in **Figure 25**, models generated by this study contains reasonable amount of Al. Future study is necessary with larger supercell to better understand the effect of Al. There could be some affect from the fact that models in this study do not contain silicate vacant sites. Due to the limited computational

resources, such calculation which require larger supercell was not attempted at this time. However, the VASP optimized models obtained will be a good starting point to build bigger models which will allow understanding some of these issues.

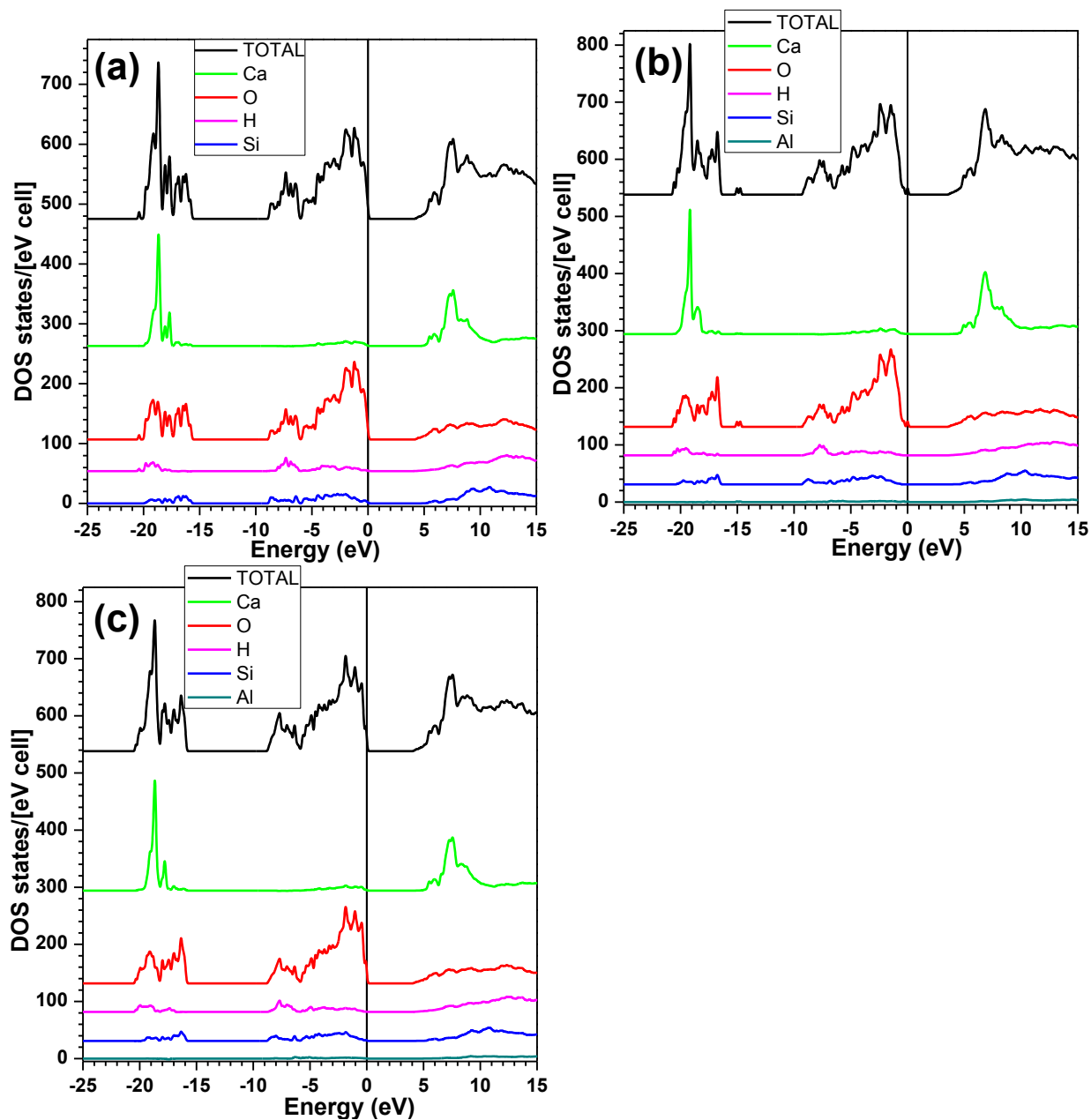


Figure 26. Total and partial DOS of (a) Tinf_14sc (b) Tinf_14sc+Al_model1 and (c) Tinf_14sc+Al_model2.

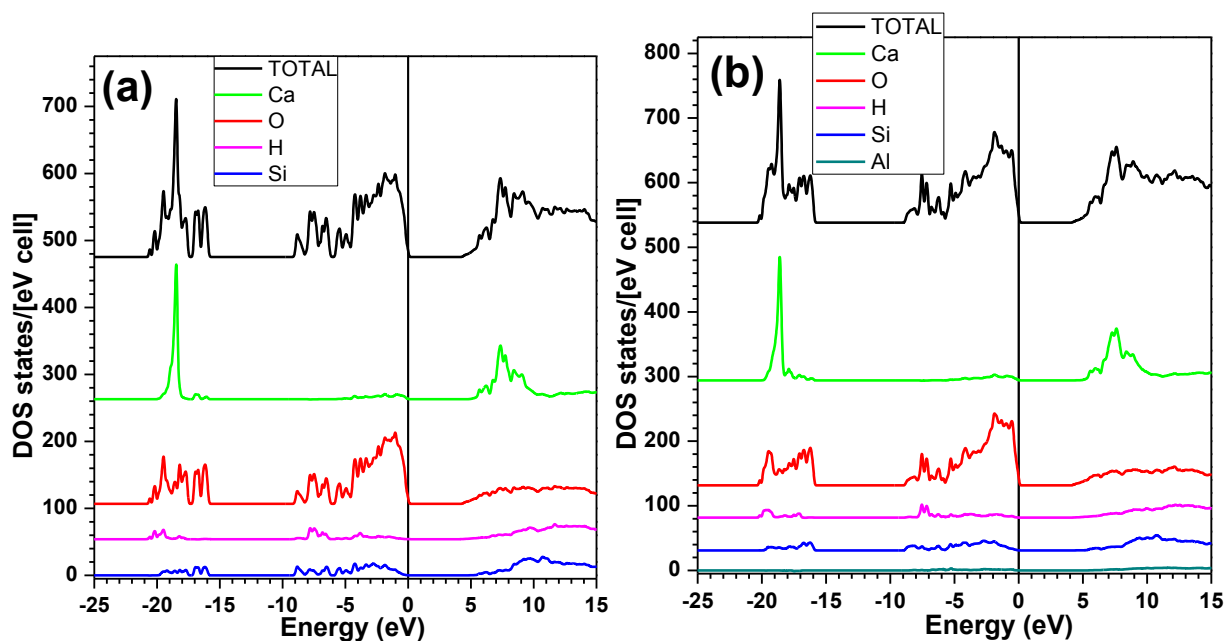


Figure 27. Total and partial DOS of (a) Tinf_sc_noCa_LS1 and (b) Tinf_sc_noCa_LS1+Al.

6.3.3 Bonding types of Richardson-2014 models

The most important feature of the OLCAO package is its ability to quantify the bonding via the Mulliken overlap population analysis (See Section 2.2). The use of this is elaborated in Chapter 3. The BO analysis is important to quantify the strength and cohesion of materials. In this regard the BO vs BL scatter plots have been instrumental in previous chapter for CSH crystals. **Figure 28** and **Figure 29** shows the BO vs BL scatter plots for Richardson-2014 models considered in this study. The pie charts in **Figure 28** and **Figure 29** give the percentage contribution from different types of bonds to the TBO thus, giving an overall representative picture of the distribution and relative strengths of different bond species. The TBOD values have been also shown in the **Figure 28** and **Figure 29** for each crystal respectively.

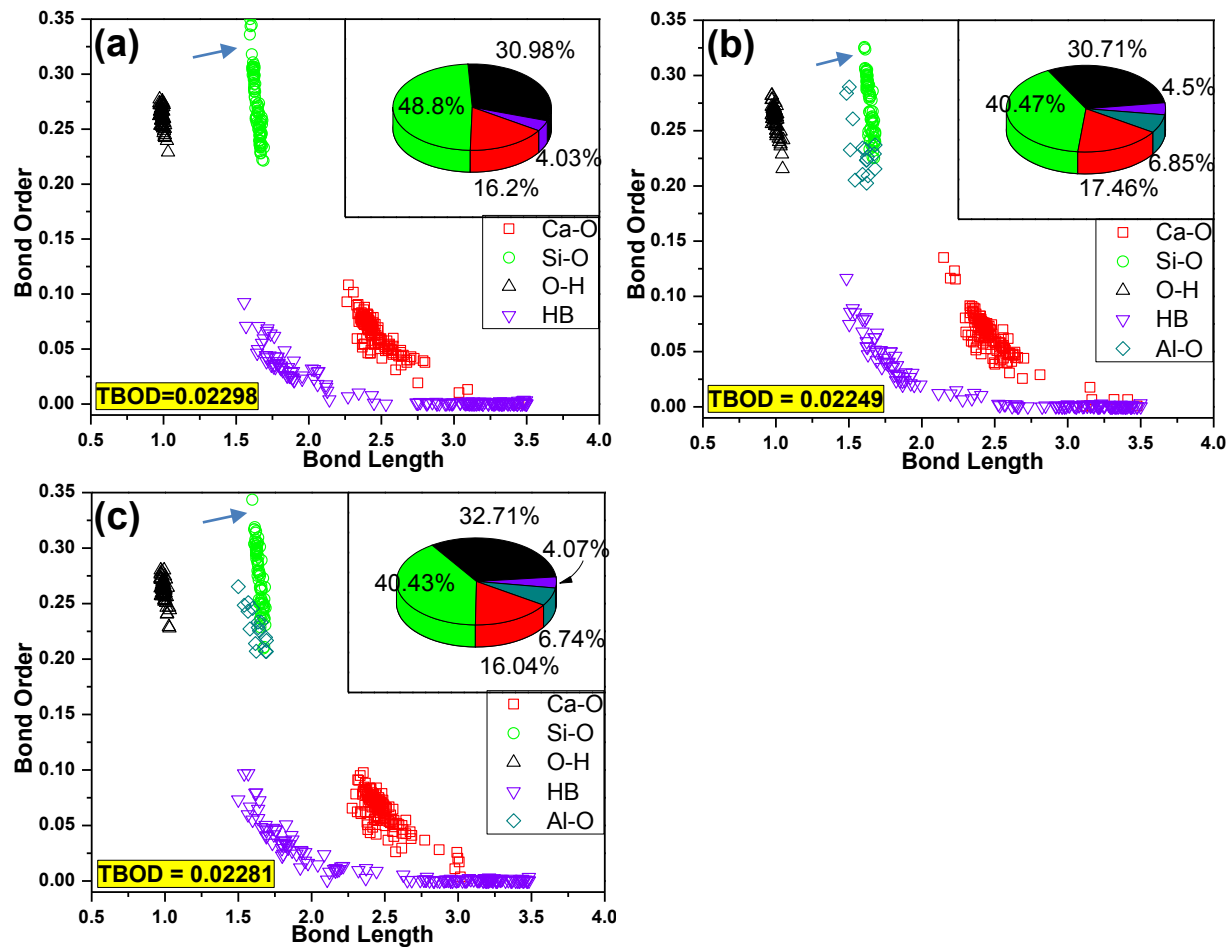


Figure 28. Bo vs BL scatter plot of (a) Tinf_14sc (b) Tinf_14sc+Al_model1 and (c) Tinf_14sc+Al_model2. The inset shows the pie chart of % contributions of bond types.

The BO distribution of Tinf_14sc model and the C-A-S-H (I) phases derived from it are shown in **Figure 28**. There are four major types of bonds, Ca-O, Si-O, O-H and HB for C-S-H model and Al-O in addition for the C-A-S-H (I) models. These distributions show typical distributions as seen in previous studies in section 4.5. Si-O and O-H covalent bonds have a rather narrow BL but a wide BO. For example Tinf_14sc+Al_model1 has narrow range for BL (1.5886, 1.6919) and wide range for BO

(0.2213, 0.3549) for the Si-O bonds. This may be useful information for spectroscopic characterization techniques to interpret data. For example, the “blue arrow” in the **Figure 28** shows a gap in the Si-O BO distribution. This was identified in **Chapter 4** as the different strength in Si-O bonds when a hydroxyl group connected to silicates. The Si-OH bonds are weaker than the Si-O bonds without the hydroxyl group.

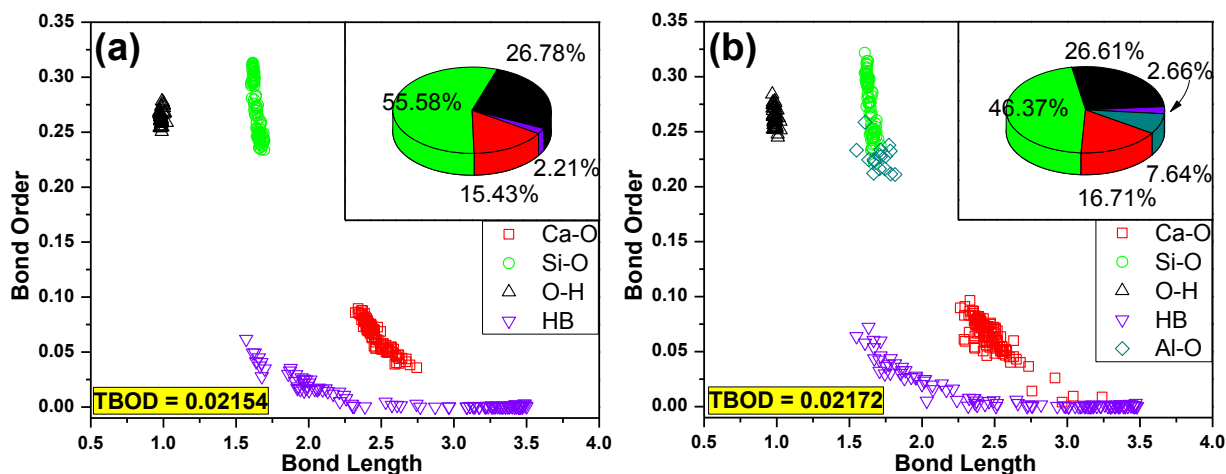


Figure 29. Bo vs BL scatter plot of (a) Tinf_sc_noCa_LS1 and (b) Tinf_sc_noCa_LS1+Al. The inset shows the pie chart of % contributions of bond types.

The Ca-O show similar distribution to T11A and T14A models in **Chapter 3**. Similar to the CSH crystals studies in **Chapter 4**, it shows a wide range of BO and BL distribution for the HBs. Tinf_14sc models have strong HBs as shown in **Figure 28**. The Tinf_sc_noCa_LS1 however, according to **Figure 29** HBs seems to be weaker. The maximum HB seen in Tinf_14sc+Al_model1 is 0.1164. The highest HB in Tinf_sc_noCa_LS1 is 0.0723. The differences among these models are the interlayer features. Tinf_14sc models have much higher Ca^{2+} ions than Tinf_sc_noCa_LS1

modes. Thus the number of Ca^{2+} in the interlayer region affect the HB network which in turn will affect the mechanical properties. The most important finding in this study is the bonding information for the C-A-S-H (I) phases. This information at *ab initio* level calculation has not been reported in literature so far. The proposed 3 C-A-S-H (I) models; Tinf_14sc+Al_model1, Tinf_14sc+Al_model2 and Tinf_sc_noCa_LS1+Al are published here for the first time. The Al substitution for Si increases the natural trivalent coordination of Al. From the scatter plot it is observed that Al-O bonds fall in the same region as the Si-O bonds. However, Al-O has wider BL in comparison to the Si-O bond distribution. For example Tinf_sc_noCa_LS1+Al has a BL range of (0.2111, 0.2586) from Al-O bonds.

The figures also contain the TBOD values for the 5 models discussed in this study. The maximum TBOD is for Tinf_14sc (0.02298) and the minimum is for Tinf_sc_noCa_LS1 (0.02154). Thus the former has much higher cohesion than the latter according to the proposed criteria in this **Chapter 4**. Thus, Ca^{2+} in the interlayer region will affect the cohesion of cement. It is also noticed that the TBOD values fall under the medium TBO range discussed in **Chapter 4**. The medium range TBO included most of the Tobemorite family of crystals and Jennite that are speculated to be the closest to the overall structure of cement gel.

6.4 Summary and conclusion

In summary, the study contains detailed electronic structure calculations using *ab initio* methods for realistic C-S-H (I) models (Tinf_14sc, Tinf_sc_noCa_LS1). With accurate structural optimization, these models were extended to include Al and

proposed for the first time possible C-A-S-H (I) phase models (Tinf_14sc+Al_model1, Tinf_14sc+Al_model2, Tinf_sc_noCa_LS1+Al). VASP optimization suggests the necessity of detailed *ab initio* study to validate Richardson-2014 models. Here, the type and distribution of bonds in C-S-H (I) and C-A-S-H (I) phases was found and compared to the electronic structure data from the CSH crystal database contained in **Chapter 4**. The Al-O bonds within the C-S-H matrix have a similar strength to the Si-O bonds. The HB distribution was found to be similar to the inosilicate family of CSH crystals discussed in **Chapter 5**. However, the Tinf_sc_noCa_LS1 model had weaker HBs comparatively. The implication of Ca^{2+} in the interlayer on the HB network was discussed. The models discussed in this study have medium range TBOD according to the metric discussed in the **Chapter 4**.

A comprehensive understanding of the C-S-H (I) structure may require an exploration of all the Richardson-2014 models. The models built and extended in this study is just an initial step. Richardson's review provides guidelines to extending the database via appropriate combinatorial changes to the provided structures. For example, models can be generated introducing **v** sites to Tinf models to generate T2, T3 and T5 models and possibly longer silicate chain lengths interpret NMR data found in literature properly. Generating C-A-S-H (I) models can be studied further as well. This study only considered the substitution to the Tinf models. To be more realistic **v** sites need to be introduced and more models with different Al composition need to be studied. A comprehensive analysis of the Richardson-2014 models, as several independent variables must be considered, may take several studies and large amount of computer resources. The most important incentive one must realize is that if a

comprehensive set of C-S-H (I) and C-A-S-H (I) models are generated it will be good starting structures to make C-S-H (II) and C-A-S-H (II) models via MD or MC methods. Only then one can realize a comprehensive understanding of the Portland cement gel.

Once a comprehensive set of models are generated from C-S-H (I) and C-A-S-H (I) as indicated in the paragraph above one can study the mechanical behavior of those models. This will allow understand the interesting mechanical properties of cement and hence concrete that has eluded scientist for centuries. It is an advantage that this change in paradigm will provide a much more reliable means in identifying the structure; composition and properties of C-(A)S-H in hardened cement. This fundamental insight on cements might provide ways to engineer new materials with suitable additives, such as polymers that can alter the interlayer HB's, in constructing more durable cements.

CHAPTER 7

TEMPERATURE DEPENDENT MECHANICAL PROPERTIES OF MO-SI-B COMPOUNDS VIA *AB-INITIO* MOLECULAR DYNAMICS

7.1 Introduction

Rapid development of technology is in constant pursuit of advanced materials with higher efficiency and durability. In the areas such as power generation and aerospace, the traditional structural materials such as Ni-based super-alloys have reached their physical limits in terms of their maximum operational condition such as temperature ($\sim 1200^{\circ}\text{C}$) which is already approaching 90% of its melting point¹⁷. By utilizing the high temperature coating and sophisticated cooling systems, the operating temperature can be increased only up to 1500°C at most¹⁷. The circumstance requires materials not only having a higher melting point but also considerable strength, stiffness and oxidation resistance at high temperatures as well as adequate mechanical behavior at room temperature¹¹². Hence the vigilant search for alternative materials has brought many researchers attention to Mo-Si-B class of alloys^{112a, 113}. Within this class of multiphase materials, the T1 (Mo_5Si_3) and T2 (Mo_5SiB_2) phases have shown high potential for the aforementioned applications by many recent studies^{112a, 114}. The T1 phase has very high melting point (2180°C) and excellent high temperature mechanical strength. The T2 phase also has excellent high temperature mechanical strength and good oxidation resistance¹¹⁵. Further, T2 phase has a higher creep resistance¹¹⁶ comparable to high-temperature ceramics^{114a}. The main drawback for the T1 phase however, is its high thermal expansion anisotropy (TEA) with the α_a/α_c ratio measured to

be as high as 2.0, resulting in high residual thermal stresses which consequently limits its structural applications ¹¹⁶⁻¹¹⁷.

Previous works on the mechanical properties at high temperatures for these two compounds have been limited to a modest ($\sim 1200^{\circ}\text{C}$) temperature range. These properties, especially the elastic tensor, are not easily accessible via experimental methods due to the difficulty in synthesizing and performing high temperature experiments on single crystal T1 and T2 phases ^{114a}. In this regards, *ab-initio* computational methods offer a viable alternative to obtain these critical properties. Numerous DFT-based *ab-initio* methods have been developed for this purpose using total energy approaches ¹¹⁸ stress-strain approaches ¹¹⁹ and density functional perturbation theory approaches ¹²⁰. Most of these methodologies work remarkably well for 0 Kelvin, but inadequate for higher temperature ¹²¹. The main objective of this study is to apply *ab-initio* molecular dynamics (AIMD) to access properties at high temperatures. AIMD method has become very popular as it encompasses, up to a greater extent, the accuracy of the DFT and ability to address high temperature ^{28, 122} properties. However, due to the demand for computational resources, typical AIMD calculations are only applied to systems in the order of a few hundreds of atoms at most ^{121-122, 123}. For Mo-Si-B system such a size is adequate owing to the relatively small number of atoms in the unit cell (32 atoms) and thus a 2x2x2 supercell of 256 atoms would be sufficient. Since the study does not consider off-stoichiometric models, the demand for the size of the supercell is comparatively less. Thus in this study, crystal structures were optimized with AIMD method for each temperature and used to extract high-temperature properties.

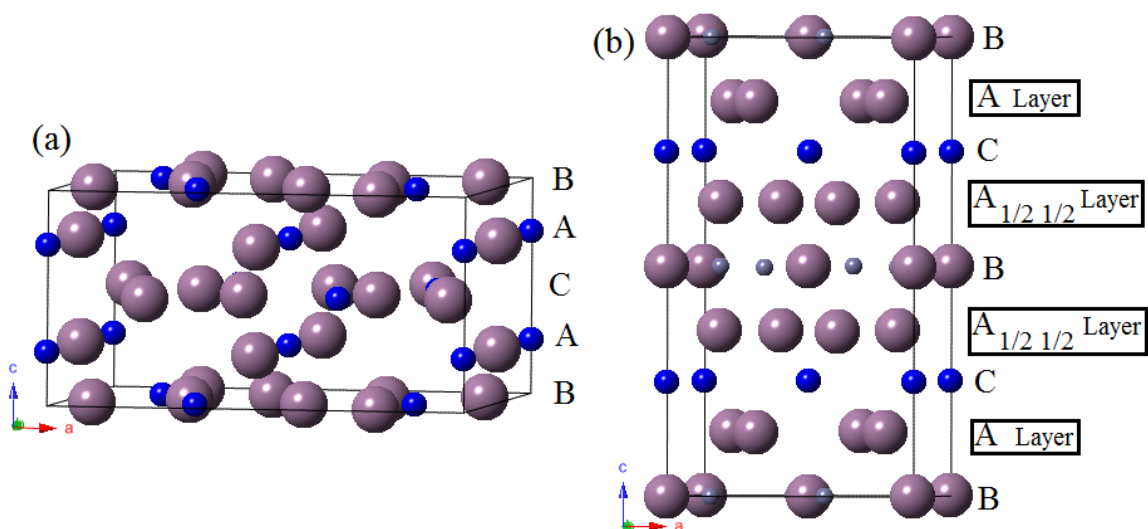


Figure 30. Unit cell of (a) T1 and (b) T2

Both the T1 and T2 phases have body-centered tetragonal structure. T1 forms in a W_5Si_3 type crystal with $D8_m$ space group symmetry. This crystal is stacked in a repetition of ABAC... layers along the c direction (**Figure 30 (a)**). The A- layers appear to have lower atom packing density than the B- and C- layers have Mo-Si bonds. However, the A layers are close enough to have Mo-Mo bonds through B- and C- layers. The B- layer is 180° rotated about the c axis. The T2 unit cell consists of 20 Mo (A type layers), 4 Si (B type layers) and 8 B atoms per cell. The C- layer however consists both of Mo and B atoms. The $A_{1/2 1/2}$ layer is similar to A- layer but shifted half of the diagonal of the unit cell. **Figure 30 (b)** clearly shows the four layer types.

7.2 AIMD method with in NVT ensemble

For all calculations it was used the Vienna *ab initio* simulation package (VASP)²⁸⁻²⁹. AIMD calculations in this study within NVT ensemble, used following parameters: (1) The PAW-PBE potentials^{30, 50} with the generalized gradient approximation (GGA); (2) electronic convergence criterion set at 10^{-4} eV; (3) MD time step of 2fs; (4) a high energy cutoff of 500 eV; an energy cutoff of 600 eV shows no discernible difference; (5) Γ point sampling was used.

Approach used by this study is to first use AIMD^{28, 122a} to get the equilibrium structure and lattice parameters at finite temperature. It was assumed that the structures obtained from AIMD embody all physical properties of the material at that temperature. Using the lattice parameters and atomic positions at respective temperatures, first-principles stress-strain method³⁴ was used to calculate the elastic tensor and the bulk elastic properties. It is essential in AIMD that the periodic supercell is sufficiently large to manage the fluctuations of thermodynamic variables, yet small enough to be computationally feasible¹²¹. For the two crystals (T1, T2), a 2x2x2 supercell (256 atoms) was generated for AIMD to extract the T dependence of the volume. The procedure was to systematically perform many NVT ensembles by varying (isotropic) the volume at each temperature so as to obtain equilibrium volume (V_0) at 1 atm (0.0001 GPa). Since T1 and T2 phases have a tetragonal crystal structure, it was initially assumed that a volumetric contraction/expansion with a constant c/a ratio to estimate V_0 close to targeted pressure and temperature. The study ensured the mean pressure and standard deviation of the mean was close to the targeted values. The data was then fitted to third-order Birch–Murnaghan isothermal equation of state¹²⁴ (BM-

EOS) to extract an initial estimate of the bulk modulus (K_0) and V_0 . Since the crystals are not isotropic, the c/a ratio for a given temperature needs to be further modified. The above procedure would only enable to provide a structure close to true V_0 at the targeted pressure. While this procedure gives the K_0 , it clearly deviates from the experimental trend as shown in **Figure 33 (b) and (c)**. This suggests that the estimated V_0 from the isotropic expansion is not close to the required equilibrium volume. Further analysis shows that although the total pressure on the supercell is close to the required value, the P_{xx} , P_{yy} and P_{zz} components vary considerably. This implies that the anisotropy ratio (c/a) has to be accounted for as well as the volume. Thus, it was subsequently evaluated the tensor components of the pressure varying the c/a ratio for the given V_0 to ensure that both the total pressure and its components are close to targeted value. After getting the equilibrium volume and c/a ratio for each temperature, a longer AIMD run of 4 ps is sufficient for convergence in pressure and temperature. The mean pressure ranged from 0.0005 to 0.2542 GPa and the standard deviation of the mean ranged from 0.0028 to 0.0138. The pressure fluctuations at each temperature for both crystals are shown in **Figure 31**. Test runs with 10 ps show no change in mean pressure.

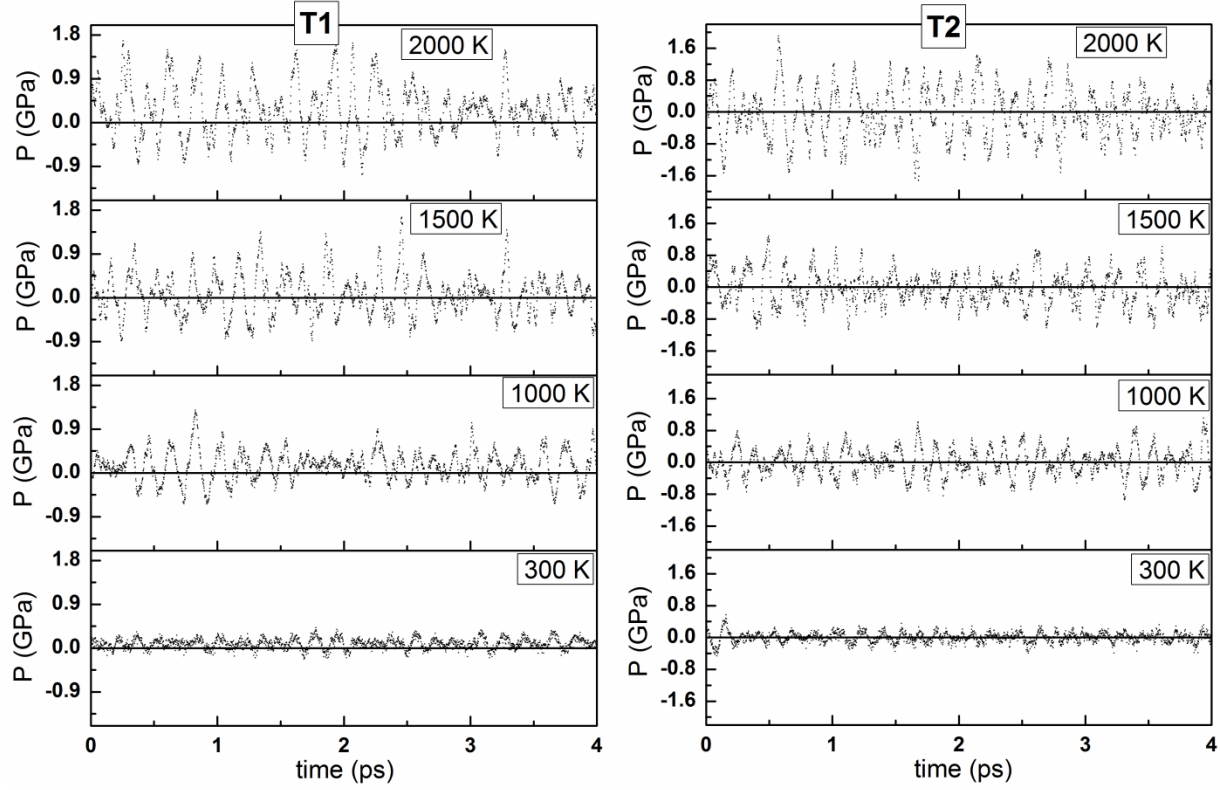


Figure 31. Pressure fluctuation during the AIMD relaxation of (a) T1, (b) T2 for temperatures 300 K, 1000 K, 1500 K and 2000 K

7.3 Thermal expansion and mechanical property calculation

The thermal expansion was calculated by plotting a and c as a function of averaged temperature. Assuming a linear thermal expansion for a and c , the CTE (α) for each axis can be calculated using, $\alpha_a = a_0^{-1} (da/dT)$ where a represent the axis and a_0 is the respective value of the axis at the ambient temperature. By calculating the ratio α_c/α_a one can obtain TEA. The reliability of the CTE in comparison with the experiment is an indicator of the reliability of the AIMD configurations which greatly encourages the following C_{ij} calculation.

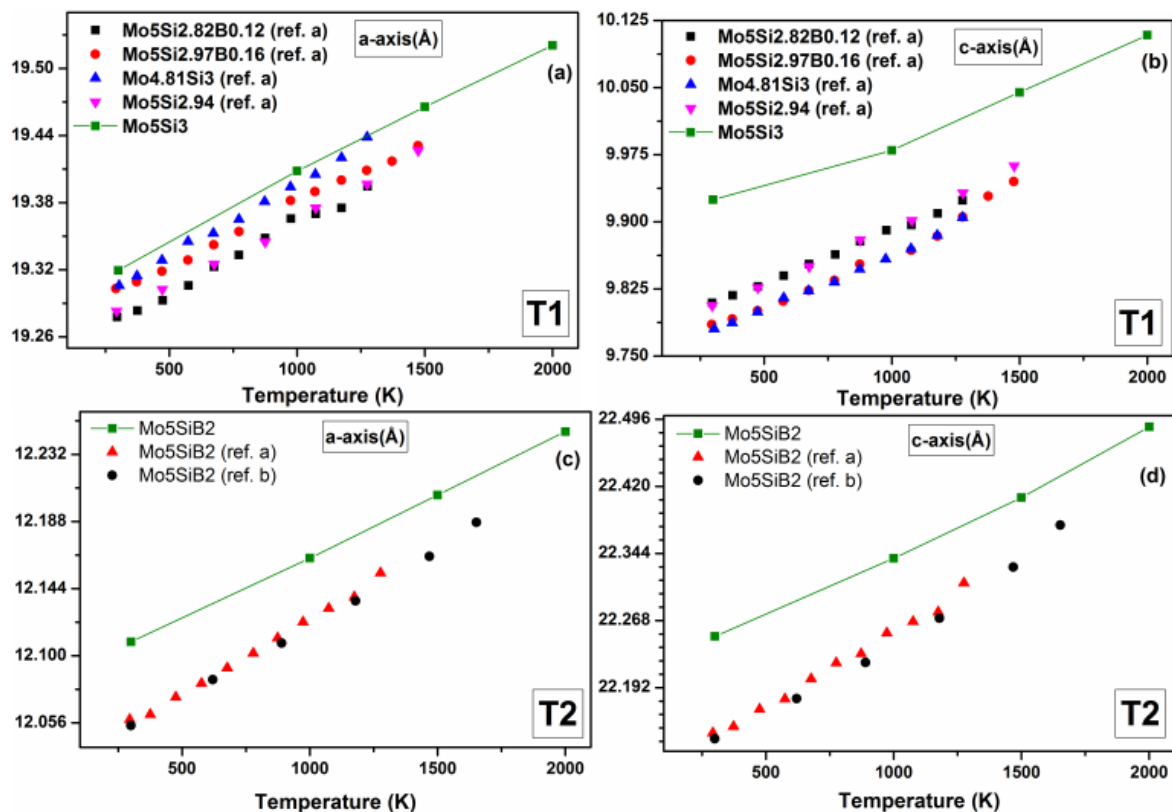


Figure 32. The calculated and experimental (^a ref. ¹¹⁶, ^b ref. ¹²⁵) thermal expansion of T1 on (a) *a*-axis, (b) *c*-axis and on T2 phases (c) *a*-axis, (d) *c*-axis

Because of the fluctuations, final output from the AIMD optimization is not representative as mentioned earlier. Therefore, a sampling procedure was adopted prior to stress-strain analysis. Therefore, the last four structures of the most relaxed atomic configurations were taken at a given NVT simulation that has the desired instantaneous temperature and pressure. During the 4ps run as stated above, 2000 configurations are obtained, with each having an instantaneous pressure and temperature. Four structures were taken as a sample from this batch by taking the last four structures having an instantaneous temperature at the targeted temperature and the instantaneous pressure which is closest to mean pressure. The structures were then used to calculate the

elastic tensors using the stress-strain method ^{34, 126} as in the usual calculation for crystals at zero temperature. It was assumed that all the temperature effect is reflected in the structure obtained from filtered AIMD structures at that temperature. For this purpose, a strain of $\pm 1\%$ is applied to the structures obtained from AIMD. The elastic property calculation procedure is discussed in section 2.3.2.

Thermal expansion is a good indicator to validate method used in this study. Many previous work ^{114b, 116, 125} had assumed linear thermal expansion within the considered temperature range. The expansion of *a* and *c* from this study is shown in **Figure 32** together with the experimental data. The agreement is excellent for T1-a with ref ¹¹⁶ whereas the c-axis is overestimated by only 1.5% at low temperatures but improves at higher temperatures. The alloy sample used in ref ¹¹⁶ is slightly off stoichiometric thus could contribute to the discrepancy. A similar comparison for T2 phase shows the agreement improves with increasing temperature. Following the method used in the experimental work, it was considered that a linear fit for the thermal expansion of the *a*-axis and *c*-axis, in order to calculate the CTE. The calculated CTE and TEA is tabulated in **Table 12** along with the experimental data for the T1 alloys in ref. ¹¹⁶ and the T2 single crystal data in ref. ¹²⁵. Experimental data on ref. ¹¹⁶ show that the CTE is quite sensitive to the Si concentration and results of this study are closest to $\text{Mo}_{4.81}\text{Si}_3$, whose composition is the closest to Mo_5Si_3 . It was however noted that the measured CTE and TEA for single crystal Mo_5Si_3 on ref ^{114b} is higher (22%) than calculated values as well as those measured in ref ¹²⁵. Overall, the AIMD simulation result shown in **Table 12** depict the high anisotropy of CTE in T1 phase, and lack of it in T2 phase is consistent with the experimental observations.

Table 12. Calculated CTE and TEA of a-axis, c-axis by linear fitting along with available experimental data.

| | $\alpha_a (10^{-6} \text{ K}^{-1})$ | $\alpha_c (10^{-6} \text{ K}^{-1})$ | (α_c/α_a) |
|---|-------------------------------------|-------------------------------------|-----------------------|
| Mo ₅ Si ₃ (present) | 6.14 | 11.00 | 1.80 |
| Mo ₅ Si _{2.82} B _{0.12} ^a | 6.27 | 11.90 | 1.89 |
| Mo ₅ Si _{2.97} B _{0.16} ^a | 5.72 | 13.90 | 2.43 |
| Mo _{4.81} Si ₃ ^a | 6.89 | 12.64 | 1.83 |
| Mo ₅ Si _{2.94} ^a | 6.27 | 13.48 | 2.15 |
| Mo ₅ Si ₃ ^c | 5.20 | 11.50 | 2.21 |
| Mo ₅ SiB ₂ (Present) | 6.71 | 6.25 | 0.93 |
| Mo ₅ SiB ₂ ^a | 7.72 | 7.20 | 0.93 |
| Mo ₅ SiB ₂ ^b | 7.90 | 7.50 | 0.95 |

^a ref. ¹¹⁶ Temperature [290 – 1475 K]

^b ref. ¹²⁵ Temperature [300 – 1650 K]

^c ref. ^{114b} Temperature [310 – 745 K]

7.4 Elastic and mechanical property calculation

The T dependence of the C_{ij} for T2 using the above scheme is shown in **Figure 33 (a)** and compared with the experimental results up to 1400K from ref ^{114a}. The agreement is reasonably well with a maximum deviation from the experimental value on C_{66} is about 11%. It should be noted here that even though the AIMD simulations do not assume any symmetry, the temperature dependence of C_{11} equals to C_{22} as expected from a body centered tetragonal symmetry. This is also another confirmation that 2x2x2 supercell is adequate to represent the elastic property of these materials. The stiffness in **a** and **c** directions decreases with temperature is consistent with experimental observations. The relative strength of C_{11} and C_{22} is less compared with the experiment. This could be due to the fact that the c/a ratio is still not exact enough, so the stiffness C_{33} is more than it should be. This study found no experimental data for the T dependence of C_{ij} for the T1 phase but the calculated results are tabulated in **Table 13**. Elastic constants of T1 are less compared to T2, indicating that T2 possess mechanical

properties better suited for high temperature applications. However experimental c_{ij} data for T1 at room temperature ^{114b} is in excellent agreement with results of current study. **Table 13** lists the averaged values of the 4 configurations filtered from the 4ps AIMD run. The accuracy of the method depends on the standard deviation of the sampled models. The **Table 14** listed each value for all the models considered which shows very small deviation for the four sample models for the temperatures considered. This is yet another indication that a 2x2x2 supercell is sufficient for this study.

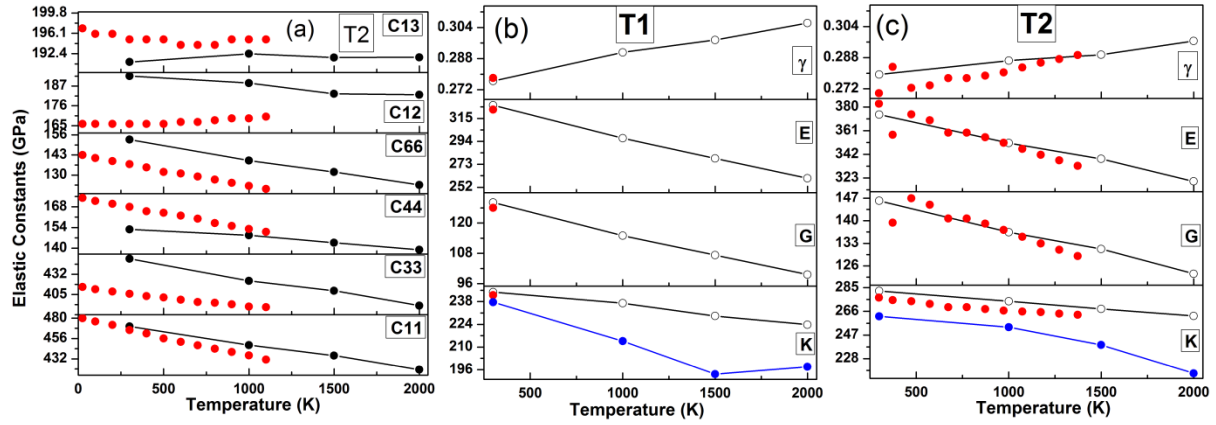


Figure 33. Calculated temperature dependence C_{ij} of T2 and corresponding experimental data ^{114a} (b) calculated bulk mechanical properties (K , G , E , γ) and experimental data at room T ¹²⁷ for T1 (c) calculated bulk mechanical properties (K , G , E , γ) and experimental data ^{114a} for T2. The calculated results are indicated in black circles and the corresponding experimental results are indicated in red circles. The fit to 3rd order BM-EOS ¹²⁴ from isotropic volume change is indicated in blue circles

Table 13. Calculated elastic constants (in GPa) of T1 phase. The experimental data is only available at room temperature (^a ref. ^{114b}).

| T (K) | C11 | C12 | C13 | C33 | C44 | C66 |
|------------------|--------|--------|--------|--------|--------|--------|
| 300 ^a | 446.00 | 174.00 | 140.00 | 390.00 | 110.00 | 140.00 |
| 300 | 448.72 | 173.58 | 137.89 | 406.40 | 111.56 | 135.95 |
| 1000 | 423.18 | 167.07 | 145.75 | 372.58 | 101.96 | 122.30 |
| 1500 | 408.10 | 164.47 | 144.70 | 351.20 | 94.19 | 115.31 |
| 2000 | 389.61 | 162.32 | 146.88 | 334.18 | 88.44 | 109.45 |

Table 14. Elastic constants and bulk mechanical properties (in GPa) of sampled models for temperatures considered for T1.

| T (K) | Model | c11 | c12 | c13 | c33 | c44 | c66 | B | K | E | γ |
|-------|-------|--------|--------|--------|--------|--------|--------|--------|--------|--------|----------|
| 300 | 1 | 446.56 | 174.71 | 138.74 | 408.17 | 110.35 | 136.88 | 244.21 | 127.96 | 326.80 | 0.277 |
| | 2 | 450.10 | 172.20 | 139.08 | 402.03 | 112.96 | 135.25 | 243.73 | 128.05 | 326.89 | 0.277 |
| | 3 | 450.05 | 174.18 | 136.13 | 408.89 | 111.68 | 136.26 | 243.68 | 128.34 | 327.52 | 0.276 |
| | 4 | 448.16 | 173.23 | 137.60 | 406.50 | 111.23 | 135.42 | 243.82 | 128.07 | 326.96 | 0.277 |
| 1000 | 1 | 422.74 | 166.83 | 149.22 | 372.24 | 102.86 | 120.41 | 238.71 | 114.01 | 295.06 | 0.294 |
| | 2 | 422.16 | 166.72 | 149.16 | 372.10 | 102.61 | 120.30 | 238.64 | 113.90 | 294.80 | 0.294 |
| | 3 | 424.35 | 168.23 | 143.95 | 370.53 | 101.40 | 125.06 | 235.09 | 116.03 | 298.91 | 0.288 |
| | 4 | 423.49 | 166.50 | 140.68 | 375.44 | 100.98 | 123.44 | 235.47 | 115.94 | 298.79 | 0.289 |
| 1500 | 1 | 404.64 | 166.03 | 143.19 | 356.81 | 91.99 | 116.54 | 228.86 | 107.32 | 278.44 | 0.297 |
| | 2 | 414.22 | 163.72 | 143.44 | 349.43 | 94.66 | 115.84 | 228.49 | 107.90 | 279.68 | 0.296 |
| | 3 | 406.46 | 164.00 | 144.75 | 353.43 | 94.86 | 114.20 | 229.43 | 107.06 | 277.94 | 0.298 |
| | 4 | 407.08 | 164.12 | 147.44 | 345.11 | 95.25 | 114.67 | 229.85 | 106.75 | 277.31 | 0.299 |
| 2000 | 1 | 388.82 | 160.45 | 147.72 | 332.43 | 89.02 | 107.60 | 223.28 | 99.18 | 259.18 | 0.307 |
| | 2 | 391.93 | 162.59 | 145.12 | 334.73 | 86.27 | 109.78 | 223.64 | 100.45 | 262.10 | 0.305 |
| | 3 | 391.19 | 164.54 | 141.49 | 337.17 | 89.01 | 110.76 | 223.13 | 100.62 | 262.41 | 0.304 |
| | 4 | 386.50 | 161.71 | 153.21 | 332.39 | 89.46 | 109.68 | 225.07 | 98.11 | 256.99 | 0.310 |

To compare results obtained in this study with the experimental data, it was necessary to first apply the VRH approximation ³⁷ on the full elastic tensors (c_{ij}) reported in ref ^{114a} to obtain the bulk elastic properties as shown in **Figure 33 (c)**. This procedure is identical to the method used in the calculation to obtain bulk elastic properties. In addition, K_0 was plotted by the fitting procedure as discussed in the methodology section, which has been a popular method in the previous DFT studies ^{123, 128}. As clearly shown in the **Figure 33 (b) and (c)**, with the assumption of hydrostatic volume expansion (a constant c/a), the K_0 values derived from BM-EOS ¹²⁴ as a function of

temperature deviate quite significantly from both the experimental data as well as the AIMD results even though they do follow the same trend. In contrast calculated results of this study shown in **Figure 33 (c)** is much closer to those derived from the experiments.

Further, current study was able to derive three other important elastic parameters; shear modulus (G), Young's modulus (E) and Poisson's ratio (γ) based on the analysis of the full elastic tensor results from stress-strain method. As shown in **Figure 33 (c)**, these bulk elastic properties for the T2 phase agree with the results derived from ref ^{114a}. There are no experimental data available on the temperature dependent bulk elastic properties of the T1 phase in the published literature. Nevertheless, the available values at room temperature ^{114a} is in excellent agreement with calculated ones. Results of this study show the bulk, shear and Young's modulus decrease monotonically with increasing T , whereas γ increases with T and have a higher slope for T1 than for T2. At low T , γ is close to those typically obtained for ceramics ¹²⁹. As the T increases γ increases to about 0.3, a typical value of a metal ¹²⁹.

The analysis is limited to stoichiometric composition of T1 and T2 phases. Further, it should be mentioned that with regard to the high temperature behavior of intermetallic crystals, there presents additional factors such as the effect of off-stoichiometry and environments as well as their potential impact on the dislocation mobility and the slip planes at very high temperatures. The effect of dislocations, is believed, should be minor at least up to 1500K. Ref. ^{114a} noted that below 1500°C (1773 K) only limited slip planes are active in the T2 phase. Similarly, the T1 phase has limited dislocation mobility at least below 1500K ¹²⁹. The experimental data were conducted

either under vacuum or inert gases^{114, 116, 125} and thus environment effects on the experimental results used for comparison should be minimal. Overall, above results suggest that the AIMD simulation in combination with the stress-strain method can be applied to obtain accurate C_{ij} values and mechanical properties at high temperature.

7.5 Summary and conclusion

This study implemented a simple but very effective method to obtain the temperature dependent elastic and thermal properties of intermetallics in the ternary Mo-Si-B system via AIMD and the stress-strain response method. The combination of AIMD results and subsequent DFT's stress-strain method analysis shows that reliable assessment of elastic and thermal properties is feasible without resorting to explicit T corrections. The results are in excellent agreement with available experimental data. The calculations confirm the abnormal TEA of the T1 phase compared to T2 phase. Furthermore this effect is shown by the Poisson's ratio as well. This study observe a monotonic decrease in principle elastic constants with increasing T and the mechanical strength is higher in T2 compared to T1 and continues to follow the trend at higher T. This method, even with its limitations is fairly straight forward and has no inherent assumptions or extrapolations which make it plausible to be applied to T1 and T2 phases in other TM-Si-B (TM=Transition Metal) systems so that the critical high temperature thermal/mechanical properties can be extracted.

CHAPTER 8

IN SEARCH OF ZERO THERMAL EXPANSION ANISOTROPY IN Mo_5Si_3 BY STRATEGIC ALLOYING

8.1 Introduction

Transition metal 5-3 silicides, particularly Mo_5Si_3 (T1 phase), are important structural phases due to its high melting point (2543 K), strength and excellent creep resistance at elevated temperatures¹³⁰. The tetragonal crystal structure of T1 has two Wyckoff sites for Mo atoms; **4b** (chain site) and **16k** (non-chain site), and two sites for Si atoms; **8h** and **4a** (**Figure 34 a**). The major drawback of the T1 phase is its unusually high thermal expansion anisotropy (TEA) or α_c/α_a of 2.2¹⁸, that results in micro-cracking, leading to mechanical failure. It has been suggested that the high TEA resulted from the anharmonicity originating from the unusually short Mo-Mo bond (2.46 Å) in the **4b** site along the c-axis within the T1 crystal structure¹³⁰. Previous work addressed this issue [3] by selective substitution of Mo with another transition metal (ex. V/Nb)^{18, 131}. However, oxidation resistance of V/Nb alloyed Mo_5Si_3 is typically poor¹³². An alternative strategy is to avoid the substitution of Mo and substituting Si by other metalloid elements such as Al. The multi-directional metallic bonds in Mo_5Si_3 could be altered by substituting Si (**8h**) atoms that are connected to the Mo (**4b**) atoms as indicated in **Figure 34 (b)**. According to a thorough review of literature there is no such study attempted in the past.

Al has been known to improve the oxidation resistance of metal silicides¹³³ through formation of continuous alumina layer that prevents oxygen penetration¹³⁴. It

has also been shown to improve the ductility at room temperature ¹³⁵. There are indirect experimental evidences that Al alloying of the T1 phase may reduce the crack formation after solidification ¹³⁶, which indicates a reduction in TEA ¹³⁷. A substitution of Si by Al in Mo-silicides has generally been known to weaken the Mo-Si bond and enhance the metallic nature of the system ¹³⁸. The substitution of Si by Al is limited to 32 atomic % for T1 phase according to the phase diagram ¹³⁹. However, no experimental thermomechanical properties of $\text{Mo}_5(\text{Si,Al})_3$ alloys are reported. This study intends first to start with alloyed $(\text{Mo,V})_5\text{Si}_3$ where experimental data are available to validate the approach of this study and then proceed with more detailed investigation of Al alloying on the T1 phase.

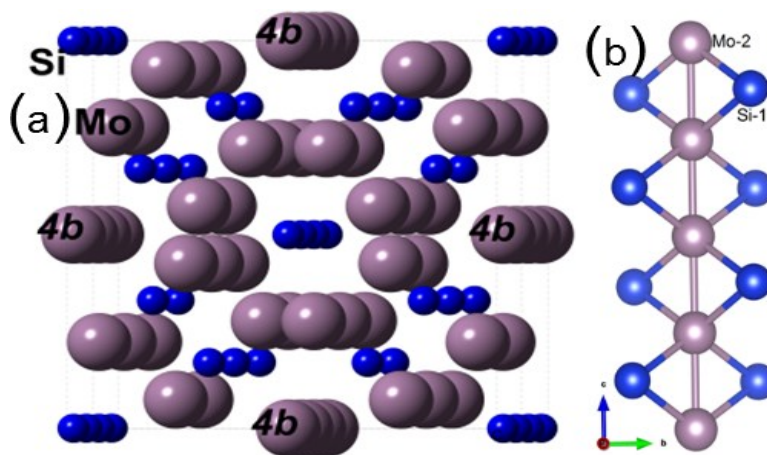


Figure 34. (a) Atomic structure of Mo_5Si_3 viewed from c direction; (b) Mo-2 chain (4b sites) viewed from a-axis direction

Rawn *et. al.* ¹⁸ observed a TEA minimum in $(\text{Mo,V})_5\text{Si}_3$ at 37.5% substitution of Mo with V. This is quite unusual as Mo_5Si_3 and V_5Si_3 are isomorphic and one would expect a monotonic change in the coefficient of thermal expansion (CTE) with V

substitution. Rawn attributed the minimum in TEA to the site preference in substituting Mo by V ¹⁸. At a lower level of substitution, the **4b** chain sites are preferred resulting in a large reduction in TEA. To better understand the microscopic origin of this intriguing thermomechanical properties of the T1 phase alloy and to engineer better high temperature alloys simulations are necessary. Thus this study choose to perform *ab-initio* molecular dynamics (AIMD) simulations on T1 phase alloys up to a temperature of 2000K. The AIMD method based on density functional theory (DFT) has an inherent advantage of having accurate potential as opposed to traditional classical MD methods. It can implicitly account for anharmonicity and is capable of directly observing the thermomechanical behavior at high temperatures ^{25c, 140}. Goal of this study is to first demonstrate that the AIMD can explain the unusual alloying effect in (Mo,V)₅Si₃ and then make a more in depth analysis of the Mo₅(Si, Al)₃ alloy via AIMD simulations. This is achieved theoretically by using second and third order elastic constants, and additional evidence via directionally resolved phonon density of states (DOS). Previous studies on the T1 phase (Mo,V)₅Si₃ show that the difference in third-order elastic constants C₁₄₄ and C₃₄₄, may be the main reason for lattice anharmonicity ^{130, 131b, 141}. There were no such studies presented before according to available literature, despite the tremendous importance and implication on its applications.

The outline of this study is as follows. In the next section, will describe the methods used for the simulation in searching for and the verification of zero anisotropy in T1 phase by strategic alloying. In section 8.3, it will first present the results and discussions on the thermomechanical properties of (Mo,V)₅Si₃ showing good agreement with the experiment ¹⁸. This is followed by a presentation of thermomechanical

properties of $\text{Mo}_5(\text{Si},\text{Al})_3$ and detailed analysis on the atomistic origin of zero TEA in this new alloy. The study wish to end with a brief conclusion.

8.2 AIMD methodology and modeling details

Study used Vienna *Ab initio* Simulation Package (VASP)²⁸⁻²⁹ for AIMD under a constant temperature and pressure (NPT) ensemble using following specifications: (1) The PAW-PBE potentials³⁰ within the generalized gradient approximation(GGA); (2) electronic convergence criterion set at 10^{-5} eV with an energy cutoff of 350 eV; (3) simulation time step of 2 fs each with a total simulation time up to 12 ps; (4) a single Γ point sampling. It was tested the AIMD simulations at a higher energy cutoff, but no significant improvement was observed.

8.2.1 NPT simulations

A 2x2x2 supercell of the T1 phase (256 atoms) in a tetragonal unit cell was used to construct initial models for $(\text{Mo},\text{V})_5\text{Si}_3$ and $\text{Mo}_5(\text{Si},\text{Al})_3$ alloys. The concentration of V at each Wyckoff site was guided by the experimentally observed values of Rawn *et. al.*¹⁸. The vanadium atoms are randomly distributed on each site. It was considered that V composition of 0% (Mo_5Si_3), 5.1%, 12.5%, 25.8%, 37.5%, 50% and 62.5% (V_5Si_3) for the simulation of alloy. For each composition, AIMD were carried out at five temperatures (300K, 700K, 1000K, 1300K and 1500K) for CTE estimation. In the 2x2x2 supercell of the T1 phase there are 96 Si atoms at both the **8h** and **4a** sites (**Figure 34 a**). As a beginning, Al was randomly distributed on the available Si sites. Four alloy models were constructed with 5.2%, 15.6%, 20.8%, 25% and 30.2% by Al substitution.

The percentages are calculated with respect to the number of Si sites, not on the total number of atoms. For example, the model with 5.2% has 5 Si atoms replaced with Al atoms in the cell. The total atomic percentage for this model is 1.9% Al. AIMD for $\text{Mo}_5(\text{Si},\text{Al})_3$ alloys were carried out at four temperatures (300K, 1000K, 1500K and 2000K).

In the AIMD simulation, pressure, temperature, volume and lattice constants fluctuate throughout the simulation time. **Figure 35** illustrates such fluctuations for pressure and temperature. However, after the initial ballistic stage (up to 1ps) their average values remain roughly constant. The thermodynamic parameters were taken from the average values excluding data from the initial ballistic stage. The CTE was obtained from the slope of lattice constants a and c variation vs. temperature from NPT simulations. The thermal expansion anisotropy was defined as the ratio of CTE in the crystallographic a and c directions ($\text{TEA} = \alpha_c/\alpha_a$).

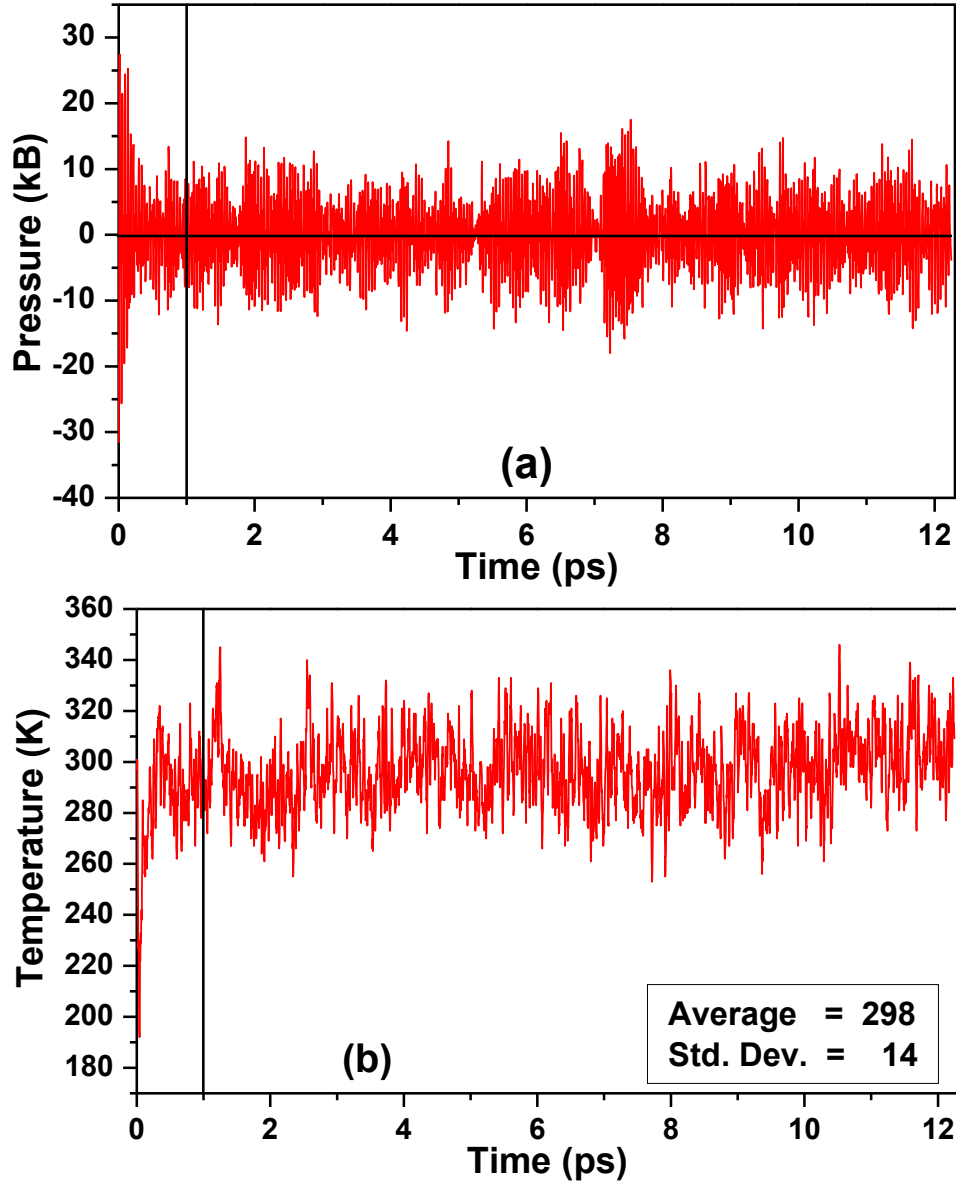


Figure 35. Fluctuation of: (a) pressure and (b) Temperature as a function of AIMD run time in the model with 25% V concentration at 300K. Averages are taken from data after the 1ps time represented by the vertical line.

8.2.2 Second and third order elastic constants

To better understand the effect of Al substitution in the proposed new $\text{Mo}_5(\text{Si}, \text{Al})_3$ alloy, it is necessary to analyze the elastic tensor of the equilibrium structure. To this end, The study used the stress-strain method^{34, 126} to calculate the elastic tensor for

selected unit cell models of $\text{Mo}_5(\text{Si,Al})_3$ including the hypothetical “ Mo_5Al_3 ” phase (See **Section 8.3.2** for details). Then $\pm 1\%$ strain was applied to the fully relaxed unit cell structure. The elastic property calculation procedure is discussed in section 2.3.2. The resulting C_{ij} are then averaged over the symmetry equivalent elements. The Cauchy-Born stability criteria ¹⁴² was then checked for each of these crystals.

The third-order elastic constant is derived by fitting the second-order elastic constant (c_{ij}) as a function of the lattice parameter expansion in the a and c directions ^{131b}.

$$c_{ij} = c_{ij}^0 + 2 c_{1ij} \left[\frac{\delta a}{a} \right] + c_{3ij} \left[\frac{\delta c}{c} \right] \quad (8.1)$$

Where c_{ij}^0 is the second-order elastic constant of the crystal at its equilibrium lattice parameters and with relaxed internal parameters. The lattice expansion for this purpose was limited to a maximum of 2 % strain, to comply with the linear elasticity assumption ^{131b}.

8.2.3 Phonon density of states

The phonon density of states (DOS) in MD simulations can be obtained from the Fourier transform of the velocity autocorrelation function (VACF). A MD post processing package called "nMoldyn" ¹⁴³ was used to obtain phonon DOS. The NPT simulation described above provides the optimal cell volume and the crystal parameters at the given temperature and 1 atm pressure. This information was used to perform an NVT (fixed volume and temperature ensemble) simulation to extract the vibrational behavior

at equilibrium. The atom-resolved phonon DOS is extracted from VAFC for individual atoms within the supercell according to:

$$C_{vv}(t) = \frac{1}{N} \sum_{\alpha=1}^N w_{\alpha} \frac{1}{3} \langle v_{\alpha}(0) \cdot v_{\alpha}(t) \rangle \quad (8.2)$$

Where v_{α} and w_{α} are the velocity at a given time and the weighting factor (based on mass) for each atom α . The total phonon DOS can be estimated from the summation of the Fourier transform of the VACF of individual atoms:

$$G(\omega) = \int_0^{\infty} dt \cos[\omega t] C_{vv}(t) \quad (8.3)$$

For an illustration, **Figure 36** shows the VACF of the NPT calculation for Mo_5Si_3 at 300K. In this study, VACF stabilizes after 1ps. thus the averaging of AIMD data after 1 ps is reasonable.

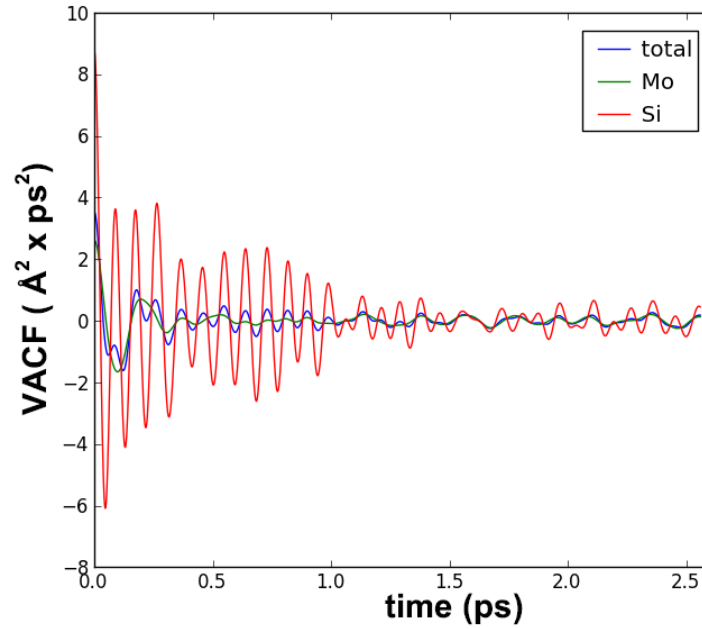


Figure 36. Velocity auto correlation function (VACF) for Mo and Si in Mo_5Si_3 at 300K.

8.3 Results and discussion

This section is divided into two parts. In section 8.3.1 shows results of CTE and TEA for $(\text{Mo,V})_5\text{Si}_3$ and $\text{Mo}_5(\text{Si,Al})_3$ alloys. The experimentally unusual TEA behaviour for the $(\text{Mo,V})_5\text{Si}_3$ alloys is well represented in simulations. Same procedure was employed to $\text{Mo}_5(\text{Si,Al})_3$ alloys and observed the reduction in TEA. **Section 8.3.2** is dedicated to identifying and explaining origin of the TEA in the T1 phase and to understand the effect of Al alloying by three different theoretical tools. Namely, Second and third order elastic constants and phonon DOS. The directionally resolved phonon DOS in particular, shows the origins of the anisotropic effect.

8.3.1 Coefficient of thermal expansion (CTE) and thermal expansion anisotropy (TEA)

The CTE and TEA for $(\text{Mo,V})_5\text{Si}_3$ and $\text{Mo}_5(\text{Si,Al})_3$ alloys are calculated using the method explained in **Section 8.2.1** above. The results for different V concentrations for $(\text{Mo,V})_5\text{Si}_3$ alloys are shown in **Figure 37** together with the experimental data which exhibit unusual TEA behavior in $(\text{Mo,V})_5\text{Si}_3$ as observed by Rawn et. al.¹⁸. Indeed, in **Figure 37 (a) and (b)**, the variation of α_c and α_a as a function of V concentration was qualitatively reproduced. At low V concentration, α_c decreases rather rapidly, reaching a minimum at 25.8% concentration, and increases thereafter. On the other hand, α_a increases only very moderately as V concentration increases with a slightly faster initial rate. The combined behavior for α_c and α_a resulted in a minimum of TEA shown in

Figure 37 (c). The minimum in TEA was located in the range of 25-40 % of V concentration in reasonable agreement with the experiment ¹⁸.

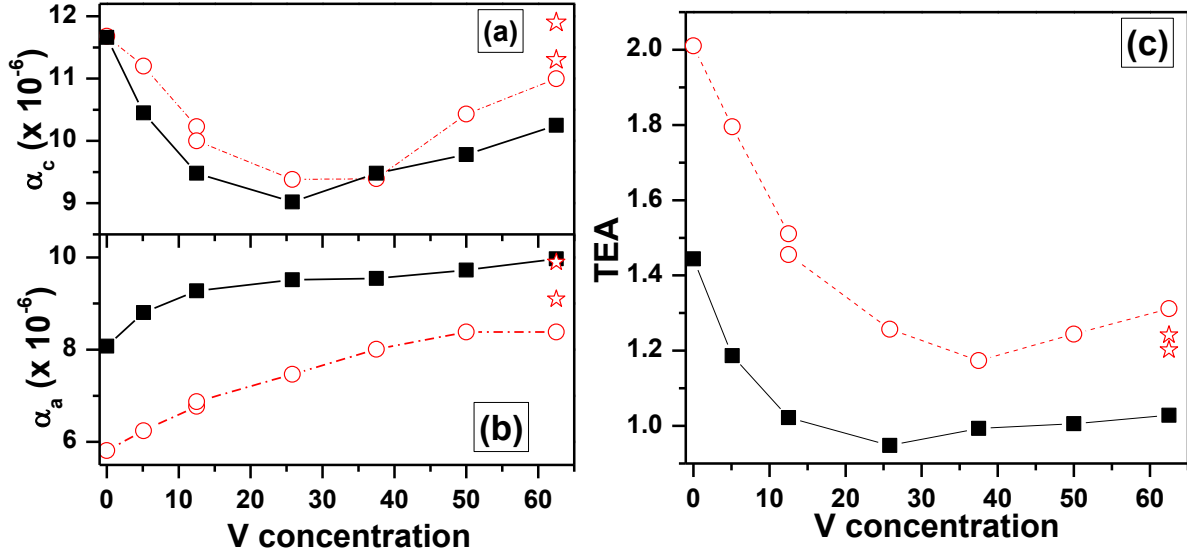


Figure 37. Simulated CTE for (Mo,V)₅Si₃ as a function of Vanadium concentration: (a) α_c , and (b) α_a ; (c) TEA. Experiment data are from Rawn et al (2005) shown in red open circles and Rodrigues et al (2009) shown in red open star symbols.

The data in **Figure 37** not only show the capability of AIMD to capture the essential features of the CTE and the TEA in V substituted T1 phase models, but also show quantitative variations with experimental data. The α_a shows a deviation of 2×10^{-6} at low V concentrations but shows a better agreement with a smaller deviation of 1×10^{-6} at higher concentrations. There could be many reasons for the deviations, such as: (1) The data from AIMD simulations was based on a wider range of temperature (300K-1500K) than the range in experiment ¹⁸ (303K-873K), (2) A 2×10^{-6} deviation in CTE corresponds to a change in lattice parameters by at least 0.02 Å, which is beyond AIMD resolution in the present calculation. The standard deviations of *a* and *c* of the simulation were 0.07Å and 0.04Å respectively, (3) A 2x2x2 supercell (256 atoms) is of

limited size for an alloyed system, especially for larger V concentration. Currently, using a larger supercell for AIMD is computationally prohibitive, (4) There may be experimental uncertainty with respect to the CTE values themselves. For example, using a wider temperature range (up to 1400K), Rodrigues et al.¹⁴⁴ reported CTE values for V_5Si_3 closer to results of this study [Figure 37 (b)]. Despite these minor difference, the AIMD simulations using NPT ensembles do capture the unusual TEA behavior of $(Mo,V)_5Si_3$ and provided motivation to explore the possibility of zero TEA in the T1 phase with other alloying elements.

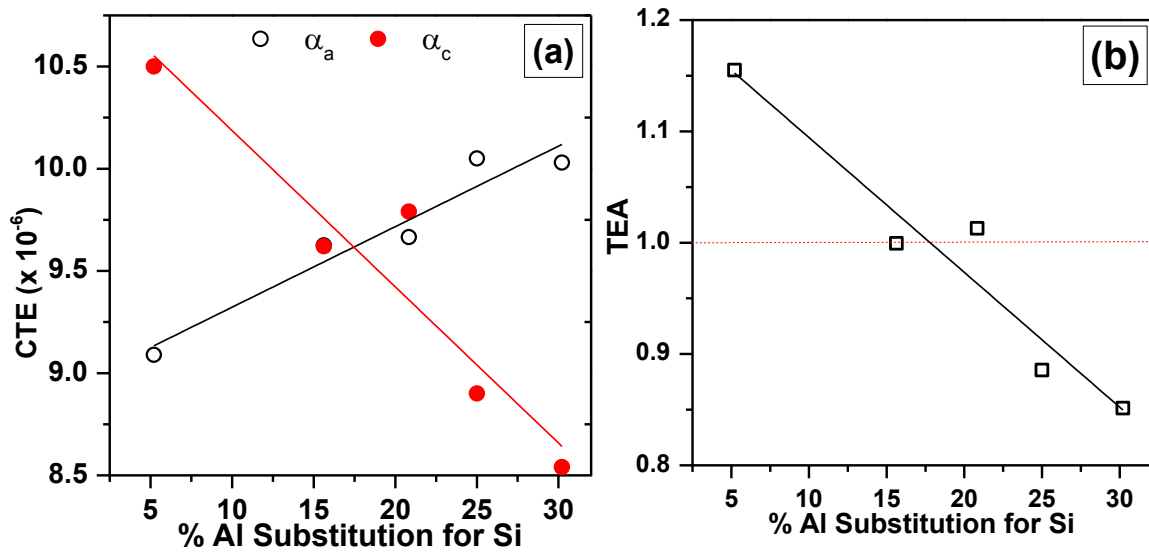


Figure 38. Simulated (a) CTE and (b) TEA as a function of % Al substitution in $Mo_5(Si,Al)_3$ alloys.

With the validation of AIMD technique for $(Mo,V)_5Si_3$ alloys, the same procedure was applied to $Mo_5(Si,Al)_3$ alloys where no experimental data exist. Within the limit of Al solubility in the T1 phase, according to the reported Mo-Si-Al phase diagram at 1823K¹³⁹ five $Mo_5(Si,Al)_3$ alloyed supercell models were generated with different Al

concentrations. As mentioned about Al atoms are randomly substituted on Si sites. Several random models were tested in this study for each composition but found no significant change in CTE. The total free energy per atom, of the five models changed linearly from -9.225eV to -9.005eV. Although the stability cannot be known exactly because of the difference in compositions, the linear increase hints that they are stable structures. Furthermore, cohesive energy was calculated for further confirmation of the stability of the supercell models. To calculate the cohesive energy, study followed the method described in ref. ¹⁴⁵. The Mo bcc crystal, Si in diamond structure and Al fcc crystal structures were taken as the reference states. The cohesive energies for the five models are -0.384, -0.358, -0.342, -0.331 and -0.319 eV/atom respectively. Therefore, the alloy models studied are structurally stable according to this criterion. The results of α_c and α_a from AIMD simulation as a function of % of Al substitution on the Si site are shown in **Figure 38 (a)**. There is an approximate linear decrease in α_c and a concomitant linear increase in α_a as Al content increased. The two lines intersect at 17.5% Al substitution, indicating an *isotropic* CTE (TEA=1) at a small Al substitution, well within the solubility limit is possible. Considering the fact that 60 % of V substitutions on Mo sites are required to yield a minimum TEA, Al should be a far more effective alloying element than V in reducing TEA. It is highly desirable that experimental measurements be conducted to verify this exciting discovery.

8.3.2 Discussion on lattice anharmonicity in $\text{Mo}_5(\text{Si},\text{Al})_3$ models

In order to find the origin for the reduction of lattice anharmonicity associated with the Al substituted T1 phase, additional static calculations were performed on the elastic

coefficients of four unit cell crystals with T1 structure corresponding to a 0.0% (Mo_5Si_3), 16.6%, 83.3%, and 100% (Mo_5Al_3) replacement of Si by Al. The last two crystals are hypothetical since they exceed the Al solubility limit in T1. For elastic coefficient calculations, the unit cell has to be used in contrast to a large supercell used in the AIMD because the crystal has to be at the equilibrium structure as explained in section 8.2.2. **Table 15** shows optimized structures and the second-order elastic constants. For Mo_5Si_3 , the calculated values are in excellent agreement with the experimental data ^{114b}. There is an overall decrease in elastic constants (C_{ij}) as a function of Al content due to an increase in the weaker Mo-Al bonding ¹³⁸. All calculated C_{ij} are positive and satisfy the Cauchy-Born elastic stability criteria, i.e. $((C_{11}-C_{12})/2 > 0)$. Mo_5Si_3 exhibits a large difference in C_{11} and C_{33} (~ 23 GPa) indicating a larger elastic anisotropy. This can be explained by the strong directional bonding in the basal plane (001) than those in the [001] direction (i.e. $C_{11}+C_{12} > C_{33}$ and $C_{66} > C_{44}$) ¹³⁰. The same trend can be observed in all 4 crystals of **Table 15**. The difference ($C_{11}-C_{33}$) however, is reduced to only 12GPa in Mo_5Al_3 . The message is that the Al substitution on Si sites reduces the elastic anisotropy in T1 phase structure by softening the directional bonding in the basal plane. This elastic anisotropy may have a direct correlation with CTE and TEA behaviour shown in **Figure 38 (a) and (b)**.

Table 15. Calculated second-order elastic constants (GPa) for a T1 unit cell substituting Al on Si sites. Number in the parenthesis is the experimental data^a

| %Al | C_{11} | C_{33} | C_{44} | C_{66} | C_{12} |
|--------------|------------------------|------------------------|------------------------|------------------------|------------------------|
| 0.00 | 439(446 ^a) | 394(390 ^a) | 110(110 ^a) | 137(140 ^a) | 177(174 ^a) |
| 16.67 | 426 | 388 | 109 | 129 | 160 |
| 83.33 | 370 | 359 | 96 | 96 | 113 |
| 100.0 | 360 | 347 | 94 | 94 | 113 |

^a ref ^{114b}

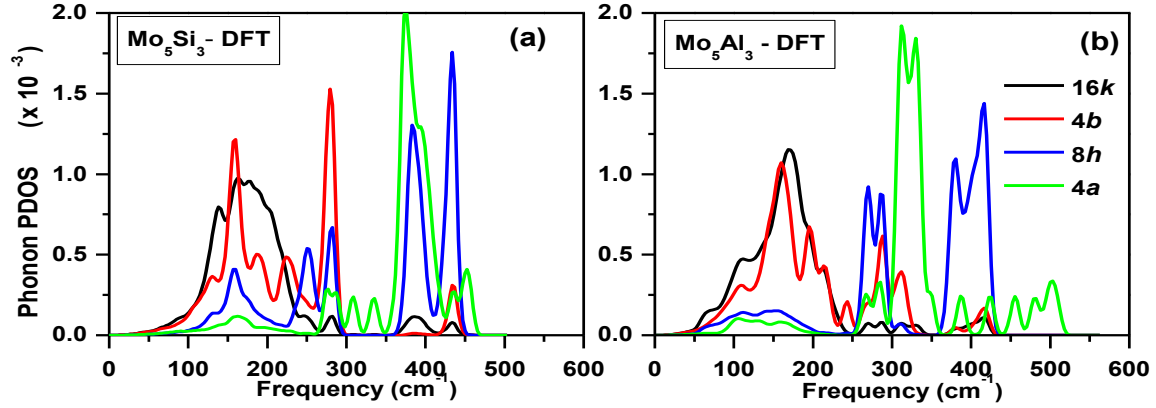


Figure 39. Calculated phonon DOS at the ground state using DFT for: (a) Mo_5Si_3 ; (b) Mo_5Al_3 .

To gain an even better insight into the role of Al alloying, third order elastic constants of four crystalline models in **Table 15** within the linear elastic limit were computed using a maximum strain of 2%. According to C. L. Fu^{131b}, a key to reducing TEA in T1 phase structure is to minimize the difference between the third order constants C_{144} and C_{344} , i.e. the rate of reduction of C_{44} as the lattice expands in a and c directions. In reference^{131b}, it was shown that this difference is minimized with 20% V substitution for Mo in $(\text{Mo},\text{V})_5\text{Si}_3$ (i.e. $C_{144} - C_{344} \sim 100$ GPa). **Table 16** lists all calculated third order elastic constants for the four models and highlighting the C_{144} and C_{344} , including the data for Mo_4VSi_3 from ref.^{131b}. There is a large difference in magnitude initially between C_{144} and C_{344} for Mo_5Si_3 . With increasing Al substitution, the difference between the two third order elastic constants is reduced. In fact, only a relatively small Al substitution ($\sim 16.67\%$) is needed to reduce its difference to 169 GPa, which is slightly larger than the value of 100 GPa for 20% V substitution in $(\text{Mo},\text{V})_5\text{Si}_3$. This supports the finding that Al is more effective in reducing the anisotropy in CTE for the T1 phase as observed directly from the AIMD simulations.

Table 16. Calculated third-order elastic constants (GPa) of $\text{Mo}_5(\text{Si},\text{Al})_3$. Here $C_{111} + 3C_{112}$ and $C_{113} + C_{123}$ measure the ‘softening rate’¹⁴¹ of the tensile modulus $C_{11} + C_{12}$ (GPa) with [100] and [001] expansions respectively.

| %Al | $(C_{111} + 3C_{112})$ | $(C_{113} + C_{123})$ | C_{333} | C_{133} | C_{144} | C_{344} | $(C_{144} - C_{344})$ | C_{166} | C_{366} |
|----------------------------------|------------------------|-----------------------|-----------|-----------|-------------|-------------|-----------------------|-----------|-----------|
| 0.00 | -4284 | -1294 | -4304 | -993 | -289 | -569 | 280 | -697 | -317 |
| 16.67 | -4016 | -1675 | -1886 | -739 | -300 | -469 | 169 | -516 | -268 |
| 83.33 | -3886 | -1104 | -2058 | -859 | -214 | -166 | -48 | -190 | -77 |
| 100.0 | -4120 | -950 | -1945 | -1133 | -390 | -343 | -48 | -363 | -40 |
| $\text{Mo}_4\text{VSi}_3^{131b}$ | -5200 | -1300 | -2500 | -850 | -350 | -450 | 100 | -600 | -300 |

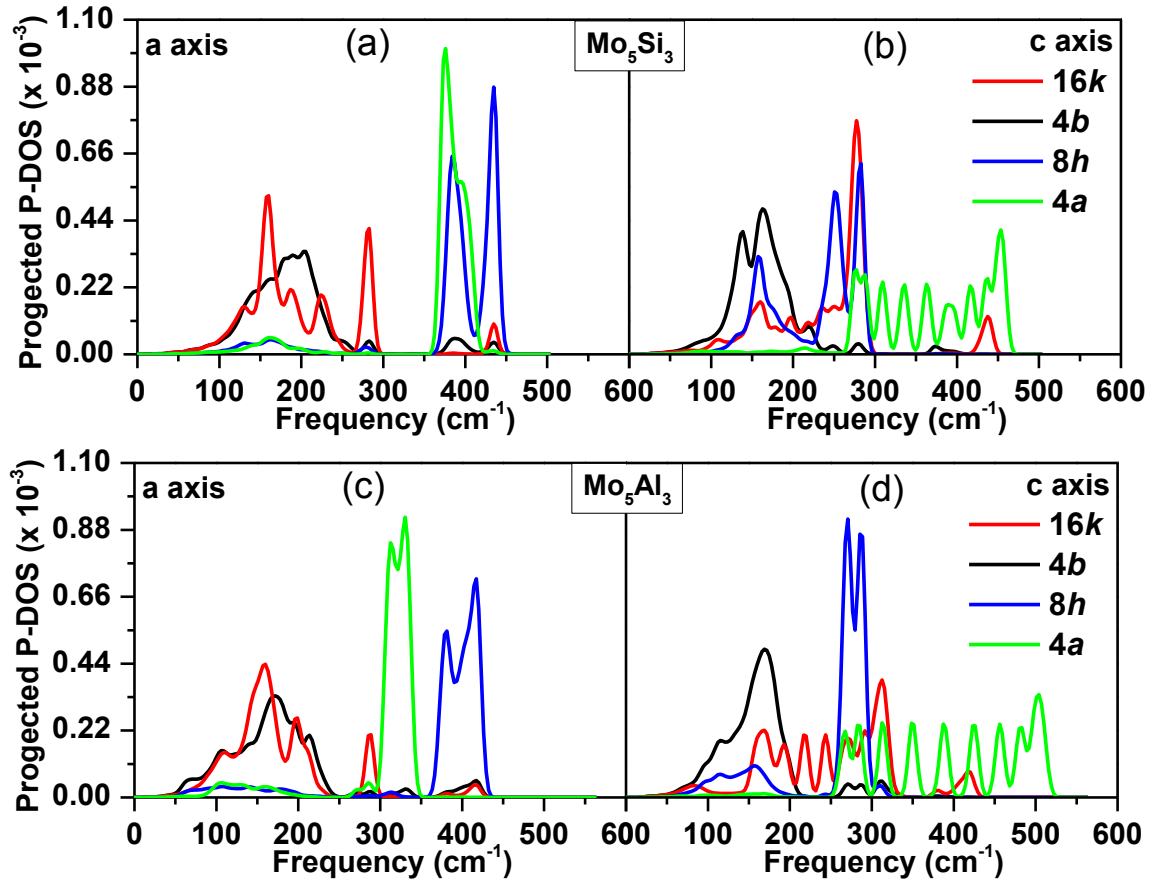


Figure 40. Ground state phonon PDOS projected along: (a) *a* direction and (b) *c* direction for Mo_5Si_3 ; and (c) *a* direction and (d) *c* direction for Mo_5Al_3 .

The Al effect shown above is quite surprising at first sight as no part of Mo-chain (**4b**) atoms are substituted by Al and thus one would expect its impact on the lattice anharmonicity to be minimal. However, as shown in **Figure 34 (b)**, the Mo-**4b** site is closely surrounded by the **Si-8h** sites as its first nearest neighbor (NN) forming Mo-Si and Mo-Al directional bonds. Thus, the substitution of Si by Al may indirectly impact the vibrational behavior in the Mo atoms at the **4b**, sites due to the nature of multi-centered bonding, especially in the vicinity of Mo-Mo chains ¹³⁰. The occurrence or absence of the vibrational coupling between the two species can be detected by the degree of degeneracy in the atom-resolved phonon spectra in the T1 crystal structure. To support this hypothesis, phonon DOS was evaluated and compared for both Mo₅Si₃ and the hypothetical Mo₅Al₃ compound with T1 structure using direct DFT phonon calculations ¹⁴², as well as from VACF via AIMD simulations. As shown in **Figure 39 (a)**, the phonon partial DOS (PDOS) from the **Mo-4b** site in Mo₅Si₃ at ground state shows a significant presence of high frequency peaks from Moatom in the 280-330 cm⁻¹ range which overlap with the PDOS from the **Si-8h** sites. This feature is not as pronounced in Mo₅Al₃ as shown in **Figure 39 (b)**. In contrast, the phonon PDOS from Mo-**16k** site is at the same low frequency range in both crystals. It is necessary to go a step further to better resolve the PDOS in different directions in these two crystals. In **Figure 40 (a)-(d)**, directionally decomposed phonon PDOS was displayed for Mo₅Si₃ and Mo₅Al₃ which clearly indicates that the phonon structure in the high frequency range (**Figure 39 (a)**) is largely due to the c-axis orientated vibration from the **4b** sites. These phonon modes are strongly coupled with the c-axis oriented phonon modes from the **8h** sites, as evident by the overlapping peaks.

It was also extracted the axially-resolved phonon PDOS of the four types of Wyckoff sites at 1500K from VACF of the AIMD simulations data for Mo_5Si_3 and Mo_5Al_3 (see section 8.2.3). They are shown in **Figure 41 a-b** and **Figure 41 (c-d)** respectively. While the characteristics phonon peaks from the Mo-**16k** and Mo-**4b** sites along the *a*-direction are generally the same for both compounds, the respective component of the phonon spectra along the *c*-axis differ considerably. In the *a*-direction, the **16k** and **4b** site Mo atoms vibrate with a low frequency that is largely uncoupled with the phonon modes from the **Si-8h** atoms (see **Figure 41**, upper panel). For the *c*-axis vibrations (**Figure 41**, lower panel), the atoms in **Mo-16k** sites still maintain the low-frequency phonon spectra similar to that in the *a*-direction, but the atoms in **Mo-4b** sites exhibit an additional phonon peak at the higher frequency range (280-330 cm^{-1}). This is especially true for Mo_5Si_3 (**Figure 41 (b)**). For Mo_5Al_3 , a much less distinctive feature at the low and high frequency phonon spectra is seen instead (see **Figure 41 (d)**). This explains why, despite the absence of a direct Mo substitution at the **4b** chain sites, the anharmonicity can still be altered significantly with Al alloying at 8h site. Obviously, the weakening of the Mo-Si bonding by an Al substitution, not only reduces the elastic anisotropy of the T1 phase, but also profoundly alters the vibrational characteristics of the adjacent **Mo-4b** sites.

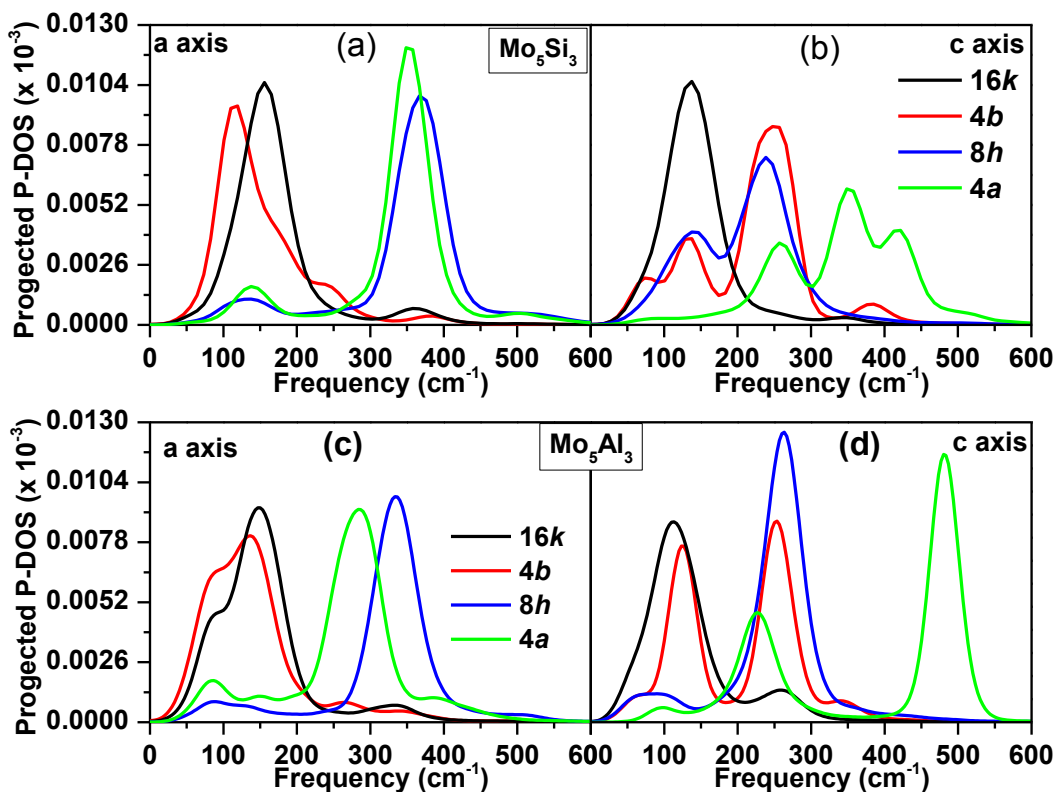


Figure 41. Phonon PDOS from AIMD at T=1500K for Mo_5Si_3 projected on the (a) **a-axis** (b) **c-axis** and for Mo_5Al_3 projected on the (c) **a-axis** (d) **c-axis**.

8.4 Conclusion

In conclusion, study discovered the possibility of an isotropic T1 phase in $\text{Mo}_5(\text{Si},\text{Al})_3$ alloys with a considerably low level of Al substitution. The method and approach used is first validated by comparing data between theoretical and experimental values for $(\text{Mo},\text{V})_5\text{Si}_3$ alloys. Previous studies on V substituted T1 phase focused on the short Mo-Mo bond length of 2.46 Å at the **4b** site as the primary source for anisotropy. The finding of the study shows this is more related the **Si-8h** site attached to the chain, not as much due to Mo-Mo BL shortening. The origin of the Al alloying effect in T1 is fully explained by the well-established second and third order

elastic constant interpretations along with the decoupling of phonon modes pertaining to **4b** and **8h** sites in T1 structure. This finding of atomistic origin in explaining reduction in TEA in $\text{Mo}_5(\text{Al},\text{Si})_3$ will have a major impact in the application of Mo-based T1 alloys for high temperature applications. In principle, one can take advantage of this approach in addressing the TEA of a wider range of intermetallic compounds.

CHAPTER 9

FINAL REMARKS AND FUTURE WORK

The main goal of this exercise is to unravel the atomistic structure of “calcium silicate hydrate” and extending it to include “calcium aluminosilicate hydrate” via *ab initio* techniques. It was established at the beginning, lack of fundamental understanding of the electronic structure of C-S-H leads models, theories and predictions that do not help much. Thus the bottoms up approach used in this study by starting with known crystal structures and using fundamental understanding gained in developing a structural model for the C-(A)S-H. Since the most important property of interest in cement is the mechanical strength, study focused to better understand on mechanical properties.

The study starts with four CSH crystals (Chapter 3) to understand their electronic properties and bonding in an attempted to find their correlation to mechanical properties. The choice of these four crystals was motivated by the understanding from a thorough review of literature, which led to the conclusion that they are the closet resembling crystalline counterparts to C-S-H in cement gel. This study concluded with a construction of electronic parameter called TBOD that shows correlation of electronic to mechanical properties (see section 3.3.4). This parameter was then argued as a good choice for classifying CSH class of crystals (See **Figure 7**). Although they were well chosen, a meager list of 4 crystals is not enough to convincingly build a metric. This led to search for CSH crystals that are with well-known structure. Richardson review (2008)⁴ was found in this search. It cites 30 purely CSH phases known up to date. After a

diligent search, 20 crystal structures were chosen from this database paying attention to 1) to be representative enough of the CSH material, and 2) having unambiguous reported structures (Some do not have fractional coordinates clearly reported). The first thing realized was that Taylor (1980) classification ^{63a} of CSH was limited and poorly classified the CSH class of crystals. Thus the present study used modified Strunz classification ⁶⁵ which was first introduced to cement research community by Garbev *et al* ⁷⁰ as a much suited for CSH to overcome these issues. This study hopes that the cement research community may find motivation in adopting this classification. The main intention of the study was to test the TBOD hypothesis on a bigger sample as 4 crystals were not sufficient as a proper representative sample. It was considered that TBOD is a representative parameter for the cohesion of a material as it averages the strength of all bonds in the unit cell. This is presented in the color maps (See **Figure 12**) given in chapter 4. There are certain trends with TBOD and the internal cohesion of the CSH crystals. The study also did in-depth analysis of the bonding strength of each species. The relative strengths of different bond species and even subtle different configurations of same species were examined and may be of paramount importance for future spectroscopic studies. This is the only study that provides the electronic structure and bonding information of large number of CSH crystals to date. Due to limitations, the study had to limit exploration only on electronic structure. This study also provides much needed clarification of hydrogen positions to the 20 CSH crystals. The hydrogen position reported from XRD always needs to be optimized by an *ab initio* calculation (see section 4.1). Also some reported structures have typographical

mistakes of atomic positions (see section 4.3) thus needed correction. The optimized and corrected atomic structures of 20 crystals in this study can be obtained on request.

To establish any correlation to electronic structure, study focused on mechanical properties of 20 crystal sample. This led to a much refine electronic parameter that is PBOD which is essentially a decomposition of TBOD to each bond species. Silicates govern the mechanical property of CSH as the popular norm in cement research community is thus questioned in this study (see chapter 5). Silicates though the strongest and the major contributor to the TBO, study found that it do not show correlation well with the mechanical properties of different crystal structure. However, data show that PBOD of Ca-O bonds and HBs have a very good correlation with mechanical properties. HB-PBOD gives the best correlation which is not found before. In light of this finding and with hope to establish most important HB type, study analyzed HB network and decomposed it to different contributions based on “Next nearest Neighbor” concept. The definition of 12 different types of HBs (see **Figure 20**) is an original contribution as it is first presented in this work. This will allow future studies to further analyze the HBs in cement and incorporate the finding to build better cement models. In summary, the large database of CSH crystals highlighted importance of HBs to cement and ways to analyze the HB network in-depth. This information will 1) help validate existing models for cement and 2) guide to build new models. It will also help the spectroscopic studies conducted during a better part of last century to re-examine their conclusions.

A recent review (2014) by Richardson ¹⁶ proposed 16 c-s-h (I) models (see section 6.1). This review unified all the experimental information to date and also

structural characteristics of CSH crystals and proposed structures consistent with all of them. This study (chapter 6) strive to test some of the hypothetical models on unified frame of reference with the knowledge gained from studies conducted on chapter 3 - 5. 2 models out of the 16 chosen from proposed C-S-H models that are easily extensible to aluminosilicate as an initial step (see chapter 5). And this study successfully made 3 C-A-S-H (I) models that will pave way to build a realistic model for C-A-S-H (I) and thus for cement. The electronic structure and bonding for these models were presented earlier (chapter 6). This work is still at an early stage thus more work is needed in future. Some of the electronic structure calculations need to be done with more potential types to properly analyze types of bonding in different environments, may be similar to the analysis in Chapter 5. It will be of great importance to study all the 16 structures proposed by Richardson's (2014) review ¹⁶ and generate more models guided by the given templates. The proposed highly ordered C-(A)-S-H (I) phase models will then be instrumental for future simulation studies as seed models to build viable C-(A)-S-H (II) phase models.

It is an important fact of incorporating the environmental conditions (finite temperature and pressure) for simulations of construction material such as C-(A)-S-H. The most suitable method, for simulation of such chemically complex systems is the AIMD. There is no much experience in applying AIMD on cement simulations in the past. It is also accepted that experience is needed on AIMD to guide a successful simulation. However, AIMD has been used for intermetallic systems for many years. Thus it was carefully chosen the construction materials, which are 5-3 silicides as a test case to build experience of simulation with AIMD and to develop new methods for

calculating mechanical properties. In this regard first set out to find a direct approach to simulate mechanical property at high temperature. The T1 and T2 phase intermetallics used in current study was the idea for this purpose. The study successfully captured the mechanical anisotropy observed in the T1 phase (see section 6.1). This is important because mechanical anisotropy is a parameter of interest for C-A-S-H as they are layered crystals. The AIMD methods developed in this study should be directly transferrable to C-A-S-H as well.

The mechanical anisotropy observed in T1 phase is a serious drawback for structural material. Even for C-A-S-H as a construction material, this is an issue and methods must be developed to alleviate its adverse impact. Using T1 phase 5-3 silicides as an example, current study found ways to reduce mechanical anisotropy by alloying. AIMD is a good choice for simulation of alloying. The study validated the observed finding of using Vanadium to reduce the anisotropy. More importantly, the study found Al as a much better alloying agent to remove anisotropy completely. Thus, the much insight gained from these AIMD studies will be important for future research. These studies will motivate application of AIMD in the field of cement research. This will allow simulations to be conducted for a broader area of questions for cement research. One of the most important such area is cement hydration and aging.

APPENDIX A:

A.1 Typical INCAR for NVT calculation

A typical INCAR used in AIMD simulation under NVT ensemble is given below. This will work in VASP 5.2 or higher version and Nose-Hoover thermostat is used for temperature simulation. Cell volume and shape is constrained in this simulation and ISIF tag must be set to 2.

```
SYSTEM = MoSiB

ISTART = 1  #continue from WAVECAR file

LSCALAPACK = .TRUE.

SIGMA = 0.2  #default Check this one!

PREC = normal

NSW = 2500  #max number of steps for IOM, # of MD steps

ISMEAR = -1; SIGMA = 0.086  #smearing method

ALGO = Normal

EDIFF = 1.0e-4  #allowed error in total E

MAXMIX = 30; AMIX = 1.0; BMIX = 1.0  #optimize charge mixer for Si, also for MD

LWAVE = .FALSE.  #determines if WAVECAR is written

LCHARG = .FALSE.  #determines if CHGCAR/CHG are written

LAECHG = .TRUE.  #core to AECCAR0 and val to AECCAR2

NELMIN = 4  #min number of SC steps

ISYM = 0  #switch of symmetry, for MD
```

NPAR = 10 #machine dependent
ENCUT = 500 #ENMAX in POTCAR as needed for accuracy
NELM = 40 #max number of selfconsistence steps, 40 normally
NBLOCK = 1 ; KBLOCK = 1000 #default =1
LPLANE = .TRUE. #good for large cells
LREAL = .TRUE. #projection in reciprocal space, good for large cells

MD (NVT) related

IBRION = 0 #0 for MD, 1 for newton, 2 for conj-grad
ISIF = 2 #must be 2 for NVT
POTIM = 2.00 #time step
RWIGS = 1 1 #wigner seitz radius (need a number for each atom type)
VOSKOWN = 0 #default=0, 1 different interpolation formula
SMASS = 0 #for MD,>=0 NVT, Nose mass parameter
TEBEG = 300 #initial temperature for MD
TEEND = 300 #final temperature for MD

A.2 Typical INCAR for NPT calculation

A typical INCAR used in AIMD simulation under NPT ensemble is given below. This will work in VASP 5.3 or higher version and Langevin dynamics is used to simulate temperature and pressure. Cell volume and shape can change in this simulation and ISIF tag must be set to 3. The friction coefficients (LANGEVIN_GAMMA) for atomic and

cell degrees of freedom are system dependent and can only be optimized with sufficient amount of testing.

SYSTEM = Mo-V1-Si

PREC = normal

NSW = 10000 #max number of steps for IOM, # of MD steps

ISMEAR = -1; SIGMA = 0.086 #smearing method

ALGO = VeryFast

EDIFF = 1E-5 #allowed error in total E

LREAL = Auto #projection in reciprocal space, good for large cells

MAXMIX = 40; AMIX = 1.0; BMIX = 1.0 #optimize charge mixer for Si

LWAVE = .FALSE. #determines if WAVECAR is written

LCHARG = .FALSE. #determines if CHGCAR/CHG are written

LAECHG = .TRUE. #core to AECCAR0 and val to AECCAR2

IALGO=48

NELMIN=5 #min number of SC steps

ISYM=0 #switch of symmetry, for MD

NPAR =24 #machine dependent

ENCUT=350 #ENMAX in POTCAR as needed for accuracy

MD (NPT) related

RANDOM_SEED = 689642361 689642398

IBRION = 0 #0 for MD, 1 for newton, 2 for conj-grad

```

ISIF=3  # variable lattice parameters

POTIM=2  #time step

MDALGO=3  #Langevin dynamics

TEBEG=300  #initial temperature for MD

TEEND=300  #final temperature for MD

## Following Langevin parameters will control the efficiency

LANGEVIN_GAMMA = 10.0 10.0 10.0  #friction coef. for atomic DoFs

LANGEVIN_GAMMA_L=10.0  #friction coef. for lattice DoFs

PMASS=10  #mass for lattice DoFs

PSTRESS=0.0001  #Targeted stress tensor values in Kbar

```

A.3 AIMD scripts for data processing and plotting

Following perl script is to gather thermodynamic data of interest from OUTCAR and OSZICAR. This will allow the used to examine the fluctuations and decide the stability region of the MD run. It is very useful to recognize the stability region when calculating thermodynamic parameters such as CTE and TEA as done in **Chapter 7 and 8**.

```

#!/usr/bin/perl

#PROGRAM: AIMD-data.pl

#      for NVT, NPT

#CREATED: 07/10/2013 by Chamila C. Dharmawardhana

#PURPOSE: AIMD data processing

#

```

#INPUTS: OSZICAR, OUTCAR

#OUTPUTS: aimd.dat

#LAST MODIFIED: 10/10/2013 by Shanaka Dharmawardhana

\$OUTCAR = "OUTCAR";

\$OSZICAR = "OSZICAR";

\$preasure = 0.0;

\$xx = 0.0;

\$yy = 0.0;

\$zz = 0.0;

\$ke = 0.0;

\$cellvolume = 0.0;

\$aaxis = 0.0;

\$baxis = 0.0;

\$caxis = 0.0;

\$state = 0;

@Table = ();

process OUTCAR

open(my \$fh, '<', \$OUTCAR) or die "Could not open file '\$OUTCAR' \$!";


```

while (my $row = <$fh>) {

    if ( $row =~ /\s*in kB\s+([-]?[0-9\\.]+)\s+([-]?[0-9\\.]+)\s+([-]?[0-9\\.]+).*$ / ) {

        $xx = $1;

        $yy = $2;

        $zz = $3;

    }

    elsif ( $row =~ /\s*external pressure\s*=\s*([-]?[0-9\\.]+)\s*kB.*$ / ) {

        $preasure = $1;

    }

    elsif ( $row =~ /\s*kinetic energy \s(ideal gas correction)\s*=\s*([-]?[0-9\\.]+)\s*kB.*$ / ) {

        $ke = $1;

    }

    elsif ( $row =~ /\s*volume of cell\s*:\s*([-]?[0-9\\.]+).*$ / ) {

        $cellvolume = $1;

    }

    elsif ( $row =~ /\s*VOLUME and BASIS-vectors are now\s*:.*$ / ) {

        $state = $state | 1;

    }

    elsif ( (($state & 1) != 0) && ( $row =~ /\s*length of vectors\s*$ / ) ) {

        $state = $state & ( 1 ^ 255 ); # unset state bit

        $row = <$fh>;      # read next line
    }
}

```

```

if ( $row =~ /^s*([-]?[0-9\\.]+)\s+([-]?[0-9\\.]+)\s+([-]?[0-9\\.]+)\s*.*$/ ) {

    $aaxis = $1;

    $baxis = $2;

    $caxis = $3;

}

$xx = $xx + $ke;

$yy = $yy + $ke;

$zz = $zz + $ke;

my $corrected = $preasure + $ke;

push @Table, [ $preasure, $xx, $yy, $zz, $corrected, 0.0, $cellvolume,
$aaxis, $baxis, $caxis ];

$preasure = 0.0;

$xx = 0.0;

$yy = 0.0;

$zz = 0.0;

$ke = 0.0;

$cellvolume = 0.0;

$aaxis = 0.0;

$baxis = 0.0;

$caxis = 0.0;

}

```

```
}
```

```
#process OSZICAR
```

```
open(my $fh, '<', $OSZICAR) or die "Could not open file '$OSZICAR' $!";
```

```
while (my $row = <$fh>) {
```

```
    if ( $row =~ /\s*([0-9]+\s+T\s*=\s*([-]?[0-9]\.?[0-9]+\s+E\s*=\s*([-]?[0-9]\.?[0-9]+\s+E)\s+F\s*=\s*([-]?[0-9]\.?[0-9]+\s+E)\s+E0\s*.*$/ ) {
```

```
        my $record = $1 - 1;
```

```
        my $T = $2;
```

```
        my $E = $3;
```

```
        my $F = $4;
```

```
        $Table[$record][5] = $T;
```

```
    }
```

```
}
```

```
# print table
```

```
printf "count      P      Pxx      Pyy      Pzz      P-corrected  T(K)      V(A^3)
```

```
a-axis(A)      b-axis(A)      c-axis(A)\n";
```

```
printf "-----  -----  -----  -----  -----  -----  -----  -----
```

```
-----\n";
```

```

$count = 1;

foreach my $record (@Table) {

    printf "%5d    %.2f    %.5f    %.5f    %.5f    %.2f    %.2f    %.2f    %.9f
%.9f    %.9f\n"

        , $count++, @$record[0], @$record[1], @$record[2], @$record[3], @$record[4]
        , @$record[5], @$record[6], @$record[7], @$record[8], @$record[9];

}

```

Following GnuPlot script (AIMD-plot.plt) will plot the thermodynamic parameters generated from the data filtering perl script (AIMD-data.pl) shown above.

```

#!/bin/gnuplot -persist

#PROGRAM: aimd-plot.plt

#    for NVT, NPT

#CREATED: 07/10/2013 by Chamila C. Dharmawardhana

#PURPOSE: AIMD data processing

#

#INPUTS: OSZICAR, OUTCAR

#OUTPUTS: Plots on std out. Can be saved as .png by

#           uncommenting proper output streams

#USAGE: gnuplot aimd-plots.plt

#LAST MODIFIED: 01/30/2015 by Chamila

#set terminal png medium size 600, 400

```

```

#set xtics 500

set grid xtics ytics

#####Plot of Corrected P tensor #####

set term X11 1

#set output 'P-tensor.png'

set ylabel "Pressure (kB)"

set xlabel "time (*2 fs)"

plot "aimd.dat" u 1:5 w l t "P",\
"" u 1:2 w l t "Pxx",\
"" u 1:3 w l t "Pyx",\
"" u 1:4 w l t "Pzz"

unset key

#####Plot of Temperature#####

set term X11 2

#set output 'T.png'

set ylabel "T (K)"

set xlabel "time (2*fs)"

plot "aimd.dat" u 1:6 w l

#####Plot of Cell Volume#####

set term X11 3

#set output 'V.png'

set ylabel "V (A^3)"

set xlabel "time (2*fs)"

```

```

plot "aimd.dat" u 1:7 w l

#####Plot of 'a-axis' fluctions#####

set term X11 4

#set output 'a.png'

set ylabel "a-axis(A)"

set xlabel "time (2*fs)"

plot "aimd.dat" u 1:8 w l

#####Plot of 'b-axis' fluctions#####

set term X11 5

#set output 'b.png'

set ylabel "b-axis(A)"

set xlabel "time (2*fs)"

#set yrange[19:19.6]

plot "aimd.dat" u 1:9 w l

#####Plot of 'c-axis' fluctions#####

set term X11 6

#set output 'c.png'

set ylabel "c-axis(A)"

set xlabel "time (2*fs)"

plot "aimd.dat" u 1:10 w l

pause -1

```

BIBLIOGRAPHY

1. Young, D., *Computational Chemistry: A Practical Guide for Applying Techniques to Real World Problems*. Wiley: 2004.
2. Kohn, W., Nobel Lecture: Electronic structure of matter-wave functions and density functionals. *Reviews of Modern Physics* **1999**, 71 (5), 1253-1266.
3. Parr, R. G., Density functional theory. *Annual Review of Physical Chemistry* **1983**, 34 (1), 631-656.
4. Richardson, I. G., The calcium silicate hydrates. *Cement and Concrete Research* **2008**, 38, 137-158.
5. (a) Parr, R. G.; Yang, W., *Density-functional theory of atoms and molecules*. Oxford university press: 1989; Vol. 16; (b) Capelle, K., A bird's-eye view of density-functional theory. *Brazilian Journal of Physics* **2006**, 36 (4A), 1318-1343; (c) Perdew, J. P.; Kurth, S., Density functionals for non-relativistic coulomb systems in the new century. In *A primer in density functional theory*, Springer: 2003; pp 1-55; (d) Koch, W.; Holthausen, M. C., *A chemist's guide to density functional theory*. Wiley-Vch Weinheim: 2001; Vol. 2.
6. Manzano, H. Atomistic Simulation Studies of the Cement Paste Components. Thesis, University of the Basque Country UPV/EHU, 2009.
7. Papatzani, S.; Paine, K.; Calabria-Holley, J., A comprehensive review of the models on the nanostructure of calcium silicate hydrates. *Construction and Building Materials* **2015**, 74, 219-234.

8. (a) Taylor, H. F. W., Proposed Structure for Calcium Silicate Hydrate Gel. *Journal of the American Ceramic Society* **1986**, 69 (6), 464-467; (b) Taylor, H. F. W., Tobermorite, jennite, and cement gel. *Zeitschrift für Kristallographie* **1992**, 202 (1-2), 41.
9. Ye, G.; Van Breugel, K.; Fraaij, A., Three-dimensional microstructure analysis of numerically simulated cementitious materials. *Cement and Concrete Research* **2003**, 33 (2), 215-222.
10. Bentz, D. P., Three-Dimensional Computer Simulation of Portland Cement Hydration and Microstructure Development. *Journal of the American Ceramic Society* **1997**, 80 (1), 3-21.
11. Maekawa, K.; Chaube, R.; Kishi, T., Modeling of concrete performance: hydration, microstructure formation and mass transport. *E and FN SPON, London* **1999**.
12. Bullard, J. W., A determination of hydration mechanisms for tricalcium silicate using a kinetic cellular automaton model. *Journal of the American Ceramic Society* **2008**, 91 (7), 2088-2097.
13. Pellenq, R.-M.; Caillol, J.; Delville, A., Electrostatic attraction between two charged surfaces: a (N, V, T) Monte Carlo simulation. *The Journal of Physical Chemistry B* **1997**, 101 (42), 8584-8594.
14. Shahsavari, R. Hierarchical modeling of structure and mechanics of cement hydrate. Massachusetts Institute of Technology, 2011.
15. Dolado, J. S.; Griebel, M.; Hamaekers, J., A Molecular Dynamic Study of Cementitious Calcium Silicate Hydrate (C–S–H) Gels. *Journal of the American Ceramic Society* **2007**, 90 (12), 3938-3942.

16. Richardson, I., Model structures for C-(A)-S-H(I). *Acta Crystallographica Section B* **2014**, 70 (6).
17. Soboyejo, W. O.; Srivatsan, T. S., *Advanced Structural Materials: Properties, Design Optimization, and Applications*. Taylor & Francis: 2006; p 504.
18. Rawn, C. J.; Schneibel, J. H.; Fu, C. L., Thermal expansion anisotropy and site occupation of the pseudo-binary molybdenum vanadium silicide Mo₅Si₃–V₅Si₃. *Acta Materialia* **2005**, 53 (8), 2431-2437.
19. Born, M.; Oppenheimer, R., Zur quantentheorie der molekeln. *Annalen der Physik* **1927**, 389 (20), 457-484.
20. Hohenberg, P.; Kohn, W., Inhomogeneous electron gas. *Physical review* **1964**, 136 (3B), B864.
21. Dreizler, R. M.; Gross, E. K., *Density Functional Theory: An Approach to the Quantum Many-Body Problem* Springer. Berlin: 1990.
22. Perdew, J. P.; Yue, W., Accurate and simple density functional for the electronic exchange energy: Generalized gradient approximation. *Physical review B* **1986**, 33 (12), 8800.
23. Perdew, J. P.; Burke, K.; Ernzerhof, M., Generalized gradient approximation made simple. *Physical review letters* **1996**, 77 (18), 3865.
24. Becke, A. D., Density-functional exchange-energy approximation with correct asymptotic behavior. *Physical review A* **1988**, 38 (6), 3098.
25. (a) Ching, W. Y.; Rulis, P., *Electronic Structure Methods for Complex Materials: The orthogonalized linear combination of atomic orbitals* Oxford University Press, USA: 2012; p 360; (b) Aryal, S.; Rulis, P.; Ching, W. Y., Mechanism for

- amorphization of boron carbide B₄C under uniaxial compression. *Physical Review B* **2011**, 84 (18), 184112; (c) Dharmawardhana, C. C.; Sakidja, R.; Aryal, S.; Ching, W. Y., Temperature dependent mechanical properties of Mo--Si--B compounds via ab initio molecular dynamics. *APL Materials* **2013**, 1 (1), 012106; (d) Dharmawardhana, C.; Sakidja, R.; Aryal, S.; Ching, W. Y., In search of zero thermal expansion anisotropy in Mo₅Si₃ by strategic alloying. *Journal of Alloys and Compounds* **2015**; (e) Dharmawardhana, C. C.; Misra, A.; Ching, W. Y., Quantum Mechanical Metric for Internal Cohesion in Cement Crystals. *Scientific reports* **2014**, 4, 7332.
26. Mulliken, R. S., Electronic Population Analysis on LCAO[Single Bond]MO Molecular Wave Functions. I. *The Journal of Chemical Physics* **1955**, 23 (10), 1833-1840.
 27. Ching, W. Y., Theoretical Studies of the Electronic Properties of Ceramic Materials. *Journal of the American Ceramic Society* **1990**, 73 (11), 3135-3160.
 28. Kresse, G.; Hafner, J., Ab initio molecular dynamics for liquid metals. *Physical Review B* **1993**, 47 (1), 558-561.
 29. Kresse, G.; Furthmüller, J., Efficiency of ab-initio total energy calculations for metals and semiconductors using a plane-wave basis set. *Computational Materials Science* **1996**, 6 (1), 15-50.
 30. Blöchl, P. E., Projector augmented-wave method. *Physical Review B* **1994**, 50 (24), 17953-17979.
 31. Kresse, G.; Joubert, D., From ultrasoft pseudopotentials to the projector augmented-wave method. *Physical review B* **1999**, 59 (3), 1758.

32. Vanderbilt, D., Soft self-consistent pseudopotentials in a generalized eigenvalue formalism. *Physical review B* **1990**, 41 (11), 7892.
33. Kresse, G.; Hafner, J., Norm-conserving and ultrasoft pseudopotentials for first-row and transition elements. *Journal of Physics: Condensed Matter* **1994**, 6 (40), 8245.
34. Yao, H.; Ouyang, L.; Ching, W.-Y., Ab Initio Calculation of Elastic Constants of Ceramic Crystals. *Journal of the American Ceramic Society* **2007**, 90 (10), 3194-3204.
35. Voigt, W., *Lehrbuch Der Kristallphysik (mit Ausschluss Der Kristalloptik)*. B.G. Teubner: 1928.
36. Reuss, A., Berechnung der Fließgrenze von Mischkristallen auf Grund der Plastizitätsbedingung für Einkristalle. *ZAMM - Journal of Applied Mathematics and Mechanics / Zeitschrift für Angewandte Mathematik und Mechanik* **1929**, 9 (1), 49-58.
37. Hill, R., The Elastic Behaviour of a Crystalline Aggregate. *Proc. Phys. Soc. A* **1952**, 65.
38. Allen, A. J.; Thomas, J. J.; Jennings, H. M., Composition and density of nanoscale calcium-silicate-hydrate in cement. *Nature materials* **2007**, 6 (4), 311-316.
39. Skinner, L. B.; Chae, S. R.; Benmore, C. J.; Wenk, H. R.; Monteiro, P. J. M., Nanostructure of Calcium Silicate Hydrates in Cements. *Physical Review Letters* **2010**, 104 (19), 195502.
40. Manzano, H.; Ayuela, A.; Dolado, J., On the formation of cementitious C–S–H nanoparticles. *Journal of Computer-Aided Materials Design* **2007**, 14 (1), 45-51.

41. Pellenq, R. J.-M.; Kushima, A.; Shahsavari, R.; Van Vliet, K. J.; Buehler, M. J.; Yip, S.; Ulm, F.-J., A realistic molecular model of cement hydrates. *Proceedings of the National Academy of Sciences* **2009**, *106* (38), 16102–16107.
42. Taylor, H. F. W., Nanostructure of C-S-H: Current status. *Advanced Cement Based Materials* **1993**, *1* (1), 38-46.
43. Zhang, X., Chang, W., Zhang, T., Ong, C. K. , Nanostructure of Calcium Silicate Hydrate Gels in Cement Paste. *Journal of the American Ceramic Society* **2000**, *83* (10), 2600-2604.
44. Dolado, J. S.; Griebel, M.; Hamaekers, J.; Heber, F., The nano-branched structure of cementitious calcium-silicate-hydrate gel. *Journal of Materials Chemistry* **2011**, *21* (12), 4445-4449.
45. Dolado, J. S.; Van Breugel, K., Recent advances in modeling for cementitious materials. *Cement and Concrete Research* **2011**, *41* (7), 711-726.
46. French, R. H.; Parsegian, V. A.; Podgornik, R.; Rajter, R. F.; Jagota, A.; Luo, J.; Asthagiri, D.; Chaudhury, M. K.; Chiang, Y.-m.; Granick, S.; Kalinin, S.; Kardar, M.; Kjellander, R.; Langreth, D. C.; Lewis, J.; Lustig, S.; Wesolowski, D.; Wettlaufer, J. S.; Ching, W. Y.; Finnis, M.; Houlihan, F.; von Lilienfeld, O. A.; van Oss, C. J.; Zemb, T., Long range interactions in nanoscale science. *Reviews of Modern Physics* **2010**, *82* (2), 1887-1944.
47. (a) Merlino, S.; Bonaccorsi, E.; Armbruster, T., Tobermorites; their real structure and order-disorder (OD) character. *American Mineralogist* **1999**, *84* (10), 1613-1621; (b) Bonaccorsi, E.; Merlino, S.; Kampf, A. R., The Crystal Structure of

- Tobermorite 14 Å (Plombierite), a C–S–H Phase. *Journal of the American Ceramic Society* **2005**, 88 (3), 505-512.
48. Bonaccorsi, E.; Merlino, S.; Taylor, H. F. W., The crystal structure of jennite, $\text{Ca}_9\text{Si}_6\text{O}_{18}(\text{OH})_6 \cdot 8\text{H}_2\text{O}$. *Cement and Concrete Research* **2004**, 34 (9), 1481-1488.
 49. (a) Pellenq, R. J.-M.; Lequeux, N.; van Damme, H., Engineering the bonding scheme in C-S-H: The iono-covalent framework. *Cement and Concrete Research* **2008**, 38 (2), 159-174; (b) Sanchez, F., Atomic-scale computational modeling of cement and concrete. *American Ceramic Society bulletin* **2010**, 89 (4), 28.
 50. Perdew, J. P., Accurate Density Functional for the Energy: Real-Space Cutoff of the Gradient Expansion for the Exchange Hole. *Physical Review Letters* **1985**, 55 (16), 1665-1668.
 51. (a) Merlino, S.; Bonaccorsi, E.; Armbruster, T., The real structures of clinotobermorite and tobermorite 9 Å: OD character, polytypes, and structural relationships. *Eur J Mineral* **2000**, 12 (2), 411-429; (b) Hamid, S. A., The crystal structure of the 11Å natural tobermorite $\text{Ca}_{2.25}[\text{Si}_3\text{O}_{7.5}(\text{OH})_{1.5}] \cdot 1\text{H}_2\text{O}$. *Zeitschrift für Kristallographie* **1981**, 154 (3-4), 189-198.
 52. Brese, N. E.; O'Keeffe, M., Bond-valence parameters for solids. *Acta Crystallographica Section B* **1991**, 47 (2), 192-197.
 53. Liang, L.; Rulis, P.; Ouyang, L.; Ching, W. Y., Ab initio investigation of hydrogen bonding and network structure in a supercooled model of water. *Physical Review B* **2011**, 83 (2), 024201.

54. Shahsavari, R.; Buehler, M. J.; Pellenq, R. J. M.; Ulm, F.-J., First-Principles Study of Elastic Constants and Interlayer Interactions of Complex Hydrated Oxides: Case Study of Tobermorite and Jennite. *Journal of the American Ceramic Society* **2009**, 92 (10), 2323-2330.
55. Manzano, H.; Dolado, J. S.; Ayuela, A., Elastic properties of the main species present in Portland cement pastes. *Acta Materialia* **2009**, 57 (5), 1666-1674.
56. Gmira, A.; Zabat, M.; Pellenq, R.; Van Damme, H., Microscopic physical basis of the poromechanical behavior of cement-based materials. *Materials and Structures* **2004**, 37 (1), 3-14.
57. Richardson, I. G.; Groves, G. W., Models for the composition and structure of calcium silicate hydrate (C-S-H) gel in hardened tricalcium silicate pastes. *Cement and Concrete Research* **1992**, 22 (6), 1001-1010.
58. Aryal, S.; Rulis, P.; Ching, W. Y., Mechanical Properties and Electronic Structure of Mullite Phases Using First-Principles Modeling. *Journal of the American Ceramic Society* **2012**, 95 (7), 2075-2088.
59. Oh, J. E.; Clark, S. M.; Wenk, H.-R.; Monteiro, P. J. M., Experimental determination of bulk modulus of 14Å tobermorite using high pressure synchrotron X-ray diffraction. *Cement and Concrete Research* **2012**, 42 (2), 397-403.
60. Constantinides, G.; Ulm, F.-J., The nanogranular nature of C–S–H. *Journal of the Mechanics and Physics of Solids* **2007**, 55 (1), 64-90.
61. Monteiro, P. J. M.; Chang, C. T., The elastic moduli of calcium hydroxide. *Cement and Concrete Research* **1995**, 25 (8), 1605-1995.

62. (a) Bernal, J. D. In *The structure of cement hydration compounds*, Proceedings of the third International Symposium on the Chemistry of Cement, London, Cement and Concrete Association: London, 1952; pp 216–236; (b) Taylor, H.; Howison, J., Relationships between calcium silicates and clay minerals. *Clay Minerals Bull* **1956**, 3, 98-111; (c) Glasser, F. P.; Lachowski, E. E.; Macphee, D. E., Compositional Model for Calcium Silicate Hydrate (C-S-H) Gels, Their Solubilities, and Free Energies of Formation. *Journal of the American Ceramic Society* **1987**, 70 (7), 481-485.
63. (a) Taylor, H. F. W.; Roy, D. M. In *Structure and Composition of Hydrates*, 7th International Congress on the Chemistry of Cement: Principal Reports, Paris, Editions Septima: Paris, 1980; pp PII 2/1–13; (b) Cong, X.; Kirkpatrick, R. J., ²⁹Si MAS NMR study of the structure of calcium silicate hydrate. *Advanced Cement Based Materials* **1996**, 3 (3-4), 144-156.
64. Richardson, I. G., The nature of C-S-H in hardened cements. *Cement and Concrete Research* **1999**, 29 (8), 1131-1147.
65. Strunz, H., *Mineralogische Tabellen*. Akad. Verl.-Ges. Geest u. Portig: Leipzig, 1982.
66. Jennings, H. M., A model for the microstructure of calcium silicate hydrate in cement paste. *Cement and Concrete Research* **2000**, 30 (1), 101-116.
67. Tennis, P. D.; Jennings, H. M., A model for two types of calcium silicate hydrate in the microstructure of Portland cement pastes. *Cement and Concrete Research* **2000**, 30 (6), 855-863.

68. Cong, X.; James Kirkpatrick, R., ^{17}O and ^{29}Si MAS NMR study of β -C2S hydration and the structure of calcium-silicate hydrates. *Cement and Concrete Research* **1993**, 23 (5), 1065-1077.
69. Thomas, S.; Meise-Gresch, K.; Müller-Warmuth, W.; Odler, I., MAS NMR Studies of Partially Carbonated Portland Cement and Tricalcium Silicate Pastes. *Journal of the American Ceramic Society* **1993**, 76 (8), 1998-2004.
70. Garbev, K.; Black, L.; Beuchle, G.; Stemmermann, P., Inorganic polymers in cement based materials. *Wasser-und Geotechnologie* **2002**, 1, 19-31.
71. De la Torre, Á. G.; De Vera, R. N.; Cuberos, A. J. M.; Aranda, M. A. G., Crystal structure of low magnesium-content alite: Application to Rietveld quantitative phase analysis. *Cement and Concrete Research* **2008**, 38 (11), 1261-1269.
72. Armbruster, T.; Lazic, B.; Galuskina, I.; Galuskin, E.; Gnos, E.; Marzec, K.; Gazeev, V., Trabzonite, $\text{Ca}_4 [\text{Si}_3\text{O}_9 (\text{OH})] \text{OH}$: crystal structure, revised formula, new occurrence and relation to killalaite. *Mineralogical Magazine* **2012**, 76 (3), 455-472.
73. Dharmawardhana, C. C.; Misra, A.; Aryal, S.; Rulis, P.; Ching, W. Y., Role of interatomic bonding in the mechanical anisotropy and interlayer cohesion of CSH crystals. *Cement and Concrete Research* **2013**, 52 (0), 123-130.
74. Haslingerová, I., Estimation of bond energies from mulliken overlap populations. *Czech J Phys* **1977**, 27 (12), 1389-1393.
75. (a) Richardson, I.; Skibsted, J.; Black, L.; Kirkpatrick, R. J., Characterisation of cement hydrate phases by TEM, NMR and Raman spectroscopy. *Advances in Cement Research* **2010**, 22 (4), 233-248; (b) Doyle, S. G., *Construction and*

Building: Design, Materials, and Techniques. Nova Science Publishers, Incorporated: 2010.

76. Rastsvetaeva, R. K.; Chukanov, N. V.; Zadov, A. E., Refined structure of afwillite from the northern Baikal region. *Crystallogr. Rep.* **2009**, *54* (3), 418-422.
77. Malik, K. M. A.; Jeffery, J. W., A re-investigation of the structure of afwillite. *Acta Crystallographica Section B* **1976**, *32* (2), 475-480.
78. Kim, J.; Schmitt, U. W.; Gruetzmacher, J. A.; Voth, G. A.; Scherer, N. E., The vibrational spectrum of the hydrated proton: Comparison of experiment, simulation, and normal mode analysis. *The Journal of Chemical Physics* **2002**, *116* (2), 737-746.
79. Agrell, S. O.; Gay, P., Kilchoanite, a polymorph of rankinite. *Nature* **1961**, *189*, 743-743.
80. Roy, D. M.; Gard, J. A.; Nicol, A. W.; Taylor, H. F. W., New Data for the Calcium Silicate, 'Phase Z'. *Nature* **1960**, *188*, 1187-1188.
81. Zhesheng, M.; Nicheng, S.; Guodong, M.; Libing, L., Crystal structure refinement of suolunite and its significance to the cement techniques. *Chin. Sci. Bull.* **1999**, *44* (23), 2125-2130.
82. Ito, T.-i.; Sadanaga, R.; Takéuchi, Y.; Tokonami, M., The existence of partial mirrors in wollastonite. *Proceedings of the Japan Academy* **1969**, *45* (10), 913-918.
83. (a) Velez, K.; Maximilien, S.; Damidot, D.; Fantozzi, G.; Sorrentino, F., Determination by nanoindentation of elastic modulus and hardness of pure constituents of Portland cement clinker. *Cement and Concrete Research* **2001**, *31*

- (4), 555-561; (b) Ulm, F.; Bazant, Z.; Wittman, F., *Creep, Shrinkage, and Durability Mechanics of Concrete and Other Quasi-Brittle Materials*. Elsevier: 2001.
84. (a) Beaudoin, J. J., Comparison of mechanical properties of compacted calcium hydroxide and portland cement paste systems. *Cement and Concrete Research* **1983**, 13 (3), 319-324; (b) Wittmann, F. H., Estimation of the modulus of elasticity of calcium hydroxide. *Cement and Concrete Research* **1986**, 16 (6), 971-972.
 85. Cong, X.; Kirkpatrick, R. J., ^{29}Si and ^{17}O NMR investigation of the structure of some crystalline calcium silicate hydrates. *Advanced Cement Based Materials* **1996**, 3 (3), 133-143.
 86. Misra, A.; Ching, W. Y., Theoretical nonlinear response of complex single crystal under multi-axial tensile loading. *Scientific reports* **2013**, 3.
 87. Allen, A. J.; Thomas, J. J., Analysis of C–S–H gel and cement paste by small-angle neutron scattering. *Cement and Concrete Research* **2007**, 37 (3), 319-324.
 88. Constantinides, G.; Ulm, F.-J., The effect of two types of C-S-H on the elasticity of cement-based materials: Results from nanoindentation and micromechanical modeling. *Cement and Concrete Research* **2004**, 34 (1), 67-80.
 89. Purnell, D. P. Novel uses for cement 2009.
<http://www.engineering.leeds.ac.uk/resilience/partners/documents/sota1-outline-webdraft1.pdf>.
 90. Qomi, M. A.; Krakowiak, K.; Bauchy, M.; Stewart, K.; Shahsavari, R.; Jagannathan, D.; Brommer, D.; Baronnet, A.; Buehler, M.; Yip, S., Combinatorial molecular optimization of cement hydrates. *Nature communications* **2014**, 5, 1-10.

91. Yamnova, N.; Sarp, K.; Egorov-Tismenko, Y. K.; Pushcharovski, D.; Dasgupta, G., Crystal structure of jaffeite. *Crystallogr. Rep.* **1993**, 38 (4), 464-467.
92. Pharr, G. M.; Oliver, W. C.; Brotzen, F. R., On the generality of the relationship among contact stiffness, contact area, and elastic modulus during indentation. *Journal of Materials Research* **1992**, 7 (03), 613-617.
93. Hertz, H., Über die Berührung fester elastischer Körper. **1882**.
94. Johnson, K.; Kendall, K.; Roberts, A., Surface energy and the contact of elastic solids. *Proceedings of the royal society of London. A. mathematical and physical sciences* **1971**, 324 (1558), 301-313.
95. Plassard, C.; Lesniewska, E.; Pochard, I.; Nonat, A. In *Intrinsic elastic properties of Calcium Silicate Hydrates by nanoindentation*, Proceedings of the 12th International Congress on the Chemistry of Cement, 2007.
96. Pelisser, F.; Gleize, P. J. P.; Mikowski, A., Effect of the Ca/Si Molar Ratio on the Micro/nanomechanical Properties of Synthetic C-S-H Measured by Nanoindentation. *The Journal of Physical Chemistry C* **2012**, 116 (32), 17219-17227.
97. Alizadeh, R.; Beaudoin, J. J.; Raki, L., Viscoelastic nature of calcium silicate hydrate. *Cement and Concrete Composites* **2010**, 32 (5), 369-376.
98. Matsuyama, H.; Young, J., Effects of pH on precipitation of quasi-crystalline calcium silicate hydrate in aqueous solution. *Advances in cement research* **2000**, 12 (1), 29-33.
99. Gard, J.; Taylor, H., Calcium silicate hydrate (II) ("CSH (II)"). *Cement and Concrete Research* **1976**, 6 (5), 667-677.

100. (a) Taylor, H. F. W., *The chemistry of cements*. Academic Press: 1964; p 168-232;
(b) Taylor, H. F., *Cement chemistry*. Thomas Telford: 1997.
101. Taylor, R.; Richardson, I.; Brydson, R., Composition and microstructure of 20-year-old ordinary Portland cement–ground granulated blast-furnace slag blends containing 0 to 100% slag. *Cement and Concrete Research* **2010**, 40 (7), 971-983.
102. Heller, L.; Taylor, H. F., *Crystallographic data for the calcium silicates*. HM Stationery Office: 1956; Vol. 49.
103. (a) Taylor, H. W., 726. Hydrated calcium silicates. Part I. Compound formation at ordinary temperatures. *Journal of the Chemical Society (Resumed)* **1950**, 3682-3690; (b) Bernal, J.; Jeffery, J.; Taylor, H., Crystallographic research on the hydration of Portland cement. A first report on investigations in progress. *Magazine of Concrete research* **1952**, 4 (11), 49-54.
104. Kalousek, G.; PREBUS, A. F., Crystal chemistry of hydrous calcium silicates: III, Morphology and other properties of tobermorite and related phases. *Journal of the American Ceramic Society* **1958**, 41 (4), 124-132.
105. McConnell, J., The hydrated calcium silicates riversideite, tobermorite, and plombierite. *Mineral. Mag* **1954**, 30, 293-305.
106. Hoffmann, C.; Armbruster, T., Clinotobermorite, $\text{Ca}_5 [\text{Si}_3\text{O}_8 (\text{OH})]_2 \cdot 4 \text{H}_2\text{O} - \text{Ca}_5 [\text{Si}_6\text{O}_7]_5 \text{H}_2\text{O}$, CSH (I) type cement mineral: determination of the substructure. *Zeitschrift für Kristallographie* **1997**, 212, 864-873.
107. Bonaccorsi, E.; Merlino, S., Modular Microporous Minerals: Cancrinite-Davyne Group and C-S-H Phases. *Reviews in Mineralogy and Geochemistry* **2005**, 57 (1), 241-290.

108. Garbev, K.; Beuchle, G.; Bornefeld, M.; Black, L.; Stemmermann, P., Cell Dimensions and Composition of Nanocrystalline Calcium Silicate Hydrate Solid Solutions. Part 1: Synchrotron-Based X-Ray Diffraction. *Journal of the American Ceramic Society* **2008**, *91* (9), 3005-3014.
109. Garbev, K.; Bornefeld, M.; Beuchle, G.; Stemmermann, P., Cell Dimensions and Composition of Nanocrystalline Calcium Silicate Hydrate Solid Solutions. Part 2: X-Ray and Thermogravimetry Study. *Journal of the American Ceramic Society* **2008**, *91* (9), 3015-3023.
110. Renaudin, G.; Russias, J.; Leroux, F.; Frizon, F.; Cau-dit-Coumes, C., Structural characterization of C–S–H and C–A–S–H samples—part I: long-range order investigated by Rietveld analyses. *Journal of Solid State Chemistry* **2009**, *182* (12), 3312-3319.
111. Faucon, P.; Petit, J. C.; Charpentier, T.; Jacquinet, J. F.; Adenot, F., Silicon substitution for aluminum in calcium silicate hydrates. *Journal of the American Ceramic Society* **1999**, *82* (5), 1307-1312.
112. (a) Lemberg, J. A.; Ritchie, R. O., Mo-Si-B Alloys for Ultrahigh-Temperature Structural Applications. *Advanced Materials* **2012**, *24* (26), 3445-3480; (b) Perepezko, J. H., The Hotter the Engine, the Better. *Science* **2009**, *326* (5956), 1068-1069.
113. Nunes, C.; Coelho, G.; Ramos, A., On the invariant reactions in the Mo-rich portion of the Mo-Si system. *JPE* **2001**, *22* (5), 556-559.
114. (a) Ito, K.; Ihara, K.; Tanaka, K.; Fujikura, M.; Yamaguchi, M., Physical and mechanical properties of single crystals of the T2 phase in the Mo–Si–B system.

- Intermetallics* **2001**, 9 (7), 591-602; (b) Chu, F.; Thoma, D. J.; McClellan, K.; Peralta, P.; He, Y., Synthesis and properties of Mo_5Si_3 single crystals. *Intermetallics* **1999**, 7 (5), 611-620.
115. (a) Meyer, M.; Kramer, M.; Akinc, M., Boron-doped molybdenum silicides. *Advanced Materials* **1996**, 8 (1), 85-88; (b) Meyer, M. K.; Akinc, M., Oxidation behavior of boron-modified Mo_5Si_3 at 800°C - 1300°C . *Journal of the American Ceramic Society* **1996**, 79 (4), 938-944.
116. Zhao, H. L.; Kramer, M. J.; Akinc, M., Thermal expansion behavior of intermetallic compounds in the Mo-Si-B system. *Intermetallics* **2004**, 12 (5), 493-498.
117. Huebsch, J. J.; Kramer, M. J.; Zhao, H. L.; Akinc, M., Solubility of boron in $\text{Mo}_{5+y}\text{Si}_{3-y}$. *Intermetallics* **2000**, 8 (2), 143-150.
118. (a) Bercegeay, C.; Bernard, S., First-principles equations of state and elastic properties of seven metals. *Physical Review B* **2005**, 72 (21), 214101; (b) Gressmann, T.; Wohlschlägel, M.; Shang, S.; Welzel, U.; Leineweber, A.; Mittemeijer, E. J.; Liu, Z. K., Elastic anisotropy of γ' - Fe_4N and elastic grain interaction in γ' - $\text{Fe}_4\text{N}_{1-y}$ layers on α -Fe: First-principles calculations and diffraction stress measurements. *Acta Materialia* **2007**, 55 (17), 5833-5843; (c) Le Page, Y.; Saxe, P., Symmetry-general least-squares extraction of elastic coefficients from ab initio total energy calculations. *Physical Review B* **2001**, 63 (17), 174103.
119. (a) Ganeshan, S.; Shang, S. L.; Wang, Y.; Liu, Z. K., Effect of alloying elements on the elastic properties of Mg from first-principles calculations. *Acta Materialia* **2009**, 57 (13), 3876-3884; (b) Ganeshan, S.; Shang, S. L.; Zhang, H.; Wang, Y.; Mantina, M.; Liu, Z. K., Elastic constants of binary Mg compounds from first-principles

- calculations. *Intermetallics* **2009**, 17 (5), 313-318; (c) Kim, D.; Shang, S.-L.; Liu, Z.-K., Effects of alloying elements on elastic properties of Ni by first-principles calculations. *Computational Materials Science* **2009**, 47 (1), 254-260; (d) Le Page, Y.; Saxe, P., Symmetry-general least-squares extraction of elastic data for strained materials from ab initio calculations of stress. *Physical Review B* **2002**, 65 (10), 104104; (e) Shang, S. L.; Sheng, G.; Wang, Y.; Chen, L. Q.; Liu, Z. K., Elastic properties of cubic and rhombohedral BiFeO₃ from first-principles calculations. *Physical Review B* **2009**, 80 (5), 052102; (f) Shang, S.; Wang, Y.; Liu, Z.-K., First-principles elastic constants of alpha- and theta-Al₂O₃. *Applied Physics Letters* **2007**, 90 (10), 101909; (g) Zhang, J. X.; Li, Y. L.; Wang, Y.; Liu, Z. K.; Chen, L. Q.; Chu, Y. H.; Zavaliche, F.; Ramesh, R., Effect of substrate-induced strains on the spontaneous polarization of epitaxial BiFeO₃ thin films. *Journal of Applied Physics* **2007**, 101 (11), 114105.
120. (a) Baroni, S.; Giannozzi, P.; Testa, A., Elastic Constants of Crystals from Linear-Response Theory. *Physical Review Letters* **1987**, 59 (23), 2662-2665; (b) Hamann, D. R.; Wu, X.; Rabe, K. M.; Vanderbilt, D., Metric tensor formulation of strain in density-functional perturbation theory. *Physical Review B* **2005**, 71 (3), 035117; (c) Wu, X.; Vanderbilt, D.; Hamann, D. R., Systematic treatment of displacements, strains, and electric fields in density-functional perturbation theory. *Physical Review B* **2005**, 72 (3), 035105.
121. Wang, Y.; Wang, J. J.; Zhang, H.; Manga, V. R.; Shang, S. L.; Chen, L.-Q.; Liu, Z.-K., A first-principles approach to finite temperature elastic constants. *Journal of Physics: Condensed Matter* **2010**, 22 (22), 225404.

122. (a) Woodward, C.; Asta, M.; Trinkle, D. R.; Lill, J.; Angioletti-Uberti, S., Ab initio simulations of molten Ni alloys. *Journal of Applied Physics* **2010**, *107* (11), 113522; (b) Kirchner, B.; Dio, P.; Hutter, J., Real-World Predictions from Ab Initio Molecular Dynamics Simulations. In *Multiscale Molecular Methods in Applied Chemistry*, Kirchner, B.; Vrabec, J., Eds. Springer Berlin Heidelberg: 2012; Vol. 307, pp 109-153; (c) Hafner, J., Ab-initio simulations of materials using VASP: Density-functional theory and beyond. *Journal of Computational Chemistry* **2008**, *29* (13), 2044-2078.
123. Oganov, A. R.; Brodholt, J. P.; Price, G. D., Ab initio elasticity and thermal equation of state of MgSiO_3 perovskite. *Earth and Planetary Science Letters* **2001**, *184* (3–4), 555-560.
124. Birch, F., Finite Elastic Strain of Cubic Crystals. *Physical Review* **1947**, *71* (11), 809-824.
125. Rawn, C. J.; Schneibel, J. H.; Hoffmann, C. M.; Hubbard, C. R., The crystal structure and thermal expansion of Mo_5SiB_2 . *Intermetallics* **2001**, *9* (3), 209-216.
126. Nielsen, O. H.; Martin, R. M., First-Principles Calculation of Stress. *Physical Review Letters* **1983**, *50* (9), 697-700.
127. Chu, F.; Thoma, D. J.; McClellan, K. J.; Peralta, P., Mo_5Si_3 single crystals: Physical properties and mechanical behavior. *Materials Science and Engineering A* **1999**, *261* (1-2), 44-52.
128. (a) Ono, S.; Brodholt, J. P.; Alfe, D.; Alfredsson, M.; Price, G. D., Ab initio molecular dynamics simulations for thermal equation of state of B2-type NaCl. *Journal of Applied Physics* **2008**, *103* (2), 023510; (b) Ono, S., First-Principles

Molecular Dynamics Calculations of the Equation of State for Tantalum.

International Journal of Molecular Sciences **2009**, *10* (10), 4342-4351.

129. Greaves, G. N.; Greer, A. L.; Lakes, R. S.; Rouxel, T., Poisson's ratio and modern materials. *Nat Mater* **2011**, *10* (11), 823-837.
130. Fu, C.; Wang, X.; Ye, Y.; Ho, K., Phase stability, bonding mechanism, and elastic constants of Mo_5Si_3 by first-principles calculation. *Intermetallics* **1999**, *7* (2), 179-184.
131. (a) Schneibel, J. H.; Rawn, C. J.; Payzant, E. A.; Fu, C. L., Controlling the thermal expansion anisotropy of Mo_5Si_3 and Ti_5Si_3 silicides. *Intermetallics* **2004**, *12* (7–9), 845-850; (b) Fu, C. L.; Schneibel, J. H., Reducing the thermal expansion anisotropy in Mo_5Si_3 by Nb and V additions: theory and experiment. *Acta Materialia* **2003**, *51* (17), 5083-5092.
132. (a) Williams, J.; Akinc, M., Oxidation behavior of V_5Si_3 based materials. *Intermetallics* **1998**, *6* (4), 269-275; (b) Behrani, V.; Thom, A. J.; Kramer, M. J.; Akinc, M., Microstructure and oxidation behavior of Nb–Mo–Si–B alloys. *Intermetallics* **2006**, *14* (1), 24-32.
133. (a) Yanagiharal, K.; Maruyama, T.; Nagata, K., Isothermal and Cyclic Oxidation of $\text{Mo}(\text{Si}_{1-x}\text{Al}_x)_2$ up to 2048 K. *Materials transactions-JIM* **1993**, *34* (12), 1200-1206; (b) Rosales, I.; Martinez, H.; Bahena, D.; Ruiz, J. A.; Guardian, R.; Colin, J., Oxidation performance of Mo_3Si with Al additions. *Corrosion Science* **2009**, *51* (3), 534-538.

134. Stergiou, A.; Tsakiroopoulos, P.; Brown, A., The intermediate and high-temperature oxidation behaviour of $\text{Mo}(\text{Si}_{1-x}\text{Al}_x)_2$ intermetallic alloys. *Intermetallics* **1997**, 5 (1), 69-81.
135. Sharif, A. A.; Misra, A.; Petrovic, J. J.; Mitchell, T. E., Alloying of MoSi_2 for improved mechanical properties. *Intermetallics* **2001**, 9 (10–11), 869-873.
136. Ponweiser, N.; Paschinger, W.; Ritscher, A.; Schuster, J. C.; Richter, K. W., Phase equilibria in the Al–Mo–Si system. *Intermetallics* **2011**, 19 (3), 409-418.
137. Nunes, C.; Sakidja, R.; Dong, Z.; Perepezko, J., Liquidus projection for the Mo-rich portion of the Mo–Si–B ternary system. *Intermetallics* **2000**, 8 (4), 327-337.
138. Waghmare, U. V.; Kaxiras, E.; Bulatov, V. V.; Duesbery, M. S., Effects of alloying on the ductility of MoSi_2 single crystals from first-principles calculations. *Modelling and Simulation in Materials Science and Engineering* **1998**, 6 (4), 493.
139. Guo, C.; Li, C.; Masset, P. J.; Du, Z., A thermodynamic description of the Al–Mo–Si system. *Calphad* **2012**, 36 (0), 100-109.
140. (a) Adams, D. J.; Oganov, A. R., Ab initio molecular dynamics study of CaSiO_3 perovskite at P-T conditions of Earth's lower mantle. *Physical Review B* **2006**, 73 (18), 184106; (b) Grabowski, B.; Ismer, L.; Hickel, T.; Neugebauer, J., Ab initio up to the melting point: Anharmonicity and vacancies in aluminum. *Physical Review B* **2009**, 79 (13), 134106.
141. Fu, C. L.; Wang, X., Thermal expansion coefficients of Mo-Si compounds by first-principles calculations. *Philosophical Magazine Letters* **2000**, 80 (10), 683-690.

142. Aryal, S.; Gao, M.; Ouyang, L.; Rulis, P.; Ching, W., Ab initio studies of Mo-based alloys: Mechanical, elastic, and vibrational properties. *Intermetallics* **2013**, 38, 116-125.
143. Róg, T.; Murzyn, K.; Hinsén, K.; Kneller, G. R., nMoldyn: A program package for a neutron scattering oriented analysis of molecular dynamics simulations. *Journal of Computational Chemistry* **2003**, 24 (5), 657-667.
144. Rodrigues, G.; Nunes, C. A.; Suzuki, P. A.; Coelho, G. C., Thermal expansion of the V_5Si_3 and T2 phases of the V–Si–B system investigated by high-temperature X-ray diffraction. *Intermetallics* **2009**, 17 (10), 792-795.
145. Wu, M.-M.; Jiang, Y.; Wang, J.-W.; Wu, J.; Tang, B.-Y.; Peng, L.-M.; Ding, W.-J., Structural, elastic and electronic properties of $Mg (Cu_{1-x}Zn_x)_2$ alloys calculated by first-principles. *Journal of Alloys and Compounds* **2011**, 509 (6), 2885-2890.

VITA

Chamila Chathuranga Dharmawardhana was born on October 03rd, 1980 in Colombo, Sri Lanka. He finished his schooling from local public school. Mr. Dharmawardhana studied at University of Colombo, bachelor's degree (B.Sc.) majoring in physics.

In August 2006, Mr. Dharmawardhana came to the United States as a graduate student in the Department of Physics at the Central Michigan University. He got his master's degree (MS) in 2008 from the Central Michigan University. While studying for master's degree, Mr. Dharmawardhana worked as a teaching assistant in department of physics. Mr. Dharmawardhana started in Science of Advanced Materials interdisciplinary PhD program at Central Michigan University in 2008.

Mr. Dharmawardhana transferred to the interdisciplinary PhD program with physics as coordinating discipline and geosciences as co-discipline in July 2011 at University of Missouri – Kansas City.

Mr. Dharmawardhana has authored and co-authored six scientific papers in peer reviewed journals. He has presented three posters and four talks in different conference.

Publications:

1. Dharmawardhana CC, Sakidja R, Aryal S, Ching WY (2013) "Temperature dependent mechanical properties of Mo-Si-B compounds via ab initio molecular dynamics" APL Materials 1(1):012106.
2. Dharmawardhana CC, Misra A, Aryal S, Rulis P, Ching WY (2013) "Role of interatomic bonding in the mechanical anisotropy and interlayer cohesion of CSH crystals" Cement and Concrete Research 52(0):123-130.
3. Li N, Dharmawardhana CC, Yao K, Ching WY (2013) "Theoretical characterization on intrinsic ferrimagnetic phase in nanoscale laminated Cr_2GeC " Solid State Communications 174:43-45 13.
4. Dharmawardhana CC, Misra A, Ching WY (2014) "Quantum Mechanical Metric for Internal Cohesion in Cement Crystals" Scientific reports 4:7332.
5. Dharmawardhana CC, Sakidja R, Aryal S, Ching WY (2015) "In search of zero thermal expansion anisotropy in Mo_5Si_3 by strategic alloying" Journal of Alloys and Compounds 620:427433.
6. Walker B, Dharmawardhana CC, Dari N, Rulis P, Ching WY (2015) "Electronic structure and optical properties of amorphous GeO_2 and in comparison to amorphous SiO_2 " Journal of Non-Crystalline Solids 428:176-183.
7. Dharmawardhana CC, Bakare M, Misra A, Ching WY (2015) "Nature of interatomic bonding in controlling the mechanical properties of Calcium Silicate Hydrates" Journal of the American Ceramic Society (in review).

8. Poudel L, Tamler C, Dharmawardhana CC, Anil M, Ching WY, “Interfacial cohesion of peptide/aragonite surface: the role played by hydrogen bonding and water” (in preparation).
9. Dharmawardhana CC, Dari N, Ching WY, “Elastic Anisotropy of all ternary MAX phases” (in preparation).
10. Hussain A, Dharmawardhana CC, Sakidja R, Ching WY, “ab initio Molecular Dynamics (AIMD) Study and Potential Development of Ti-Si-C Metallic System” (in preparation).
11. Hunca B, Dharmawardhana CC, Ching WY, “Electronic structure and bonding in vitreloy $Zr_{41.2}Ti_{13.8}Cu_{12.5}Ni_{10}Be_{22.5}$ ” (in preparation).
12. Dharmawardhana CC, Misra A, Ching WY, “Electronic structure and mechanical properties of C-S-H (I) AND C-A-S-H (I) phases” (in preparation).